Residual Stress and Distortion Measurements on Induction Hardened AISI 4340 Discs

Jie Yi

A Thesis
in
The Department
of
Mechanical and Industrial Engineering

Presented in Partial Fulfillment of the Requirements
for the Degree of Master of Applied Science (Mechanical Engineering) at
Concordia University
Montreal, Quebec, Canada

September 2011

CONCORDIA UNIVERSITY

SCHOOL OF GRADUATE STUDIES

This is to certify that the Thesis prepared,

By: **Jie Yi**

Entitled: **"Residual Stress and Distortion Measurements on Induction Hardened AISI 4340 Discs"**

and submitted in partial fulfillment of the requirements for the Degree of

Master of Applied Science (Mechanical Engineering)

complies with the regulations of the University and meets the accepted standards with respect to originality and quality.

Signed by the Final Examining Committee:

_____	Chair
Dr. Rama Bhat	
_____	Examiner
Dr. Ramin Sedaghati	
_____	Examiner
Dr. Mohammad Jahazi	External
_____	Co-Supervisor
Dr. Mamoun Medraj	
_____	Co-Supervisor
Dr. Philippe Bocher	

Approved by: _____

Dr. A.K.W. Ahmed, MASc Program Director
Department of Mechanical and Industrial Engineering

_____

Dean Robin Drew
Faculty of Engineering & Computer Science

Date: _____

ABSTRACT

Residual Stress and Distortion Measurements on Induction Hardened AISI 4340 Discs

Jie Yi

In this study, 15 induction hardened AISI 4340 discs in three initial hardness levels were used for distortion investigations, by virtue of CMM (coordinate measuring machine). Triaxial residual stress measurement was performed on a selected disc sample by means of neutron diffraction technique. A comb reference sample was prepared by WEDM (wire electrical discharge machining) for obtaining the stress-free lattice spacing (d_0) distribution. Vickers hardness test was finally applied on this selected disc after the stress measurement.

The distortion results show that the distortion profile depends on both initial hardness of the sample and the applied induction hardening recipe. For the same initial hardness, the larger the energy input, the larger the distortion size as well as the hardening depth. For a given induction hardening recipe, the increase in initial hardness leads to a deeper hardening depth but a smaller distortion size.

The residual stress results show that the variation of d_0 in the hardened layer can vary the stress value in the same region up to ~200MPa. The hoop and axial residual stresses demonstrate a similar stress profile in the hardened layer with maximum compressive value of -1120MPa, approximately. The radial residual stress displays a significant variation in the surface layer. This variation is attributed to the questionable d_0 profile and the uncertainty of neutron diffraction method itself. The over-tempered region is found in the hardness profile, suggesting that tempering effect occurs during the induction hardening treatment.

ACKNOWLEDGEMENTS

First and foremost I would like to owe my deepest gratitude to my supervisor, Professor Mamoun Medraj, for his first-rate guidance, insightful suggestions, persistent help, continuous financial support, as well as the great patience and caring during my 3-year master studies at Concordia University. It is really an honor for me to work for him. Without his encouragement and effort this thesis would not have been accomplished.

I would like to give my great gratitude to Professor Philippe Bocher, my co-supervisor from École de technologie superieure (ETS) du Québec, for his explicit guidance on my research works and constantly offering valuable helps during my master studies.

Additionally, a special and great appreciation goes to Dr. Michael Gharghouri from Chalk River NRC Laboratories of Canadian Neutron Beam Centre, for his priceless, enormous and extremely important support in my Neutron Diffraction (ND) experiment. His thorough knowledge and vivid explanations of ND technique gave me a very deep impression and, I will never forget his kindness to pick me up day after day during my stay at Chalk River.

I would like to thank Hugo Landry for his continuous helps in the CMM measurements at

ETS. I would like to thank Benjamin Larregain, Dr. Florent Bridier, Vincent Savaria and Mr. Antoine Faure from ETS, for their aids and nice cooperation in my works. I would also want to thank Dr. Hoseini Majid from McGill University for his best suggestions.

Moreover, I would like to thank Jean-Marie Aubry from D.P. Digital Precision, for his help in sample preparation for ND experiments.

The financial support from PWC (Pratt & Whitney Company) for the whole CRIAQ project I involved is gratefully acknowledged.

Further, I wish to share the credit of my work with all research members in Prof. Medraj's group for their help, suggestions, encouragements and especially their meticulous care. I feel so fortunate to befriend with them.

I thank the staff in the Mechanical & Industrial Engineering department for their various assistants in administrative matters. I also want to give my thanks to all my thesis committee members for the thorough reading of my thesis and for their valuable suggestions.

Finally, I am greatly indebted to my family, my parents and grand-parents, as well as my

boyfriend, Yi Li, for their indestructible and forever support, cheering me up and encouraging me to finish this work.

TABLE OF CONTENTS

LIST OF ABBREVIATIONS

IH	Induction Hardening
CMM	Coordinate Measuring Machine
EDM	Electrical Discharge Machining
WEDM	Wire Electrical Discharge Machining
ND	Neutron Diffraction
XRD	X-ray Diffraction
d	Atomic lattice spacing
d_0	Unstressed atomic lattice spacing (stress-free lattice spacing)
SGV	Sampling Gauge Volume
RS	Residual Stress

CHAPTER 1

Introduction

1.1 Background

Good performance mechanical components used for aerospace applications always require a combination of high strength, high hardness as well as satisfactory toughness. In order to meet this demand, a variety of heat treatments especially surface hardening techniques has been employed nowadays. The most commonly used include carburizing, shot peening, laser and induction hardening (IH).

1.2 Main Features of Induction Hardening

During induction hardening heat treatment, the work-piece is first quickly heated by an electromagnetic field to reach a specific temperature, with eddy currents and heat produced on the surface, and then followed by a rapid cooling usually quenching in a given medium until room temperature [1-3]. Owing to the fast speed of the whole IH treatment, only the work-piece surface goes through the phase transformation and consequently forms the strong phase, which, in most cases, is Martensite. The core material, however, still maintains its original state and thus keeps a good toughness. By

virtue of that, the final internal stress state left in the induction hardened part usually demonstrates a compressive residual stress in the surface layer, achieving the purpose of material surface enhancement.

In addition, IH treatment enables engineers to guarantee a desired shape of hardened contour by means of adjusting the IH process parameters [4]. For example, by varying the input frequency, power level (Fig 1.1) or heating time, one can make work-piece hardened only at specific locations of interest with a certain hardening depth [5]. It has been reported that the hardening depth can be roughly calculated based on the input frequency, current and heating time. A higher frequency could result in a thinner hardened layer whereas longer heating time can obviously promote the hardened case depth [6].

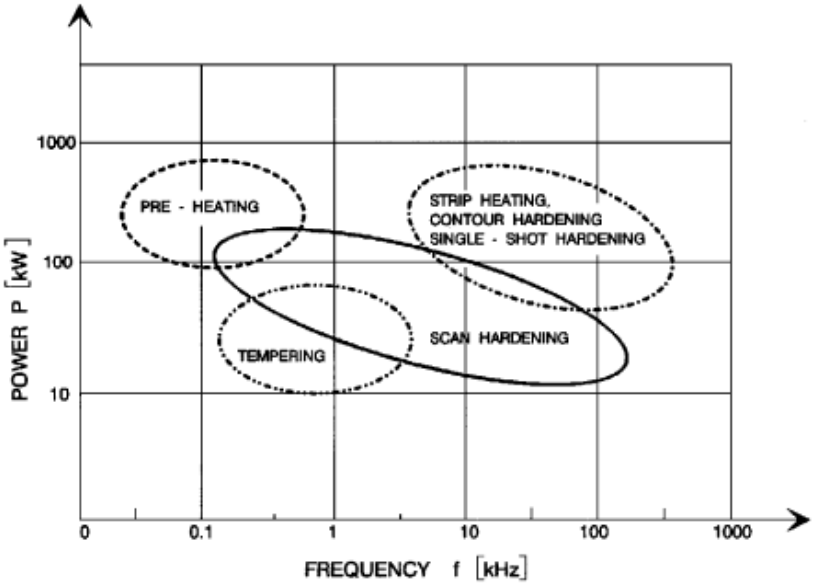

Fig 1.1 Power and frequency employed in various surface treatments [5]

1.3 Residual Stress and Distortion resulting from the Induction Hardening

In the past ten years, in order to well control the performance of the work-piece practical performance, significant amount of research has been focused on studying the correlation between IH process parameters and its resulting residual stress distributions, taking into account the key role of residual stress on the overall work-piece performance. Besides, it has been proven that any heat treatment undoubtedly leads to the appearance of sample geometry change (distortion) to various extents. Thus the distortions generated from IH should be also given considerable attentions and therefore it is frequently combined with residual stresses for specimen heat treatment effects analysis.

1.3.1 Residual stress measurement techniques

In the past, a number of techniques were explored for the purpose of describing the residual stress distributions resulted from different processes. These techniques can be basically divided into two groups: destructive and non-destructive [7, 8].

1.3.1.1 Destructive techniques

Destructive methods [9-11] are usually applied for bulk or surface stresses determination, depending on which specific technique is chosen. They are established on the basis of stresses relaxation theory and therefore are necessarily destructive. Materials are normally cut layer by layer and then the resulting strains are measured. In the majority of

previous works [13-17], an assumption that the layer removal process does not change the original stress state or generate extra stress was commonly used to simplify the complex stress status. So far, hole-drilling, ring-core (RC) and contour methods are the three broadly used destructive methods for detecting residual stress distribution [12]. Among them, contour technique, firstly induced for residual stress measurement by M.B. Prime [18, 19], has gained a lot of attention at present due to its favourable features of avoiding the complicated stress inversion work and calculating the released strain straightforwardly from the cutting position.

1.3.1.2 Non-destructive techniques

Non-destructive testing of residual stress is accomplished by measuring the change in the crystal size of the material [7, 8, 20]. They are capable to examine the residual stress distribution without damaging the parts. Diffraction techniques [21], including X-ray diffraction (XRD) and neutron diffraction (ND), have become the most commonly utilized non-destructive techniques to study residual stress nowadays due to their high accuracy and broad applications. Other methods, such as magnetic and ultrasonic approaches, are adopted for specific material stress investigations and depend on particular principles. For example, magnetic method [22] is based on the interaction between magnetization and elastic strain in ferromagnetic materials whilst ultrasonic

approach [23] is developed on the correlation between the velocity of ultrasonic wave propagation and the applied mechanical stresses on the material.

XRD [20, 24] is capable to show a high resolution over a small volume and reflect the in-plane stress state and thus it is more appropriate to uncover the sample residual stress state beneath the surface within a short distance. The main limitation of the XRD technique is in establishing the deep residual stress profile which is due to the low penetration depth of the X-rays compared with ND [25]. In most cases, with the assistance of a series of layer removal process, XRD can probe the residual stress distribution up to several millimeters but the stress relaxation after each layer removal step should be taken into account for the final stress correction. Until now, the most commonly adopted stress correction model was developed by Moore and Evan in 1958 [26]. This mathematical model enables the calculation of normal stress, which cannot be measured through XRD directly, from the other two measured stress components and therefore obtain the 3D residual stress state. Nevertheless, such stress correction work is still a rough estimation and the errors increase significantly with the increase in the investigation depth. Accordingly, the real measurement of specimen normal stress is necessary especially in the case of deep internal stress studies.

ND is a good alternative diffraction tool to examine the work-piece internal residual stress because of the strong penetration ability of neutrons. As such, ND can investigate the specimen internal stress up to several centimeters within the material and reveals a

complete 3D stress map directly from the experimental outcomes with a high spatial resolution [25, 27, 28]. In the same time, it avoids the questionable stress state recreated by the layer removal procedure followed in XRD. Normally, ND technique enables the residual stress measurement at close-to-surface depths of approximately 0.2mm down to inside investigation up to 25mm for steel [29]. However, for measurements at depths less than 0.2mm, XRD approach accompanied with layer removal process is more effective and is often applied.

The principle of residual stress determination by ND is quite similar to XRD; it characterizes sample stresses by virtue of measuring the change of atomic lattice spacing (d) at a specific lattice plane *{hkl}*. The lattice spacing (d) can be derived from the measured diffraction angle 2θ and the selected constant wavelength λ, by means of Bragg's law [11]:

$$\lambda = 2dsin(\theta) \dots\dots \text{Eq. (1)}$$

To obtain the residual strain value, ε, at each measuring point, the corresponding reference lattice spacing, in other words, the unstressed or stress-free lattice spacing d_0 should be known as well. It is usually measured from a reference sample which is assumed to be in a stress-free state. Then, the strain ε, which is the fractional change in atomic lattice spacing with respect to the stress-free lattice spacing d_0 is therefore calculated from:

$$\varepsilon = \frac{d - d_0}{d_0} \ldots\ldots \text{Eq. (2)}$$

Finally, the relevant residual stress can be calculated based on the generalized Hooke's law [11], considering the three stress components. Hoop stress (σ_H), axial stress (σ_A) and radial stress (σ_R), as in the following equations:

$$\sigma_H = \frac{E}{1+\nu}\left[\varepsilon_H + \frac{\nu}{1-2\nu}(\varepsilon_A + \varepsilon_R + \varepsilon_H)\right] \ldots\ldots \text{Eq. (3)},$$

$$\sigma_A = \frac{E}{1+\nu}\left[\varepsilon_A + \frac{\nu}{1-2\nu}(\varepsilon_A + \varepsilon_R + \varepsilon_H)\right] \ldots\ldots \text{Eq. (4)},$$

$$\sigma_R = \frac{E}{1+\nu}\left[\varepsilon_R + \frac{\nu}{1-2\nu}(\varepsilon_A + \varepsilon_R + \varepsilon_H)\right] \ldots\ldots \text{Eq. (5)},$$

where *E* is the Young's modulus and *v* is the Poisson's ratio.

The schematic layout of neutron diffractometer [28] for the residual stress measurement on a fastener sample is shown in Fig 1.2. As illustrated, the neutrons are generated from the nuclear reactor, directed to a monochromator which can provide a monochromatic beam of neutrons. Then, these neutrons are guided toward the target measurement location within the sample, diffracted from a group of specifically selected crystallite lattice planes of the material and finally received by a signal detector to provide the information of diffraction angle *2θ* of the lattice planes.

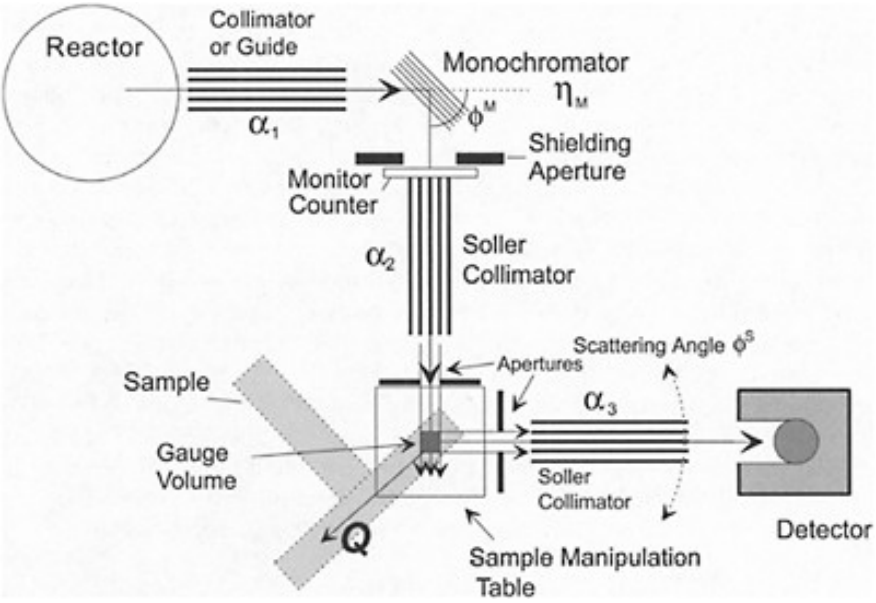

Fig 1.2: Schematic layout of a neutron diffractometer for residual stress measurement [28].

Additionally, some important points should be kept in mind in terms of residual stress measurement by ND method [27, 28]. Firstly, the residual stresses measured by ND are elastic stresses and the value obtained from each point is actually an average value over the whole sampling gauge volume, not the real stress at a point. Moreover, the ND determined residual stress should be considered as the macroscopic stress rather than the microscopic stress, since usually the sampling gauge volume of ND is so coarse that it cannot resolve the "phase-to-phase" and "grain-to-grain" or "in-grain" residual stress. Finally, given the high cost and relative time-consuming experiments, the necessity and effectiveness of the ND technique for residual stress investigation should be considered on a case by case basis.

1.3.2 Distortion measurement techniques

The heat treatment distortion measurements are usually accompanied with sample residual stress studies because the internal stress state can significantly determine the sample geometry variations. Usually, for obtaining the distortion generated by the whole heat treatment process (or only by a step of the heat treatment), the contour of the sample is needed to be measured before and after the whole heat treatment (or the certain step).

Up to now, the common techniques applied for distortion and sample surface location measurement includes non-contact techniques, such as laser scan which is widely used in thin mechanical part measurements, and mechanical contact technique which is more suitable for rigid and thicker work-piece surface detection, like the well-known CMM, the coordinate measuring machine [30, 31].

CHAPTER 2

Literature Review

2.1 Varied Induction Hardening Modelings for Part Distortion and Residual Stress Quantification

Varied modeling and simulation works have been carried out on IH process itself as well as residual stresses and distortion evolutions during IH. Yu et al. [32] developed a finite element model to calculate the residual stresses and distortion resulted from heat treatment and this model has been further developed by other researchers for investigating the IH parameters effects on residual stresses. Wang et al. [33] calculated the residual stresses as well as microstructure variations due to IH treatment. Denis et al. [34] presented a model of temperature/time change during IH heating and quenching stages and similarly, Longeot et al. [35] rendered the mathematical correlation between the generated electro-magnetic field in work-piece and the thermal features involved. Both models can allow one to predict the final residual stress and distortion distributions after IH treatment.

A typical residual depth profile of a laser surface hardened specimen made of AISI 1045 steel was reported by Yang and Na [36]. As shown in Fig 2.1, a comparison between the

calculated and the experimental residual stress in sample's longitudinal direction was made. This sample showed a compressive residual stress in the hardened layer, followed by a transition to tensile stress. The residual stress approaches to zero towards the core of the sample. Moreover, this result indicates that in the hardened layer, the calculated residual stress taking into account the Martensite transformation plasticity was closer to the experimental results than the one calculated without considering Martensite transformation plasticity which overestimates the magnitude of compressive stress near the surface. This finding was further supported by Yu et al. [32].

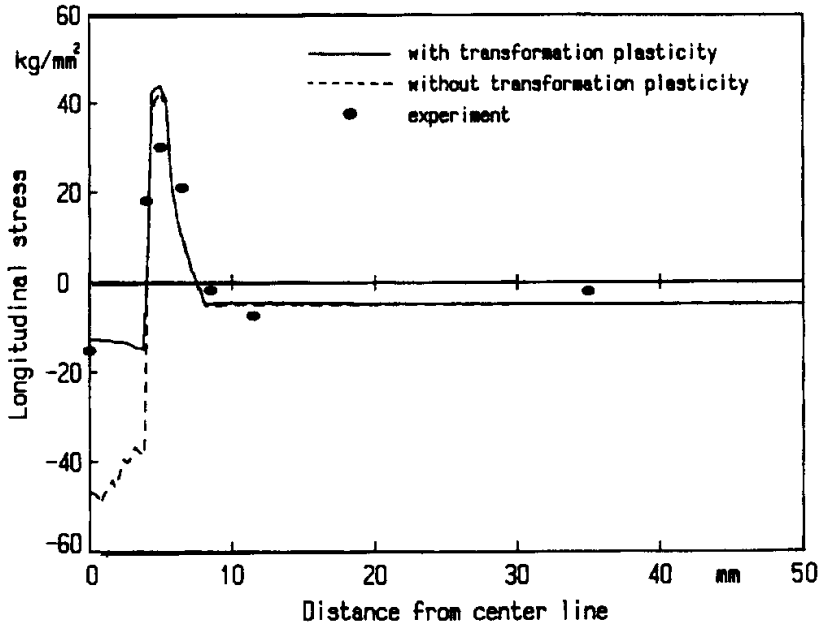

Fig 2.1: Experimental and calculated longitudinal (axial) residual stress on top surface in single pass laser surface hardening [36]

In order to have a deep insight of residual stress and distortion characteristics of real mechanical parts after heat treatment procedures, and to verify the modeling effectiveness,

considerable efforts have been put into experimental investigations on various heat treated pieces. These efforts will be summarized in the following sections.

2.2 Residual Stress Studies

A number of techniques including destructive and non-destructive were explored in the literature in the purpose of describing the residual stresses of various specimens.

2.2.1 Residual stress studies by destructive techniques

In 1933, Mathar [13] firstly presented a report in terms of residual stress measurement by means of hole-drilling method. A 12mm hole was drilled and the corresponding released strain was measured in his experiments. However, his works was restricted to uni-axial compressive stress field. During the following years, many relevant research works were done. Equations for bi-axial stress field were firstly developed by Mesmer in 1936 [37] and afterwards a great deal of efforts was put on strain gage sensitivity improvements. In 1956, an empirical way to solve the problems in blind-hole drilling application was proposed by Kesley [38]. Then, in 1972 and 1974, Beaney and Procter [39, 40] published two papers concentrating on the accurate measurement of residual stresses using center hole-drilling technique. They examined the influence of hole-drilling process and argued that the magnitude of extra stresses induced by hole-drilling is considerable, concluding that this technique produces unreliable residual stress values.

Consequently, many research works [41-43] were then carried out on the error analysis and accuracy improvement of hole-drilling technique used for residual stress measurement. Barsanescu and Carlescu [44] investigated the influences of hole-eccentricity on residual stress measurement and proved that the accuracy of hole-drilling has strong correlation with the eccentricity between the hole and the rosette center, and the accuracy of strain gages integration tendency correction. They established a new correction equation based on bi-axial stress state to improve the precision but still concluded that the hole-eccentricity cannot be avoided. At this point and also taking into account the complicated 2-D or 3-D spatial residual stress state, the present stress relaxation method, which is based on the complex stress-inversion principle, is not capable to reflect the real internal stress state, particularly in multi-dimensional cases [9]. Other types of stress-relaxation-based techniques, such as layer removal and sectioning, were proposed and used in work-piece internal stress investigations in later years [45]. Although they have advantages over the hole-drilling method, the unsatisfactory spatial resolution and the relatively intricate data analysis were also troublesome and limited their farther applications [12, 18].

Nowadays, a new stress relaxation technique, namely contour method [18, 19, 46, 47], has attracted a lot of attention, and its remarkable feature that the residual stress could be directly determined from the measured deformation has made it one of the most powerful techniques in residual stress measurements. Prime [48] gave a detailed explanation of the

principle of this method in his paper where he used contour method to explore a bent beam residual stresses as displayed in Fig 2.2(a) in 2-D map and (b) in 1-D curve. A good agreement between the bend test prediction and contour measured result in residual stress profile was found from both 1-D and 2-D figures. Afterwards, Prime et al. [49] employed both contour and ND methods to characterize the residual stress distribution in a butt joint which was made from two 25.4mm thick aluminum alloy plates, as demonstrated in Fig 2.3 and Fig 2.4. The authors compared the results and then stated that both contour and ND methods were capable to inspect the stresses with magnitude less than 0.05% of the elastic modulus. In addition, Zhang et al. [50] investigated the residual stresses around a cold expansion hole in an EN8 plate via contour method. A consistent result of hoop residual stress distribution between 2D contour map and 3D FE simulation was obtained, which confirmed the effectiveness of contour method in residual stress measurements. More studies on contour-determined in terms of residual stresses have been described elsewhere [51-53].

Furthermore, it has been noted that contour approach is particularly suitable in weld work-piece residual stress inspection, since in this case the unstressed spacing d_0 somewhat varies with depth and relatively hard to measure with a high accuracy, resulting in difficulties for applying diffractive methods (XRD and ND) which are based on the change of sample atomic lattice spacing d [21, 24, 27, 28]. However, despite of all

benefits contour method is still invalid if the testing samples should meet the non-destructive requirement.

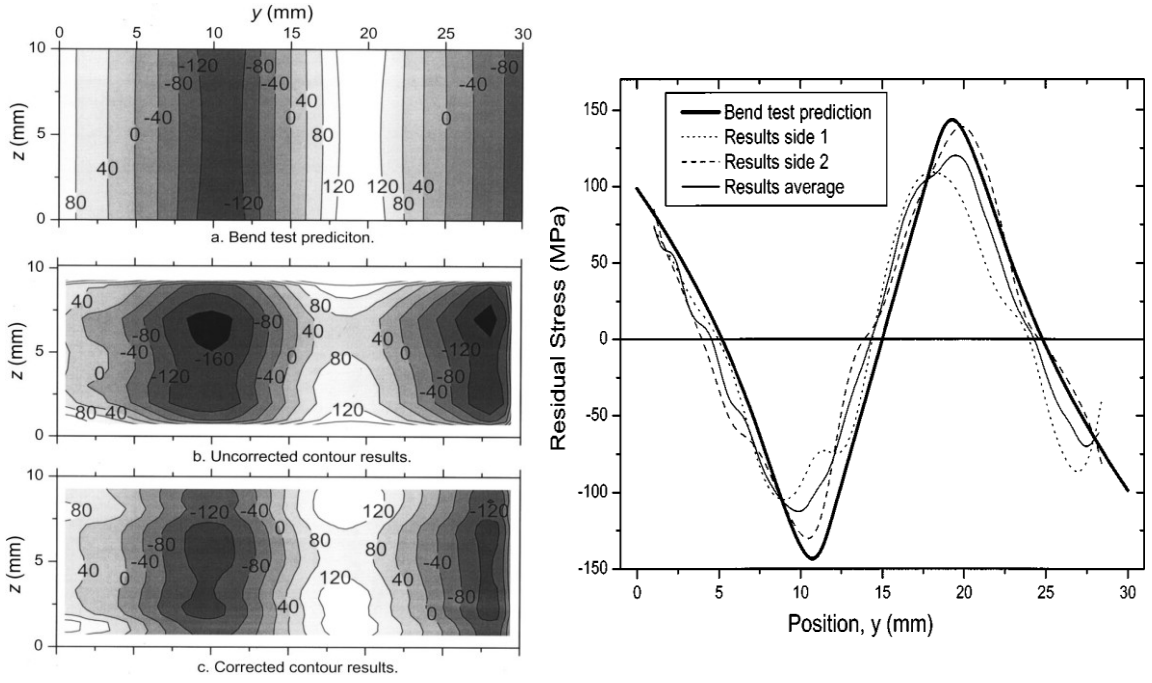

(a) (b)

Figure 2.2: (a) Cross-sectional residual stress map from contour method test on bent beam, stresses are in MPa; (b) 1-D residual stress results from contour method measurements of bent beam [48]

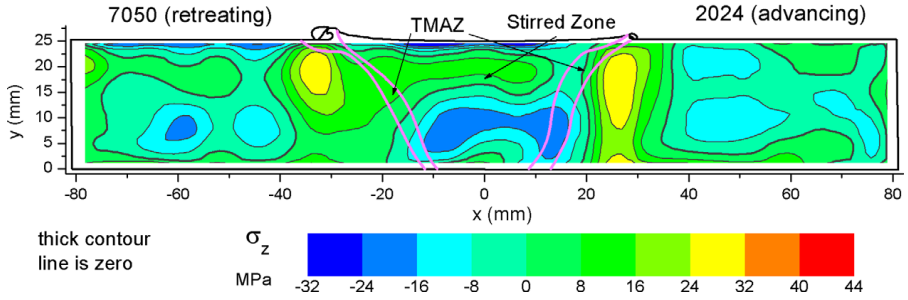

Figure 2.3: Residual longitudinal stresses measured in test specimen removed from FSW plate by contour method [49]

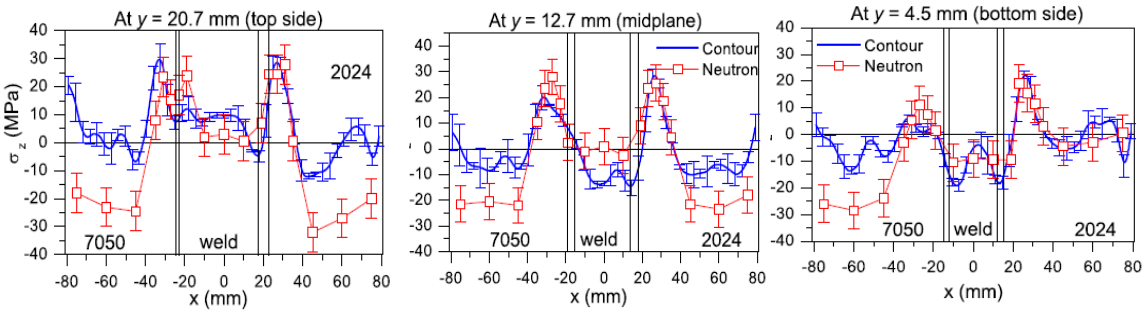

Figure 2.4: Neutron diffraction measured stresses plotted with contour results. Vertical lines indicate the stirred zone and TMAZ boundaries [49]

2.2.2 Residual stress studies by diffraction techniques

Meanwhile, abundant amount of work have been published regarding residual stress measurement by non-destructive approaches, especially by diffraction methods XRD and ND. The results were always used to compare with destructive methods, or, to verify the simulation models.

2.2.2.1 Using X-ray diffraction

XRD is more commonly and widely used for research studies because of its high accuracy in near surface area (≤10μm [29]) and short measuring time. Moreover, many reports agreed that, with regard to deep stress measurement by XRD, successive layer removal process is required because of the low penetration ability of electrons and its resulting stress relaxation should be taken into account for final stress correction [26]. Hornbach et al. [54] used XRD to measure the residual stresses of gear specimens (S/N 61, 63 and 65 are gear series numbers) owing to the IH process. They applied layer removal process to explore the stress in depth, comparing the uncorrected and finite

element analysis (FEA) and Flat-plate corrected residual stress distributions in radial direction, as shown in Fig 2.5. A significant difference between uncorrected and corrected residual stress magnitude was found and meanwhile an oscillation of residual stress was observed along the depth, which could be attributed to the complex variations of temperature distributions and cooling rates produced by IH. Similarly, Coupard et al. [55] examined the residual stress distributions in 2 batches of induction hardened cylindrical samples through XRD. An agreement between the finite element modeling (FEM) and the experimental data was concluded. In their work, Moore and Evan correction was adopted for stress relaxation calculation resulted from local and circumferential layer removal process. The relevant comparisons between simulation and XRD results for a hardened layer of 3mm in axial and circumferential directions are shown in Fig 2.6(a) and (b). They claimed that the agreement between FEM simulation and XRD measurement result can only be obtained at depths lower than one-tenth of the sample's diameter. For deeper depths, a reliable experimental correction is required.

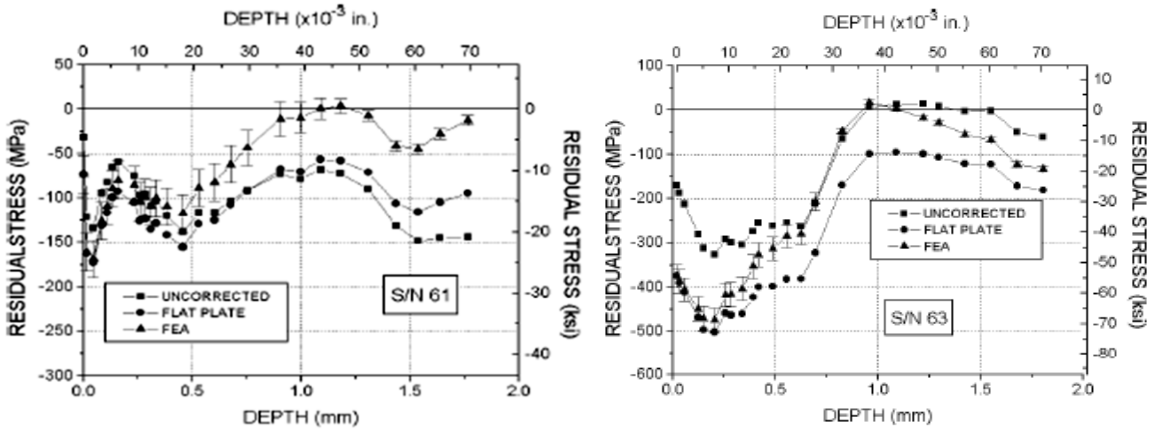

Fig 2.5: Comparisons of radial residual stress distribution between uncorrected and corrected results: (a) S/N 61 induction hardened gear; (b) S/N 63 induction hardened gear [54]

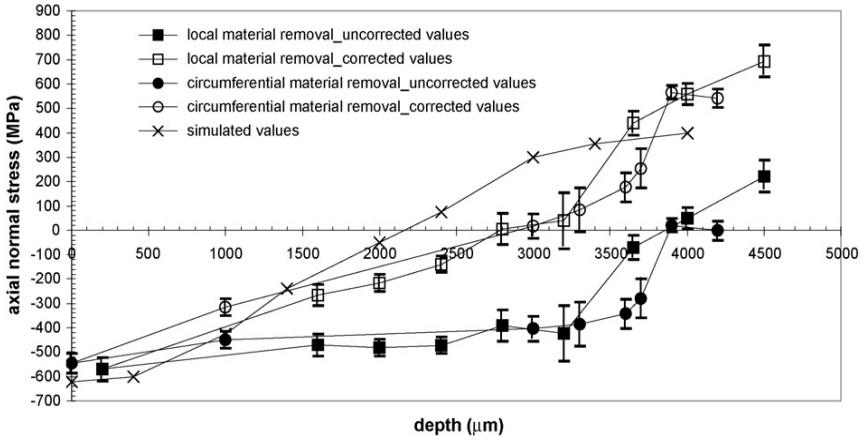

(a)

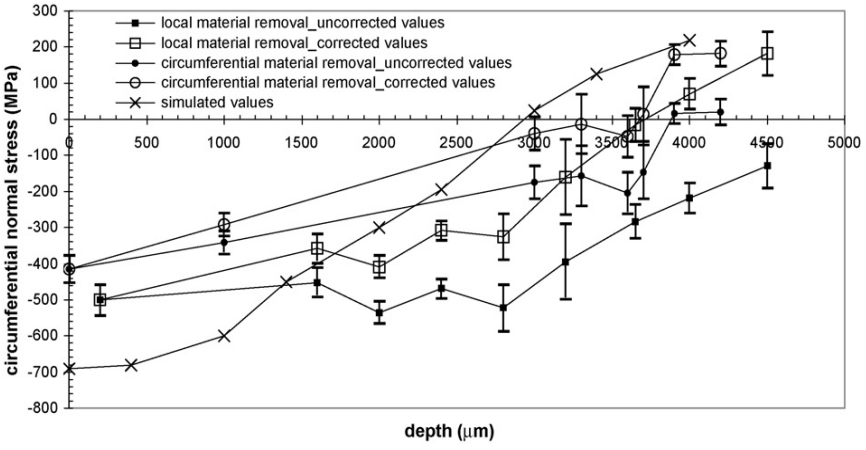

(b)

Figure 2.6: Corrected, uncorrected (measured by X-ray diffraction) and simulated normal residual stress profiles for both material removal techniques for hardened layer of 3mm: (a) in axial direction; (b) in circumferential direction [55]

More XRD-based near surface residual stress investigations on various samples were reported in the literatures [21, 56]. However, considering the required layer removal process and its resulting stress relaxation correction for XRD investigation, ND technique, undoubtedly, is more suitable and powerful in deep non-destructive stress detection.

2.2.2.2 Using neutron diffraction

Gür et al. [57] presented a model of residual stress depth profile along the radius of an oil-quenched Ck45 cylindrical sample. They compared their simulation results with the previous neutron diffraction (ND) experimental data obtained by Schröder [58]. The comparison, as indicated in Fig 2.7, demonstrated a high consistency between the simulation and the real measurement in both axial and tangential directions. Yet, Hossain et al. [59] also employed ND technique to examine the residual stresses in a quenched stainless-steel sphere and compared their results with FEM modeling. A good agreement between simulation and experiment was obtained. In addition, Marthandam [60] reported a consistent result of residual stress distribution of several structural steels between using ND approach and destructive ring-core (RC) method. Albertini et al. [61] determined the heat treatment effectiveness on a steel crown gear through ND. They confirmed that the ND-determined residual stress value at the closest point from the surface by the residual stress profile obtained by XRD. Consequently, it can be seen that ND technique can offer

a coherent result not only with the simulated models but also with XRD and other destructive methods.

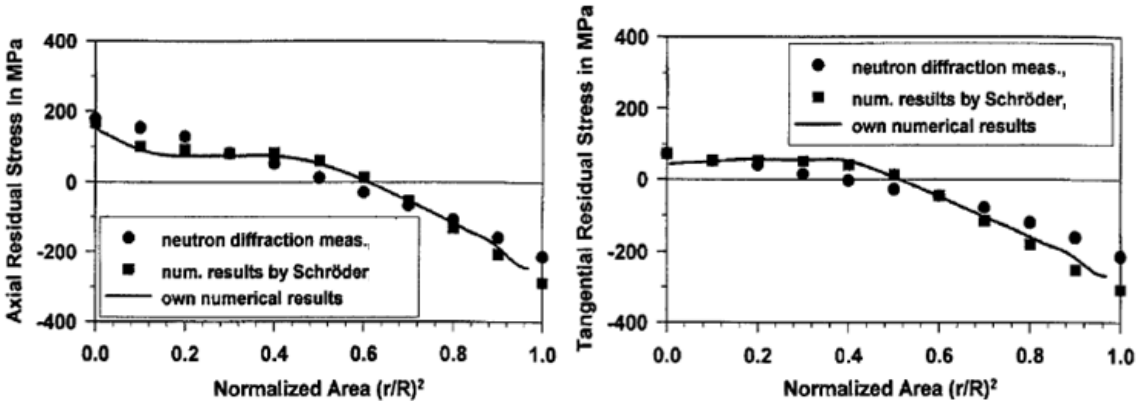

Fig 2.7: Comparison of numerically predicted residual stresses with neutron diffraction measurements and numerical results given by Schröder: (a) in axial direction; (b) in tangential direction [58]

2.2.2.3 Unstressed lattice spacing (d_0) investigation in neutron diffraction

Notwithstanding, above-mentioned residual stress measurements through ND were all based on a constant unstressed lattice spacing (d_0). As known, d_0 is dependent on the microstructures and once there is a change of microstructure within the investigated sample, the d_0 could alter. Paradowska et al [62] used a comb and a set of cuboids as the reference samples (Fig 2.8) to investigate the stress-free d_0 variations within the material by means of both ND and synchrotron XRD techniques. Their finding indicated that d_0 was almost not affected by the change of microstructure. The average variations obtained between the weld metal, HAZ (heat affected zone) and parent metal were no more than 0.0001Å, as given in Table 2.1. By virtue of that and considering the relative time-consuming d_0 reference sample preparation process, they finally claimed that there

is no great significance to measure the unstressed lattice spacing at least for weld sample residual stress determinations.

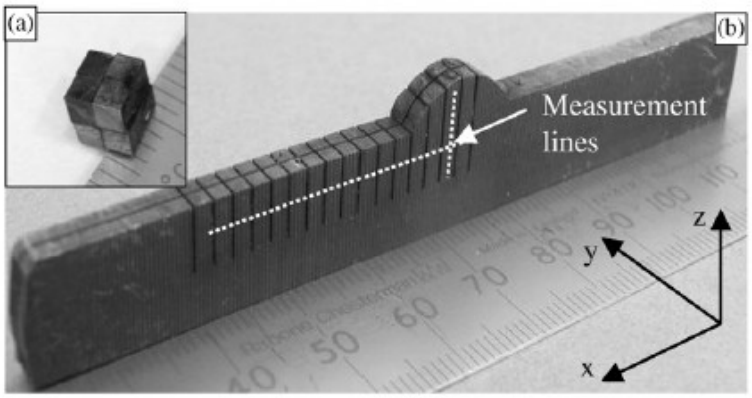

Fig 2.8 the reference samples for stress-free lattice spacing d_0 measurement: (a) set of cuboids; (b) comb [62]

Table 2.1 Stress-free lattice spacing measured at diffraction location by ND [62]

Specimen	Area of measurements	Local average d_0 (Å)	Statistically calculated error (Å)
Cuboids	Parent metal (PM)	1.18605	0.00007
Comb	Parent metal (PM)	1.18607	0.00007
	Heat affected zone (HAZ)	1.18600	0.00009
	Weld metal (WM)	1.18601	0.00009

However, Ezeilo et al. [63] argued that it is necessary to adopt appropriate d_0 values for ND stress measurement when the microstructure of specimen varies with depth. They carried out their residual stress studies on a 12% chromium Martensitic stainless steel after laser surface, giving a re-melted depth of 0.23mm. Using both ND and XRD approaches they compared the experimental results with the theoretical model. Fig 2.9 shows a quite good agreement in stress distribution between ND results which are based on a varied d_0 and the XRD results, as well as the theoretical model, in the near surface area. Significant differences of residual stress around ±200 MPa were observed in the

melted and heat affected zones of this laser treated specimen, one based on a constant d_0 and the other based on a varied d_0. This work proved that the stress-free lattice spacing d_0 plays an important role in ND residual stress determination and should be taken into consideration.

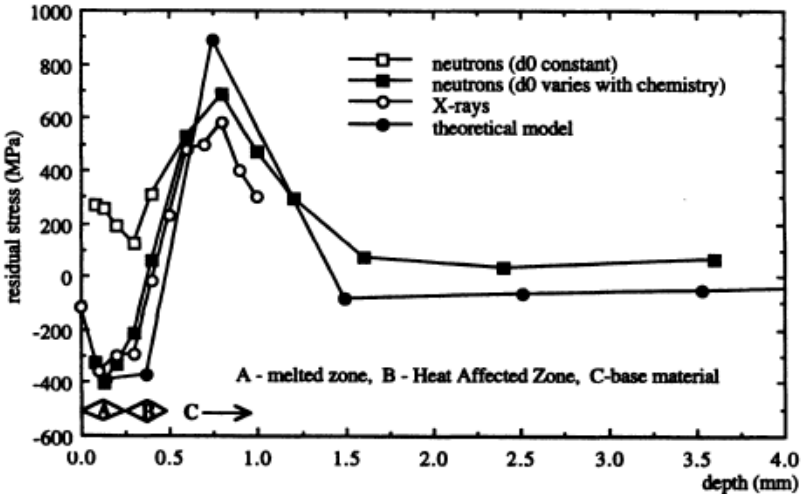

Fig 2.9 Comparison of ND- and XRD-determined as well as predicted residual stress in a laser treated sample (12% chromium Martensitic stainless steel) surface [63]

In present research, ND technique has been selected for specimen internal residual stress investigation, due to its favorable characteristics, such as non-destructive, deep penetration and no stress correction analysis is required. Considering that this residual stress measurement is performed on an induction hardened sample with microstructure changing from surface to core, there is a possibility of significant variation of unstressed lattice spacing d_0 along depth, which could affect the ultimate residual stress result to some extent. Consequently, the investigation work of d_0 variation along depth has been carried out in this study.

2.3 Distortion Studies

Distortion measurements on various samples have been reported by many researchers. Ramanathan and Foley [64] examined the quenching distortion profile of a set of Jominy bars made of nine steels with different chemical compositions using CMM. The distortion size and shape in terms of each investigated sample was reported and the general quenching distortion shape is depicted in Fig 2.10. As shown, the diameter enlarged after heat treatment while a contraction happened afterwards, forming an overall "hourglass" contour along the axis. This particular deformation pattern can be related to the material volumetric expansion (around 5%) which happened near the bar end during the quenching process owing to the Austenite/Martensite phase transformation, and the plastic deformations occurred during the phase transformation at the same time.

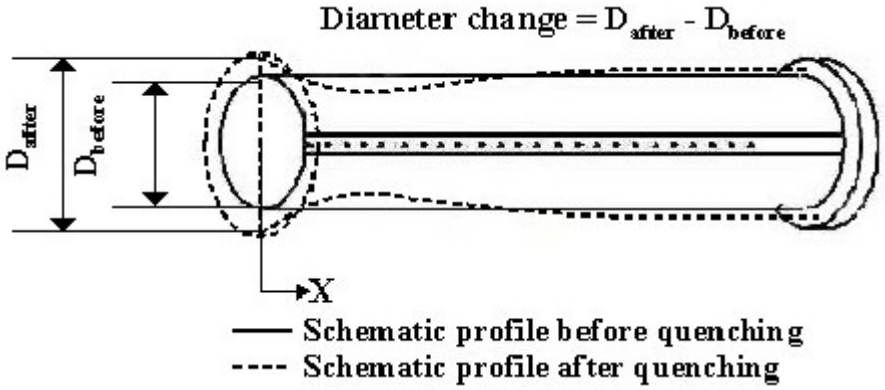

Fig 2.10: A typical schematic quenching distortion profile of a Jominy bar [64]

Thuvander [65] heat treated a ring die with radial grooves on one end surface made of tool steel K326. The whole heat treatment process included pre-heating to 500°C for 80mins, heating to 1100°C for 80mins, quenching in a fluidized bed at 15°C for 7.5mins

and finally tempering at 350°C for 60mins. Fig 2.11(a) displays the calculated and measured distortion profiles after quenching in terms of the radial groove sectioned at 45˚ and a very good conformity was observed. Fig 2.11(b) presents a comparison between calculated and measured distortions of ring die outer radius at mid-height around the ring (0˚-360˚), with and without tempering step. The results showed an angle-dependent variation of radius distortion size regardless of the tempered or non-tempered state. However, the non-tempered radius distortions were all negative, implying shrinkage at this state, whereas the tempered radius distortions are all positive which suggested a sever volume increase of the material during tempering.

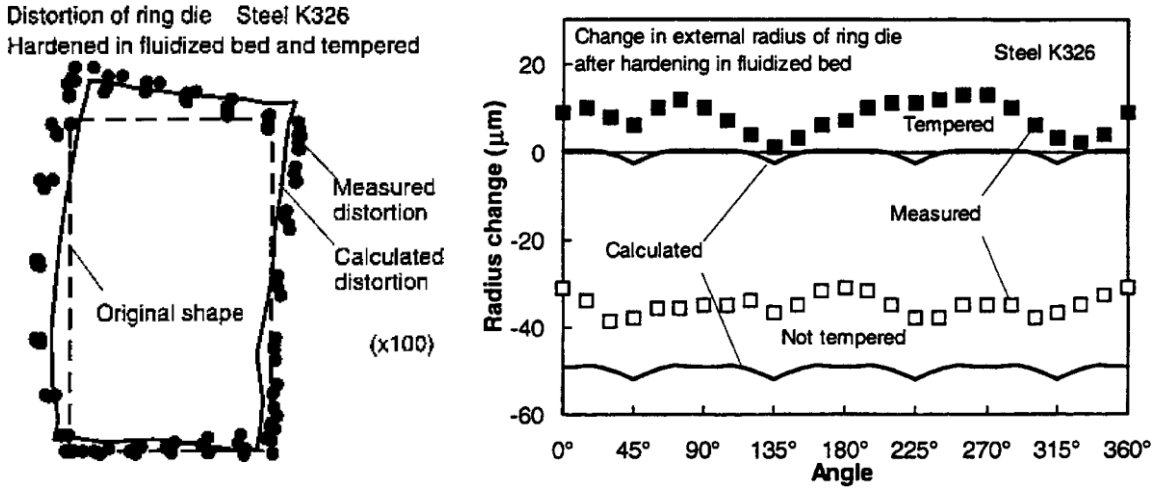

(a) (b)

Fig 2.11: (a) Measured and calculated distortion after quenching. The 4 sections at the positions at the 45˚from the grooves; (b) Comparison between calculated and measured distortion of the external radius at mid-height around the ring, with and without tempering. The angle is given from a point between two grooves [65]

Besides, Thuvander et al. [66] examined the difference of radial distortions of cylinder (Fig 2.12(a)) and tube (Fig 2.12(b)) samples between the simulation and the experimental

result by means of CMM. A clear radial distortion fluctuation around sample can be seen from both cylinder and tube specimens, which suggested a non-uniform distortion distribution. In addition, for the cylinder case the distortion profile is irregular whereas for the tube case the maximum distortion is found at 0˚ and the minimum was observed at the perpendicular direction 90˚.

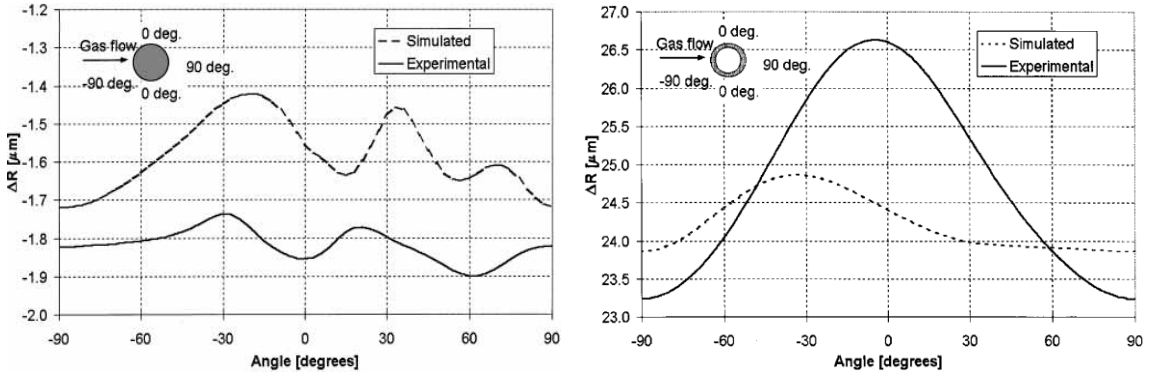

(a) (b)

Fig 2.12: (a) Radial displacement for a gas quenched *cylinder* with 2 different boundary conditions; (b) Radial displacement for a gas quenched *tube* with 2 different boundary conditions [66].

More distortion measurements by CMM have been described somewhere else [67-69], and the CMM-based surface coordinate measurement has usually been employed in residual stress determination through contour method for displacement calculation, as mentioned in related works [47-53].

It has been reported that, for the distortion measurements on the thin and flexible parts, mechanical contact techniques should be avoided since they may push or even damage the parts. However, the samples in present study are made of 4340 high strength steels with a moderate thickness around 7mm, which makes them suitable for both mechanical

contact and non-contact approaches. Considering many surface contour investigations have been done by CMM and have been documented in details in the literatures, the present distortion measurements are therefore carried out by the mechanical contact CMM technique, for convenience and also for comparisons with the previous distortion studies.

2.4 Objectives of the Present Work

Although a large number of residual stress and distortion experimental works has been reported in recent years, studying the residual stress distribution and distortion profile due to the IH treatment, is still needed due to the complex temperature evolution and cooling rate during this process. Moreover, since the change in the specimen geometry caused by IH is relatively smaller than that caused by traditional heat treatment, there are limited contributions describing the distortion caused by induction hardening and further relating it to residual stress distribution. This is the origin of the present study.

In the present work, the investigated samples are 7.0mm thick steel discs with approximately 106mm diameter and ND technique was chosen to measure the residual stress depth profile of the induction hardened disc. The distortion contour of investigated disc was established by measuring the coordinate system by means of CMM technique of a series of designed points on the three (top, bottom and circumferential) surfaces of the discs before and after the IH treatment. The Vickers micro-hardness is applied to uncover

the hardness distribution within the sample to provide a more across-the-board analysis of this disc specimen.

The present study aims at:

- Studying the effects of initial hardness and IH parameters on the distortion and hardening depth of a series of disc samples using CMM method.
- Determination of the 3D residual stress distributions on a selected disc sample by means of ND technique.
- Exploring the connection between the distortion, residual stress and the hardness depth profiles of a targeted disc sample.

CHAPTER 3

Experimental Procedures

The objective of the present research is to investigate the distortions and residual stresses introduced by induction surface hardening on target samples as well as the micro-hardness evolution in the hardened layer. 15 disc-shaped specimens in total were employed in distortion measurements and one disc (#7) was specifically selected for further residual stress and micro-hardness distribution explorations.

3.1 Material and Sample Geometry

Samples used in this study were made of AISI 4340, Nickel-Chromium-Molybdenum alloy steel. The chemical composition is provided in Table 3.1 [70]. This steel is especially known for its highest combination of mechanical strengths and ductility under the heat treated conditions, and therefore has been widely used in aerospace industry for the last 40 years [71].

The geometry of the samples is sketched in Fig 3.1. It is a 7.0mm thick disc with outside diameter of 106.1mm and inside diameter of 13.5mm. The surface roughness of the disc is required to reach $R_a \leq 6.3\mu m$ after the manufacturing process. 20 such discs were prepared and 15 of them were used (5 discs as backup samples) in the present work.

Table 3.1 Chemical composition of steel AISI 4340 [70]

Element	**Content (wt %)**
C	0.38 - 0.43
Cr	0.70 - 0.90
Mn	0.60 - 0.80
Mo	0.20 - 0.30
Ni	1.65 – 2.00
P	0.040 max
Si	0.20 - 0.35
S	0.040 max
Fe	Balance

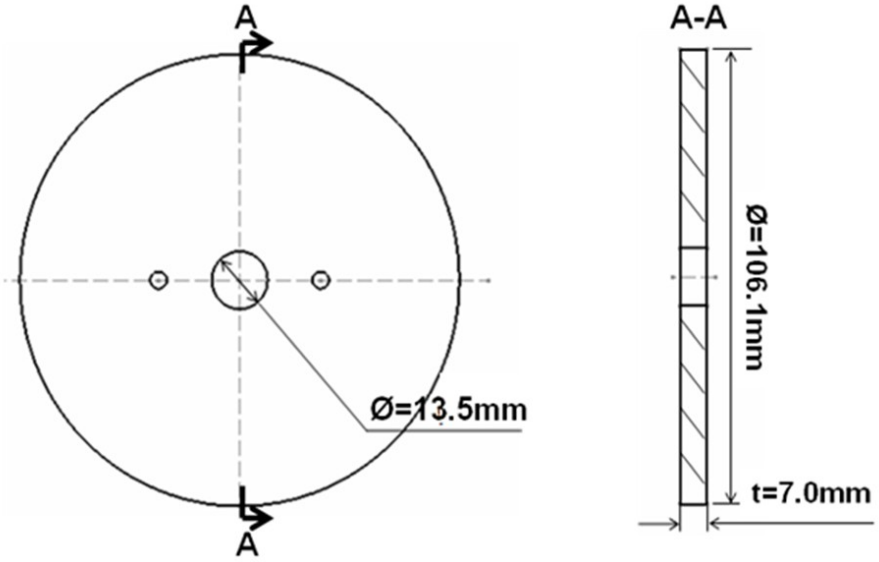

Fig 3.1 Specimen geometry (dimensions in mm)

3.2 Pre-Heat Treatment

All 20 disc samples are in 27HRC hardness (called inherent hardness) before the pre-heat treatment. Here, the purpose of pre-heat treatment is to provide these 20 discs with three different hardness (called initial hardness) values before undergoing the induction surface hardening, by means of varying the processing conditions.

Prior to the treatment, 15 discs were evenly divided into three groups, named group I, II, III. The 5 discs in group I were marked as disc #1 to #5 and similarly, the 5 discs in group II and III were marked as disc #11 to #15 and disc #16 to #20, respectively. Group I and II were targeted to reach a higher hardness (around 45HRC) and medium hardness (around 35HRC) level after the pre-heat treatment, separately. Group III was designed to have a lower hardness before the induction hardening and therefore 5 discs in this group was not subjected to pre-heat treatment. Considering that steel with hardness close to 45HRC is widely utilized in today's part surface engineering due to its relatively good mechanical properties [71] (compared with that of 35HRC and 27HRC), group I in present study was thus set as a key group for investigations. Additionally, the remaining 5 discs (marked as disc #6 to #10) serve as the backup samples for group I, namely group **I'**, in case of unexpected problems occurred on samples during the experiments.

During the pre-heat process, two furnaces, for heat treatment and tempering, were used. Samples in group I (disc #1 to #5) and backup group I' (disc #6 to #10) were firstly heated to 850°C for 45mins and then quenched in a mixture of water and 10% polymer quenchant (Aqua-Quench solution), followed by tempering at around 380°C for 1.5h and air cooling in the end to reach a hardness of 43HRC. Samples in group II (disc #11 to #15) went through the same heating and quenching steps as group I, except that the tempering stage was executed at 550°C with the duration of 2h. The final achieved hardness of this group is on the order of 35HRC. Group III was not subjected to any treatment here and

consequently the 5 discs (disc #16 to #20) kept their inherent hardness of approximately 27HRC. It is relevant to note that the material group III may have a different Martensite lath size than groups I and II as it did not undergo the same quenching sequence after the Austenitisation treatment.

Note that the above-mentioned macro-hardness values of three testing groups were obtained by investigating one of five samples from each group, considering the average of three macro-hardness measurements per sample. The hardness after pre-heat treatment was termed as initial hardness since it is the hardness before IH treatment, and pre-heat treatment results of three testing groups are specified in Table 3.2.

Table 3.2 Pre-heat treatment recipes for 20 disc samples

Testing Group	**Samples**	**Pre-heat Treatment**	**Inherent Hardness**	**Initial* Hardness**
Group I and Group I'	Disc #1 to #5 and Disc #6 to #10	-Heating at 850°C for 45mins; -Quenching in water + 10% polymer (Aqua-Quench solution); -Tempering at 380°C for 1.5h; -Air cooling	~27HRC	~43HRC
Group II	Disc #11 to #15	-Heating at 850°C for 45mins; -Quenching in water + 10% polymer (Aqua-Quench solution); -Tempering at 550°C for 2h; -Air cooling		~35HRC
Group III	Disc #16 to #20	Non-treated		~27HRC

* called initial hardness because it is the hardness before the IH process

3.3 Induction Surface Hardening

Pre-heat treatment provided three testing groups with three different initial hardness values (Table 3.2) before the induction hardening process was carried out. Therefore, the role of induction hardening here is to further treat all samples, enabling them to achieve a higher hardness value in the surface layer while maintaining the initial hardness in the core at the same level. However, the 5 discs in backup group (group **I'**) were not induction hardened at this time. They are intended to be induction hardened when there is a need for further experimental investigations on discs with initial hardness of 43HRC.

15 disc samples from group I, II and III were induction hardened using the same high frequency of around 200 kHz but with varying heating time and power to provide different IH recipes. For all samples, quenching stage was carried out in an Aqua-Quench solution (water + 12% to 12.5% polymer) right after heating without time delay until reaching a room temperature of approximately 25˚C.

The determination of IH parameters (heating time and power) applied to samples is not easy. It requires both simulation studies and the corresponding experimental verifications on IH process. The simulation work of disc's through-thickness hardened profile due to various IH recipes was done by Blut [72], a master student in ETS. The relevant experimental verifications were carried out by trying a series combination of heating time and power to explore the range of the disc's hardening depth that can be obtained in practice. Critical IH power values (maximum and minimum powers) were finally found

through the experiments and it was viewed as the basis for IH parameters' selection in present study. Briefly, in present study, the selection of IH heating time and power should ensure that the disc can be hardened without part melted, showing an integral hardened profile along the thickness after the treatment. In other words, it means the applied parameters must be able to generate a hardening penetration depth at the mid-thickness of the disc and meanwhile avoiding the probable melting occurring at the disc's corner, taking into account the edge effect [73] appearing during the IH process. Based on all above, the appropriate IH parameters for present work were finally decided.

The detailed heating time (in second) and power (in percentage of maximum power) selected for disc samples have been illustrated in Fig 3.2 and summarized in Table 3.3. It can be noted that, by virtue of IH treatment, the samples in three initial hardness groups can demonstrate various outcomes in hardness, distortion as well as residual stress distributions. This is the ground for afterwards experimental results analysis of these three aspects.

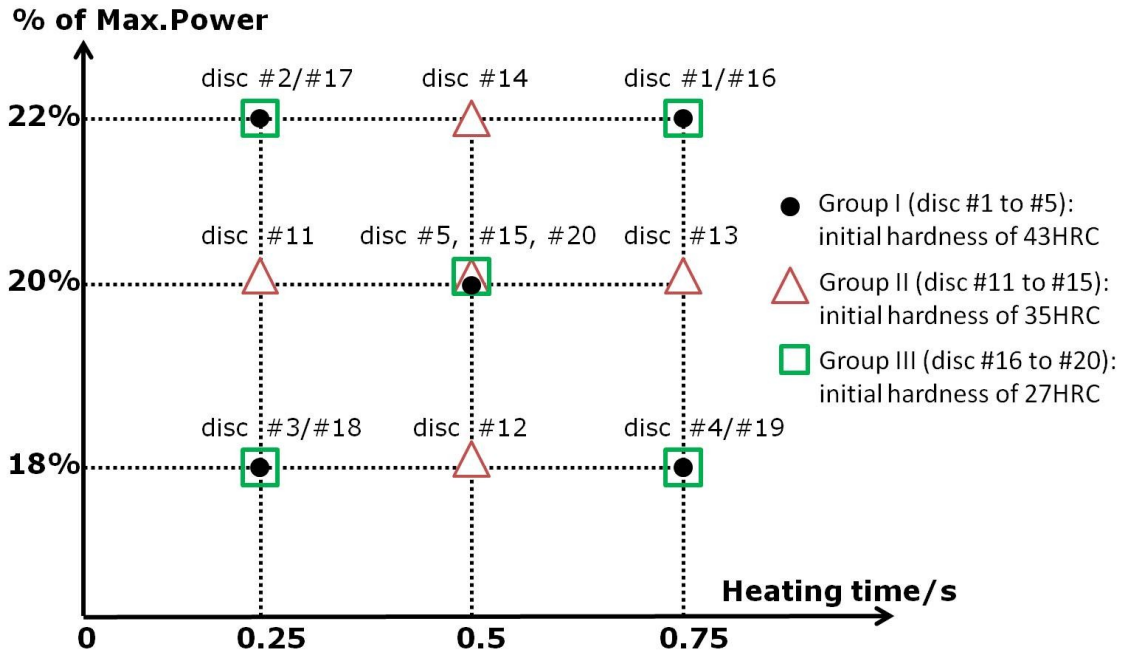

Fig 3.2 diagram of induction hardening recipes applied on 15 disc samples

Table 3.3 Induction hardening parameters applied on samples

Group	Sample	Induction Hardening Parameters			Initial hardness (HRC)
		Power* (%)	Heating time (s)	Quenching medium	
Group I (Disc #1 to #5) and Group III (Disc #16 to #20)	Disc #1 and #16	22	0.75	Water + (12% to 12.5%) polymer (Aqua-Quench solution)	Group I 43HRC; Group III 27HRC
	Disc #2 and #17	22	0.25		
	Disc #3 and #18	18	0.25		
	Disc #4 and #19	18	0.75		
	Disc #5 and #20	20	0.50		
Group II	Disc #11	20	0.25		Group II 35HRC
	Disc #12	18	0.50		
	Disc #13	20	0.75		
	Disc #14	22	0.50		
	Disc #15	20	0.50		

* is the percentage of maximum power

The induction hardening equipment set-up together with the real heating and quenching stages during the experiment are shown in Fig 3.3. As demonstrated in Fig 3.3(a), the disc sample was fixed on top of the cooling ring and positioned in the center of the

induction coil before the IH start. One function of the cooling ring is to carry the sample moving up and down to reach a suitable position for IH treatment. Also, since the cooling ring can self-rotate during the heating and quenching steps, as shown in Fig 3.3(b), it enables the disc a more uniform induction hardened layer.

The diameter of single induction coil used in present study is 109mm, which allows a coupling distance (the interval between the coil and the sample) around 1.5mm away from the disc sample (Ø=106.1mm).

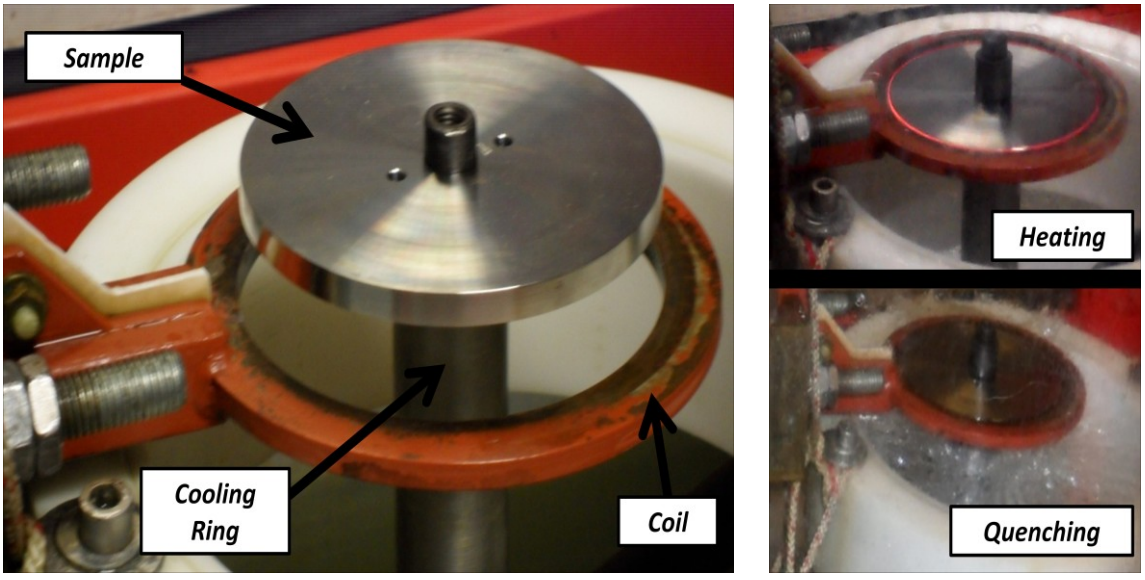

(a) (b)

Fig 3.3 Photographs of induction hardening process: (a) experiment set-up; (b) heating and quenching stages

3.4 Distortion Measurement

Distortion of the investigated sample is distinguished as the dimensional variations of the sample contour of each face (top, circumferential and bottom) of the disc. The

dimensional changes caused by the applied induction hardening process will be measured. For this purpose, the final distortion results are thus determined by measuring the profiles on disc's three faces before and after the IH treatment.

3.4.1 Examinations prior to the distortion measurement

Prior to the distortion measurements, a series of investigations were carried on disc samples to verify the real dimensions and surface roughness as well as the experimental repeatability. This is important because the accuracy of distortion result is largely dependent on the real condition of the investigated sample and the resolution of the equipment as well.

In present study, the dimensions of each disc were verified and documented. It was found that the real inside and outside diameters of all discs were very close to the nominal values shown in Fig 3.1. Whereas, the real thickness of the disc was 6.98mm, 0.2mm less than the nominal value 7.0mm.

In order to verify the real roughness of disc surface, the vertical deviations of the real disc surface from its ideal form was measured using a coordinate measuring machine (CMM). This result is demonstrated by both 2D surface maps and 1D linear graph provided in appendix III. The specifications of the CMM equipment are given in the next section-distortion measurement in this chapter.

The repeatability of distortion measurement by CMM has to be verified since it can be a source of error resulting from the measuring system. This work was performed by repeating the same CMM coordinate measurement on the same sample but after the sample re-setup (comparing the vertical coordinate value on disc's surface between first and repeated measurements). The best repeatability was found to be around 0.6μm and the average was less than 1μm. The details are also documented in Appendix III.

3.4.2 Distortion measurement by CMM

Distortion measurements on target discs were conducted by a Mitutoyo Bright-STRATO 7106 coordinate measuring machine (CMM), as shown in Fig 3.4, located in a temperature controlled laboratory at ETS. Mitutoyo's MCOSMOS software is run simultaneously with the contour measurement so that one can monitor the progress and interacts with the machine, if necessary. This CMM equipment is a moving-bridge type CMM with improved high accuracy in the 1μm range. The resolution of this equipment is close to 0.1μm and the best experimental repeatability has been proved to be 0.6μm.

A most functional motorized head mount (PH10M) combined with a high-accuracy touch-trigger measuring head (TP200) was particularly assembled for present CMM system. Such measuring head system configuration provides totally 720 repeatable positions for samples contour investigation and can give relatively small measuring angle increments of 7.5˚ only. Additionally, an automatic probe changing system is available

for this system, which enables a completely surface coordination measurement without interruption until the end. The probe used in present study is a ruby ball (Ø=1.5mm) with the probe stem of 20mm. This selection is mainly based on the consideration of operating the CMM measurement on disc's bottom face. As can be seen from the third image of Fig 3.4(b), in order to perform the CMM measurement on the bottom face, the probe stem has to be parallel to the bottom face, and has to be long enough to carry the probe moving towards the disc's center without any possible collision. Considering the measuring length along the radius of the disc is around 10mm (the detailed plan of the CMM measuring point distributions on disc samples will be discussed next), the probe stem finally used was 20mm. It should be noted that the probe diameter (Ø=1.5mm) was not chosen separately, which corresponding to the probe stem applied.

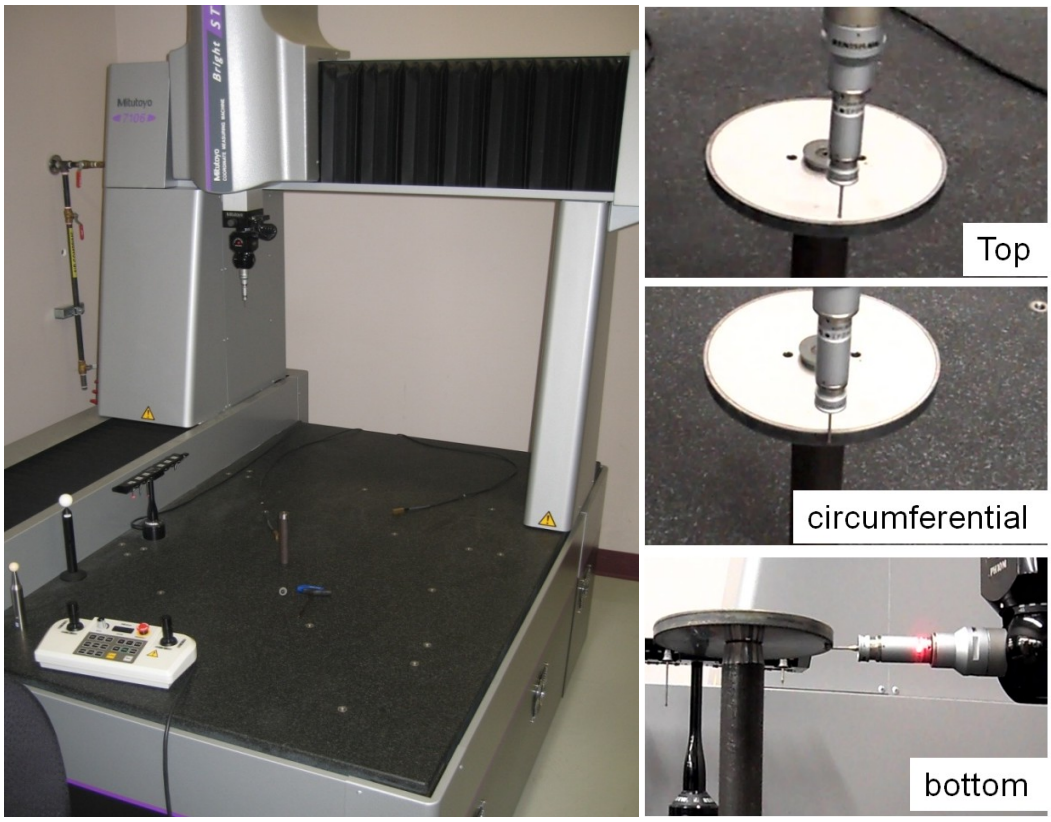

(a) (b)

Fig 3.4: Photographs of (a) CMM measuring system set-up; (b) ongoing CMM contour measurement on sample top, circumferential (lateral) and bottom faces

As reported by numerous researchers [1-5] and displayed in Fig 3.5(a), the induction hardened disc has a hardened layer within only few millimeters from the circumferential surface, due to the well-known current "skin-effect" occurring during the IH process. Commonly, this short-range hardened layer can be seen as the main place where the part dimensional variation (distortion) happens. This is because the sample's volume change, which is caused by the material Austenite to Martensite phase transformation, and the associated plastic deformations take place in the hardened layer, during the IH treatment. Based on above, all disc distortion investigations in present study have been designed to only measure the variations in the coordinates of the points that are located on the top or

bottom face of the disc within a range of nearly 10mm from the circumferential edge. This arrangement is demonstrated by the distributions of a series of lines (each line consists of many points) in Fig 3.5(b).

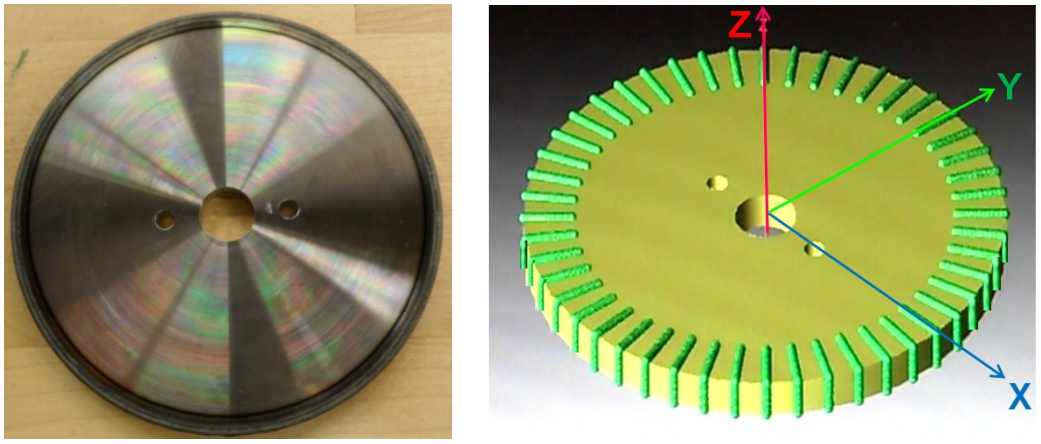

(a) (b)

Fig 3.5: (a) A photograph of a typical induction hardened sample and (b) its schematic diagram of measuring points distributions on each face

Same distributed patterns of measuring points were used on disc top and bottom faces for contour exploration, giving totally 2880 points on each face, while for circumferential face total amount of 528 measuring points were utilized. 48 measuring angle steps (at each measuring angle there is a measuring line) were distributed evenly on disc top/bottom face around disc center with interval of 7.5˚. Each measuring line comprises 60 measuring points. The point coordinate system measurement via CMM was carried out along the radial direction towards center of the disc. The first measured point of each line was located at a radial depth of 0.15mm from the disc circumference. This 0.15mm spacing, sometimes called security length, was set to ensure that the probe touching tip

can definitely land on the sample surface, taking into account the possible dimensional variations of the disc preventing the possibility of damaging the probe.

Fig 3.6 illustrates the measuring point layout on the disc's three faces in detail. As can be seen, for obtaining a clear distortion profile across the hardened layer, totally 50 measuring points were equally spaced in the range of 5mm with 0.1mm between them, followed by 10 points with a larger constant interval of 0.5mm. For the circumferential face, similarly, 48 measuring angle steps (48 measuring lines) were uniformly allocated around the disc center with internal angle of 7.5˚ while 11 points with an equal spacing of around 0.6mm were laid along each measuring line. Likewise, a security distance of 0.15mm was set for the same reason at the two ends of each measuring line.

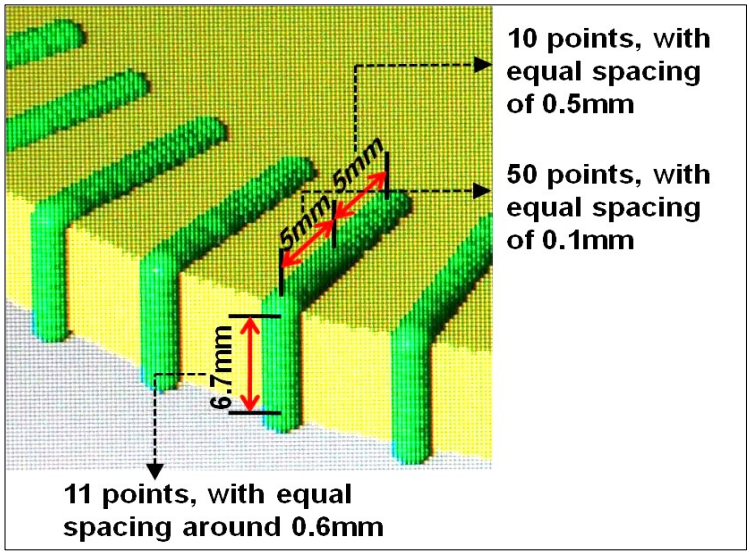

Fig 3.6: Measuring points layout on the top (bottom is the same) and lateral faces

3.5 Residual Stress Determination

3.5.1 Unstressed reference sample preparation

For obtaining the knowledge of stress-free lattice parameter (d_0) distribution required in stress measurement by ND technique, the reference sample which subjected the same heat treatment procedure of the targeted disc (used for stress measurement) is needed. Considering the ND-based stress measurement is a relatively time-consuming work, only one disc (disc #5) from the key group I and one disc (disc #7, which was induction hardened by the same recipe of disc #5 before ND measurement) from the backup group I' were selected for present ND investigations. Disc #7 was used as the targeted sample to perform the ND stress measurement while disc #5 was used to manufacture a "comb"-shaped reference sample to establish the unstressed lattice parameter (d_0) depth profile for the targeted sample (disc #7).

The reason for choosing disc #5 (and disc #7) for current ND study is based on the consideration of the particular IH recipe applied to. As mentioned in previous section, the IH recipe applied to disc #5 (same for disc #7) was 20% of maximum power with 0.5s heating time. It was the same recipe also applied to disc #15 of group II and disc #20 of group III, and therefore this recipe becomes the only mutual recipe that shared by three hardness groups. The significance of present ND study on disc #7 (and disc #5) is that, in the future ND stress investigations, it will be interesting to explore the initial hardness

effect on the residual stress under a fixed IH recipe, by making comparisons between disc #7 (initial hardness 43HRC), disc #15 (initial hardness 35HRC) and disc #20 (initial hardness 27HRC).

The preparation of the comb reference sample was made to cut along the radius of disc #5, so as the depth profile (along radius) of the stress-free lattice parameter (d_0) can be established. In practice, the comb cutting process was performed by wire electro-discharge-machining (wire EDM or WEDM) technique [74], using a brass wire diameter of 0.01inch (around 0.25mm) for rough comb side cutting and a SW-A zinc coated wire diameter of 0.004inch (around 0.10mm) for fine comb-teeth machining. The specifications of WEDM parameters applied in this work are provided in Table 3.4 while the detailed drawing of the comb design and its dimensions, and the photograph of the actual comb are shown in Fig 3.7 (a) and (b), respectively.

Table 3.4 WEDM input parameters set-up

EQUIPMENT: WIRE EDM CHARMILLES ROB.300		
Input parameters	**40 Comb-teeth cutting**	**Comb side-cut**
Wire material	SW-A zinc coated wire	Brass wire
Wire diameter (inch)	0.004	0.010
Voltage (volt)	80	80
Pulse duration (μs)	0.3	1.0
Time between 2 pulse (μs)	14.0	18.0
Short pulse time adjust (μs)	0.2	0.5
Ref. speed (mm/min)	2.0	10.0
Ref. average voltage (volt)	50.0	44.0
Injection pressure-bar (per unit)	1.0	2.0
Wire speed (mm/min)	6.0	6.0
Wire tension (per unit)	0.38	1.0

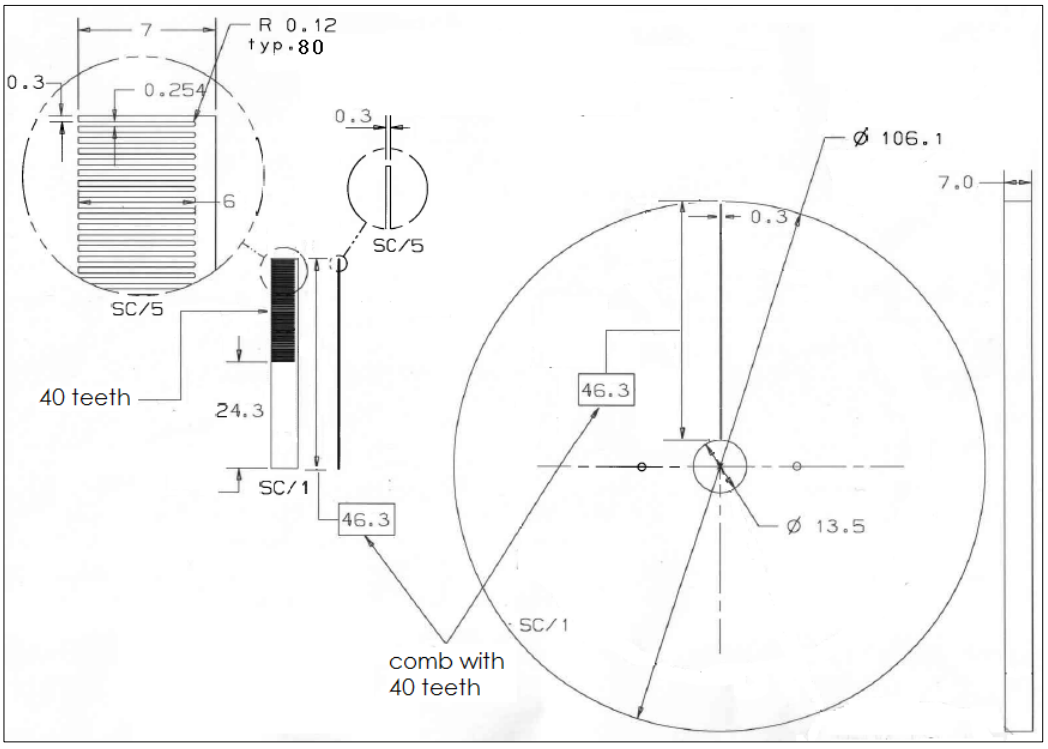

(a)

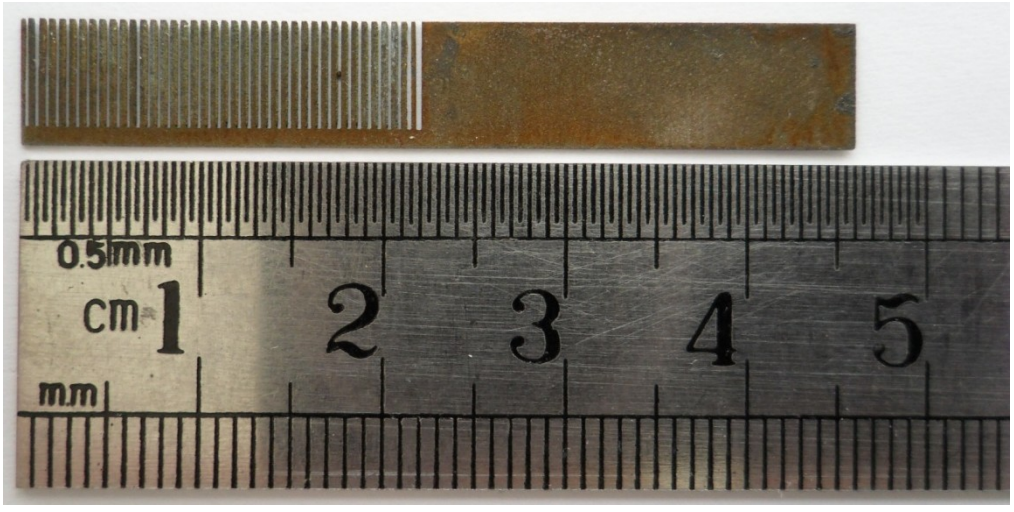

(b)

Fig 3.7: The stress-free reference comb sample (a) schematic design (dimensions in mm); (b) real photograph taken after WEDM

3.5.2 Neutron diffraction investigations

Neutron diffraction (ND) measurements were carried out using L3 neutron diffractometer at NRU reactor at Chalk River Laboratories, Ontario, Canada. The general layout of the ND experiment for comb and disc samples is demonstrated in Fig 3.8. The incident and diffraction neutron beams were limited by two slits and the sampling gauge volume (SGV) was defined by the intersection of these two beams as well as the selected gauge height. Through a computer-controlled translation and rotation system, the testing sample can be moved to a position that the SGV covers the part of interest within the specimen [27, 28].

The *{115}* planes of a single-crystal monochromator, germanium (Ge), with a monochromator diffraction angle (θ^m) of $2\theta^m \approx 98.77^\circ$ were particularly chosen to provide a neutron beam with a fixed wavelength λ of 1.653 Å. The α-Fe *{112}* reflection with a detector angle φ (2θ) of approximately 89.9˚ was used for diffraction pattern analysis. A 32-wire based multiple detector spanning an angle of 2.54˚ was employed for neutron detection and 1.00˚ oscillation angle was adopted during the neutron counting process in order to involve enough diffraction grains of the aimed specimen. Since the counting time can significantly influence the measurement accuracy, the neutron counts were continued until a clear diffraction peak was observed.

Additionally, prior to the ND stress investigation, the applied neutron wavelength λ had been calibrated by standard Ni powder. Also, the wall scans [75] were carried out on both

comb and disc samples before the stress measurement, in order to make sure the sampling gauge volume would be centered within the sample thickness.

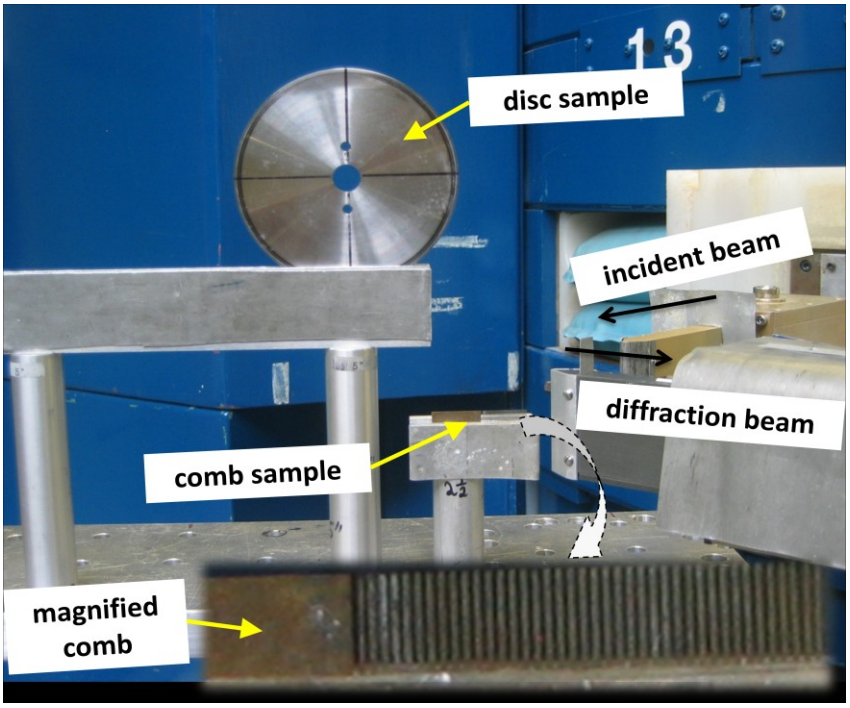

Fig 3.8 ND measurement layout for disc and comb (with a magnified view) sample

3.5.2.1 Unstressed lattice spacing (d_0) measurement

The reference comb is composed of 40 ($0.3\times0.3mm^2$) teeth as indicated in Fig 3.7, however, only the first 10 teeth were used in unstressed lattice spacing (d_0) investigations. This is because the thickness of the hardened layer was found to be less than 2mm and 10-teeth length is around 5mm twice the length of the rough hardening depth. Therefore, it is expected that a nearly constant d_0 value exists over the region farther than 10-teeth depth. Considering this and also because of the relative time-consuming data collection

of the neutron diffraction experiment, the stress-free lattice parameter investigation of the 30 remaining teeth was not pursued.

The detailed ND set up for comb reference sample is depicted in Fig 3.9. The already defined SGV was defined by two slits (one slit defines the incident beam size and the other defines the diffraction beam size) with 0.3mm width and 4mm height. As shown, the ND measurement was performed on the comb along a traverse line (the measurement line) from the first tooth to the tenth. The center of the SGV was located at tooth mid-height and in the center of each investigated tooth. The diffraction peak profile measured at every tooth was made of 32 points and was then fitted to a Gaussian profile with a flat background for finding the diffraction angle location, full-wide at half-maximum (FWHM) as well as the integrated intensity. Afterwards, this obtained diffraction angle result was related to the corresponding unstressed spacing d_0 using Bragg's law (Eq. (1)). Therefore the d_0 profile along the disc radius has been achieved. In fact, two d_0 profiles were acquired: one is d_0 profile in the hoop direction and the other is in the radial direction.

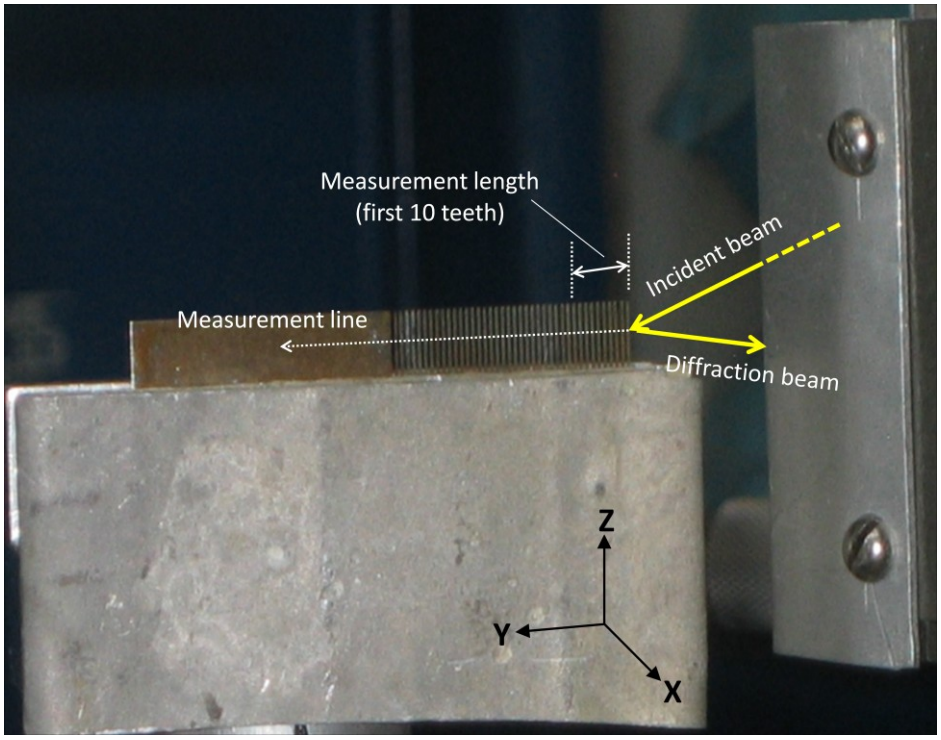

Fig 3.9 ND set-up of comb sample for unstressed parameter d_0 investigations

3.5.2.2 Residual stress determination

The general ND set up for residual stress measurement of disc #7 is illustrated in Fig 3.10. As shown, ND measurement was carried out at disc mid-thickness along disc radius (the measuring line) from a very near-circumferential-surface position, starting at a depth of 0.2mm, until 5mm inside the material, approximately. Equal measuring step of 0.1mm was adopted in the first 2mm below the circumferential surface while 0.5mm in the following 3mm, giving 25 measuring points in the range of 5mm investigated depth.

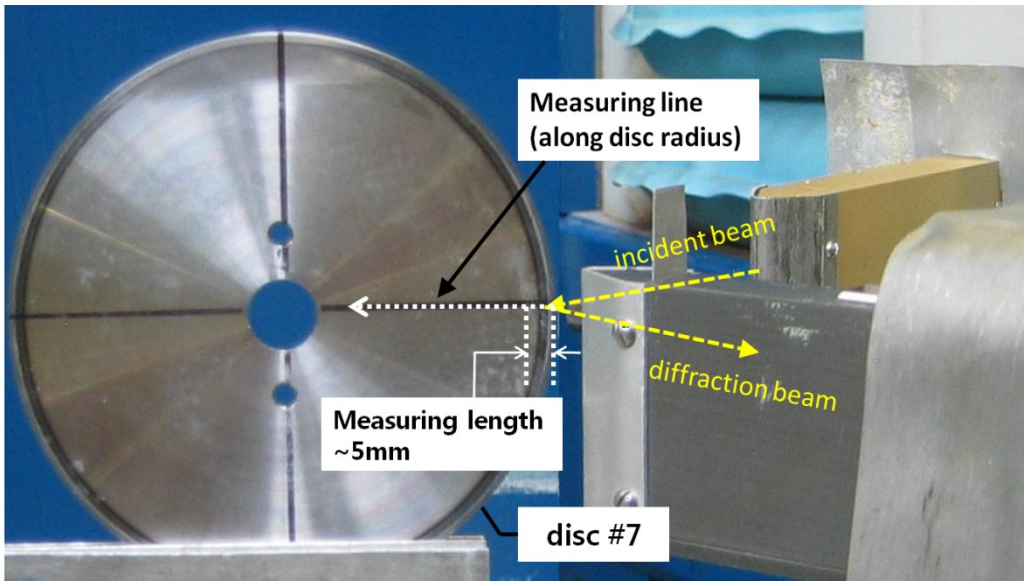

Fig 3.10 ND set-up for residual strain measurement of disc #7

The SGV for disc sample was defined by two slits width and the gauge height chosen based on the measuring direction. For disc radial residual strain investigation, taking into account the limitations arising from the strain gradient and the relative small measuring step, 0.3mm width of slits was specially selected with 4mm gauge height, and hence the SGV was 0.36mm^3 (0.3×0.3×4). For disc hoop and axial strain evaluation, wider slits of 3mm with 0.3mm gauge height was adopted, resulting in a larger SGV of 2.7mm^3 (3×3×0.3) in these cases. This was possible because the limitations in attempting to measure the residual strains in these two directions only constrained the gauge height. The illustration of the SGV dimensions and the corresponding measured residual strain in axial, hoop and radial directions is given in Fig 3.11(a) to (c). The detailed explanation of the SGV size determinations for present ND study is provided in Appendix I.

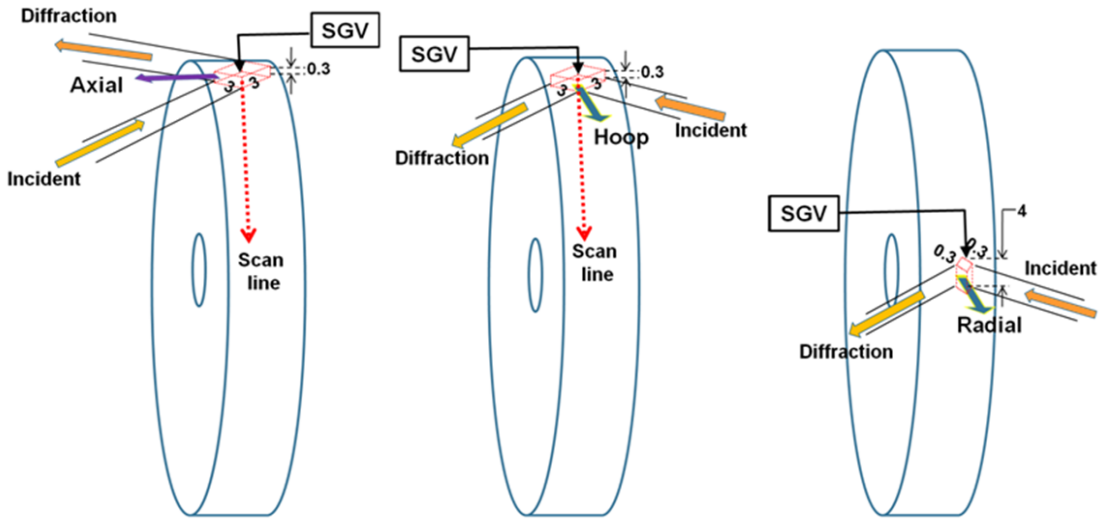

(a) (b) (c)

Fig 3.11 Schematic drawing of SGV dimensions and the corresponding measured residual strain direction: (a) axial scan; (b) hoop scan; (c) radial scan

Moreover, regardless of the direction in which the strain is measured (radial, hoop or axial), the measured diffraction peak profile at every measuring step was composed of 32 points within the first 2mm from disc circumferential surface and 60 points after 2mm. The peak profile was then fitted to a Gaussian curve with a flat background to obtain the diffraction angle location, full-width at half-width-maximum (FWHM) as well as the integrated intensity.

Afterwards, this diffraction angle result was linked to the relevant unstressed spacing d_0 profile obtained from previous comb specimen according to Bragg's law (Eq. (1)). As a consequent, the residual strain profiles in three directions along the radius have been fulfilled. Finally, by virtue of the Hooke's law (Eq. (3), (4) and (5)), the corresponding residual stresses can be calculated from the obtained strains. It should be noted that there

are few assumptions when applying the Hooke's law in present work. Firstly, the investigated sample is assumed to be the isotropic material and only the elastic deformation happens on the sample. Additionally, the Young modulus (E) and the Poisson ratio (v) are both assumed to be independent of the measuring direction.

3.6 Surface Etching and Vickers Hardness Test

3.6.1 Surface etching investigation on testing group I, II and III

It should be noted that all disc samples in present study, except disc #7, were only performed surface etching method to roughly estimate the relevant induction hardening depth, instead of applying Vickers hardness test along the disc's radius. This is mainly under the consideration that, disc #7 was the only disc investigated by ND and therefore can be used as a key sample to explore the relationship between distortion, residual stress and hardness distributions along the disc's radius. Regarding the 15 disc samples from group I, II and III, since all stress data are currently not accessible and the Vickers tests for 15 samples are also time-consuming to some extent, the etching method was finally employed to give a general idea of these discs' hardening depths.

In practice, these 15 induction hardened discs were etched using 2% Nital solution after finishing the distortion measurements. The etching process was carried out on the edges of both top and bottom faces of each disc sample, at 0˚and 180˚, respectively. Each data

was the averaged value (mean) of three measurements. The measurement error was calculated in percentage form using the following formula:

$$\delta_x\% = \frac{\Delta X}{X_m} \times 100\% = \frac{|X_{meas.} - X_m|}{X_m} \times 100\% \ \ldots\ldots \text{Eq. (6)},$$

where δ_x = measurement percentage error, ΔX = the measurement absolute error, $X_{meas.}$= measured value, X_m = mean value of all measurements.

The final etching results, that is, the rough hardening depths of these 15 discs, were further used to explore the effects of the initial hardness and the IH parameters on the final hardening outcomes

3.6.2 Vickers micro-hardness test on disc #7

As for disc #7, after finishing the residual stress measurements using ND technique, it was used to carry out Vickers micro-hardness examination using a load of 200g. In order to establish the relationship between micro-hardness and residual stress profiles of the same sample, the hardness test was performed following exactly the same measuring line of the residual strains measurement. It was carried out at disc mid-thickness position, along the radius from 0.2mm (Fig 3.12) below the circumferential surface to approximately 5mm depth inside. Besides, two additional Vickers hardness measurements were also conducted with the same range of depth (0.2mm to 5mm) and the same load of 200g. As can be seen from Fig 3.12, regarding these two cases, one measuring line was located in the top-thickness (0.15mm below the disc top face) while

the other was positioned in the bottom-thickness (0.15mm away from the disc bottom face). Furthermore, for the purpose of investigating the uniformity of hardness distribution around the disc, these three hardness tests mentioned above were duplicated at their opposite side across disc center. The error calculation is similar to that given in last section (3.6.1), using Equation (6). All Vickers hardness measurements were carried out on the small cross-section samples cut along disc thickness at the target positions.

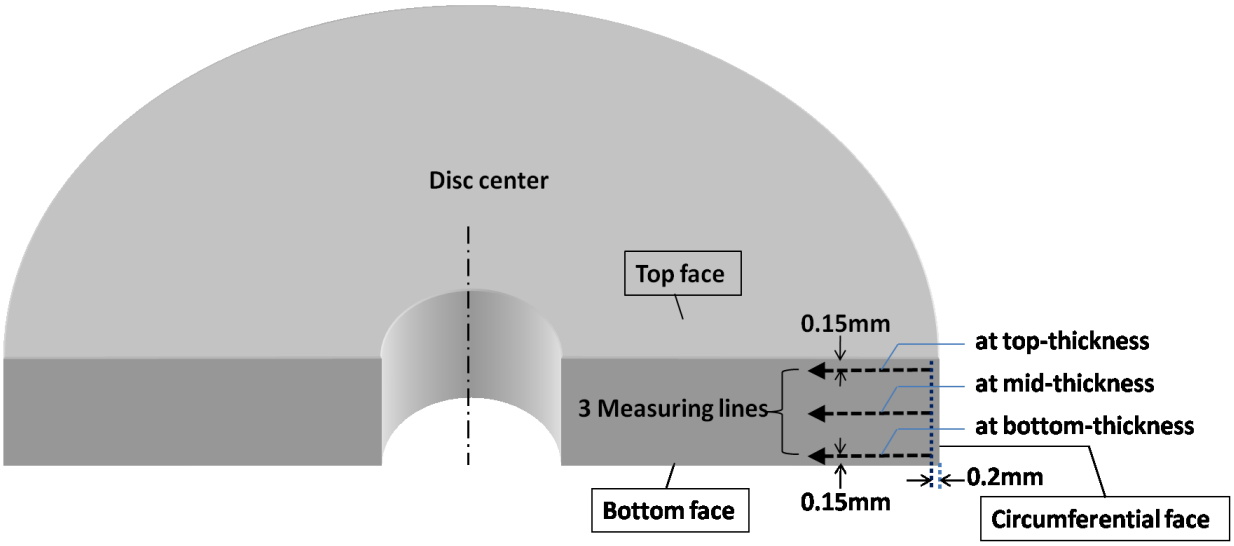

(a)

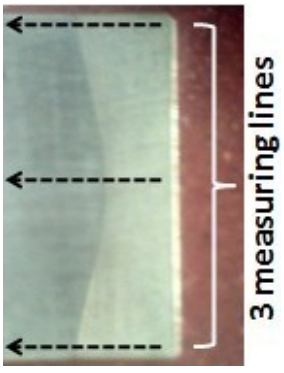

(b)

Fig 3.12: (a) schematic sketch of the micro-hardness measurement path at three different thickness positions of disc #7; (b) a photograph of the small cross-section used for real micro-hardness measurement of disc #7

CHAPTER 4

Results and Discussions

4.1 Hardening Depth Results

Nital quick-etching method was employed to give a rough estimation of the induction hardening depths of the processed samples.

4.1.1 Group I: samples with 43HRC initial hardness

Fig 4.1 (a) to (e) are the image views of discs #1 to #5 top and bottom surface edges after etching. The detailed IH recipes applied to samples in this group and their resulting hardening depths are summarized in Table 4.1. The overall hardening depth order for the considered five discs is as follow: disc #1 > disc #4 > disc #5 > disc #2 > disc #3.

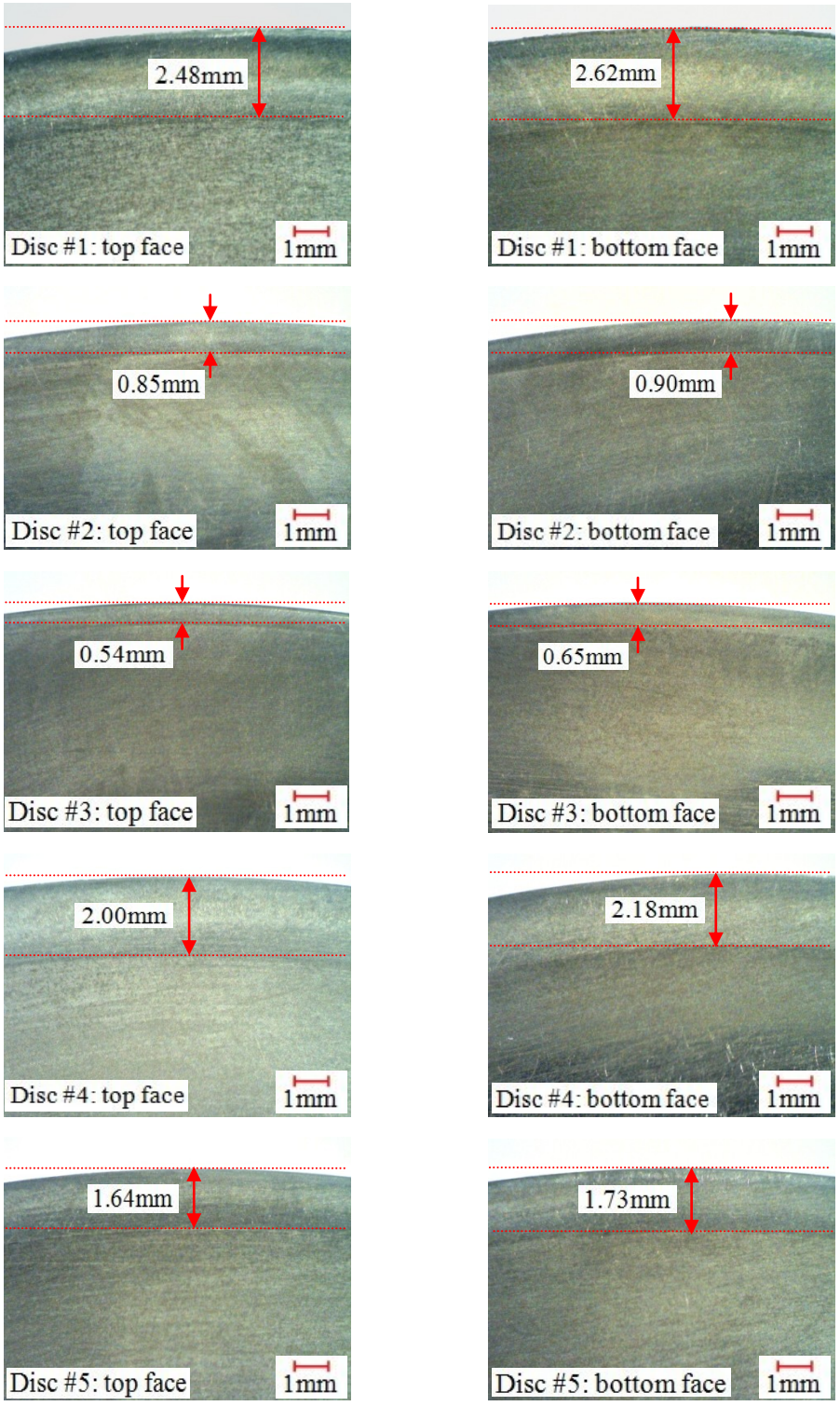

Fig 4.1 Optical images showing the hardening depths: the left hand side is for the top surface of discs #1 to #5; the right hand side is for the bottom surface of discs #1 to #5.

Table 4.1 Hardening depth result of group I

Samples	Initial Hardness (HRC)	IH Recipes (power and time)	Hardening Depth(mm) (Meas. error 1%-5%)		
			Top	Bottom	Average
Disc #1	43HRC	Power: 22% of maximum Heating time: 0.75s	~2.48	~2.62	~2.55
Disc #2		Power: 22% of maximum Heating time: 0.25s	~0.85	~0.90	~0.88
Disc #3		Power: 18% of maximum Heating time: 0.25s	~0.54	~0.65	~0.60
Disc #4		Power: 18% of maximum Heating time: 0.75s	~2.00	~2.18	~2.09
Disc #5		Power: 20% of maximum Heating time: 0.50s	~1.64	~1.73	~1.69

Moreover, it should be noted that all five discs in this group display a similar discrepancy in hardening depth between the top and bottom faces (see Fig 4.1 and Table 4.1). The hardening depth on bottom face is slightly larger than the top one for all cases. Although such discrepancy is relatively small and therefore the hardening depth on the top and bottom faces can be seen as similar, the possible reasons for this discrepancy are needed to be discussed. Firstly, this hardening depth difference probably suggests that the disc sample was not perfectly centered in the coil before performing the IH process – the disc may be positioned a little high which makes no more intense magnetic field at the bottom face. On the other hand, this fact may indicate a non-perfect-flat coil surface.

4.1.2 Group II: samples with 35HRC initial hardness

Similarly, Fig 4.2 (a) to (e) displays discs #11 to #15 top and bottom surface edges after etching. Again, the roughly estimated hardening depth on the top and bottom edges is quite close for every sample and the specifications are provided in Table 4.2.

The hardening depth comparisons are similarly carried out under the IH condition of a fixed heating time but various powers and a fixed power but various times. The results are consistent with the fact that higher energy result in higher case depth.

Also, the hardening depth discrepancy has been observed in this group. However, in contrast with group I, here all five discs demonstrate a larger hardening depth on the top rather than the bottom face. Therefore, in these cases, it suggests that the part may be positioned a little low in the induction coil. The reason of the inconsistent trend of the hardening depth discrepancy (of sample's top and bottom faces) between group I and II could be attributed to the coil resetting process for group II before the IH treatment. Since the induction coil was removed and fixed again, the sample's position in the coil must be changed more or less. As a result, the hardening depth on top and bottom faces altered.

Additionally, except disc #11, all samples demonstrate approximately the similar hardening depth (the discrepancy is relatively small) on the top and bottom faces. The relatively big hardening depth discrepancy of disc #11 could be also attributed to the positioning of the part in the induction coil. For example, if the part is positioned too high in the coil, similar discrepancy would be obtained.

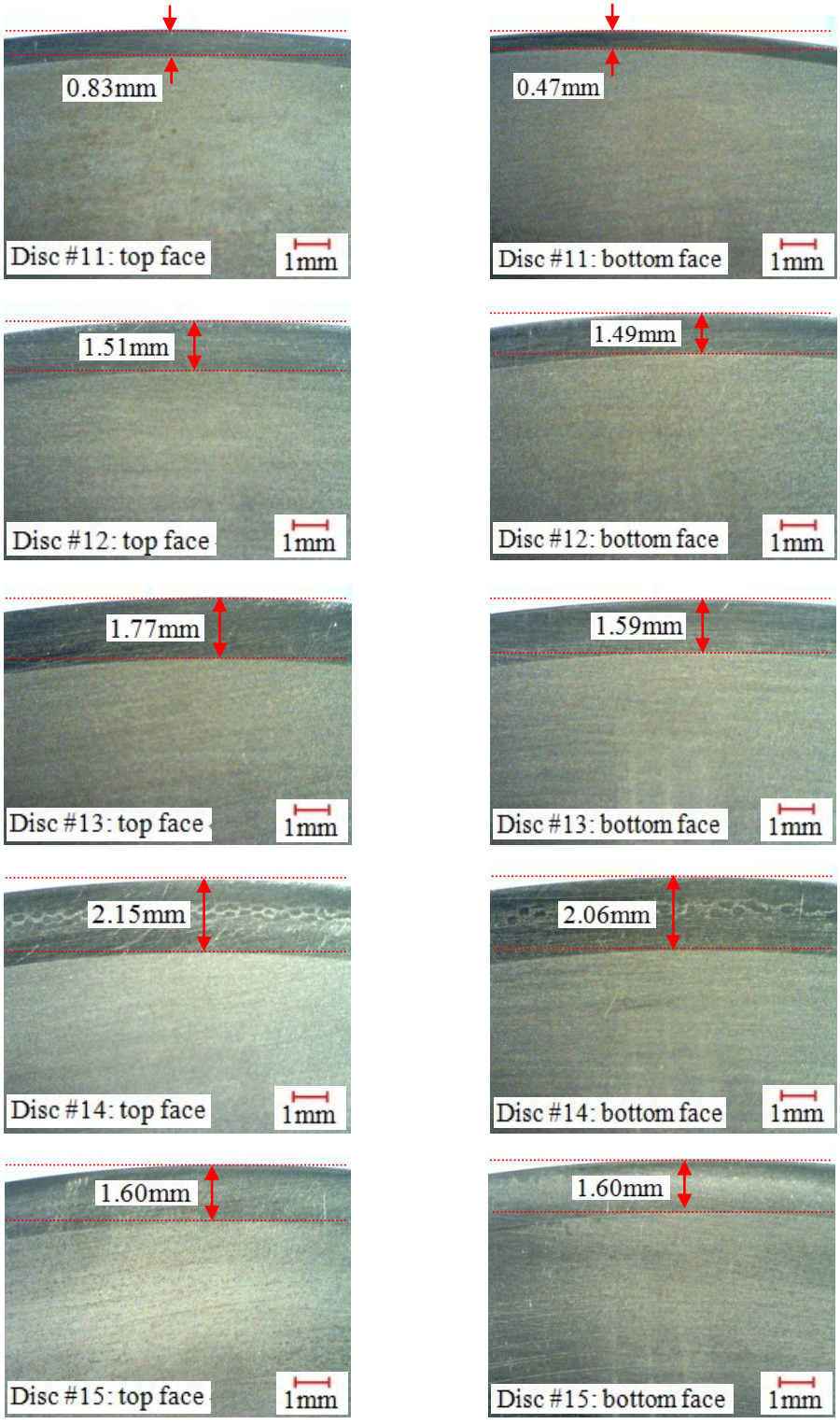

Fig 4.2: Optical images showing the hardening depths: the left hand side is for the top surface of discs #11 to #15; the right hand side is for the bottom surface of discs #11 to #15.

Table 4.2 Hardening depth result of group II

Samples	Initial Hardness (HRC)	IH Recipes (power and time)	Hardening Depth(mm) (Meas. error 1%-5%)		
			Top	Bottom	Average
Disc #11	35HRC	Power: 20% of maximum Heating time: 0.25s	~0.83	~0.47	~0.65
Disc #12		Power: 18% of maximum Heating time: 0.50s	~1.51	~1.49	~1.50
Disc #13		Power: 20% of maximum Heating time: 0.75s	~1.77	~1.59	~1.68
Disc #14		Power: 22% of maximum Heating time: 0.50s	~2.15	~2.06	~2.10
Disc #15		Power: 20% of maximum Heating time: 0.50s	~1.60	~1.60	~1.60

4.1.3 Group III: samples with 27HRC initial hardness

As mentioned earlier in the distortion result's section, this group is a comparison group with group I because the present five samples have undergone completely the same five induction hardening recipes employed on group I. Therefore the purpose of the hardened depth measurements here is to probe the influence of the initial hardness on induction hardening depth.

Fig 4.3 (a) to (e) demonstrates the hardening depths of discs #16 to #20 measured on top and bottom surfaces, and meanwhile Table 4.3 lists the related hardening depth results of these samples. Similarly, it has been found that the higher the energy input, the deeper is the case depth.

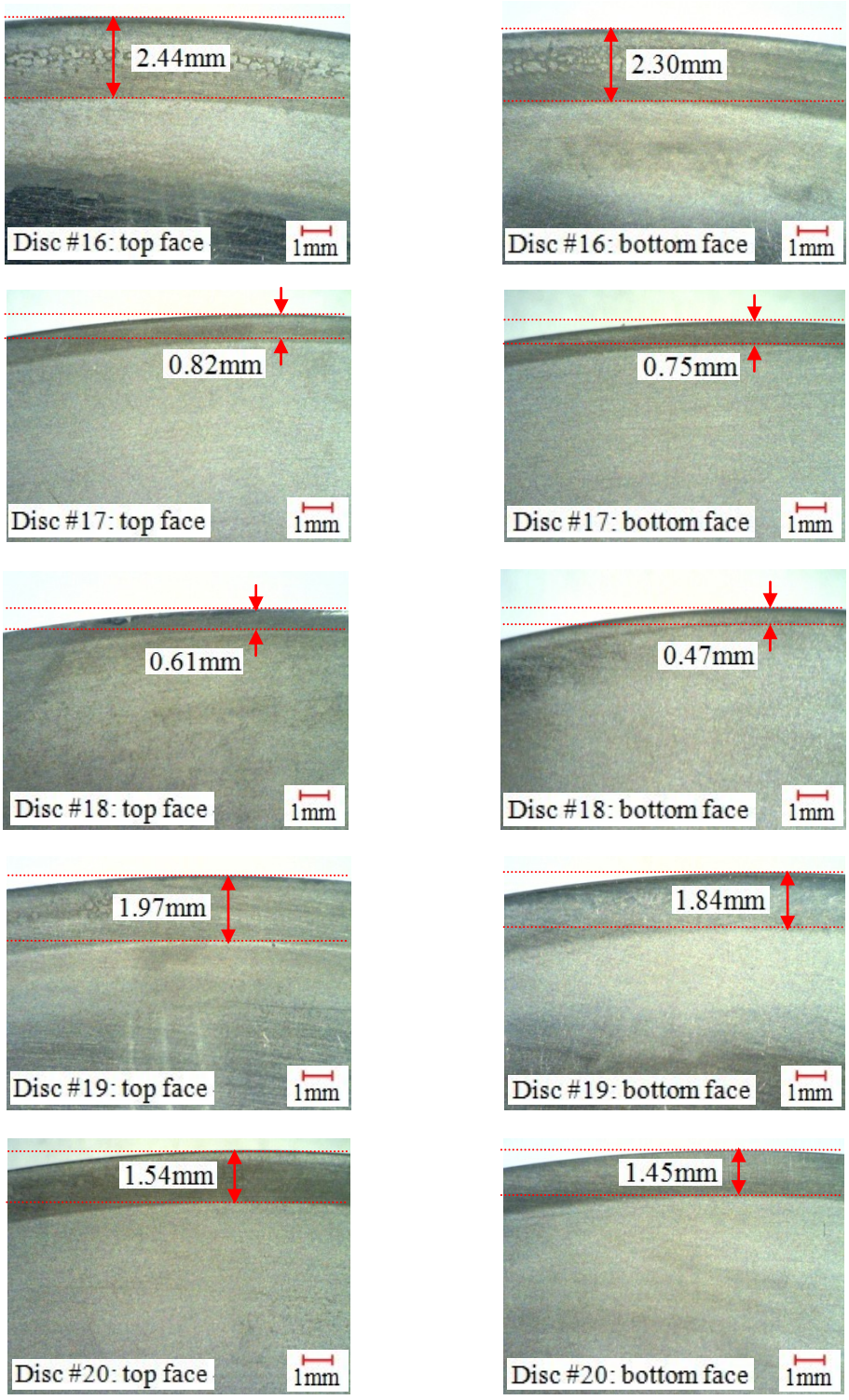

Fig 4.3: Optical images showing the hardening depths: the left hand side is for the top surface of discs #16 to #20; the right hand side is for the bottom surface of discs #16 to #20.

Table 4.3 Hardening depth result of group III

Samples	Initial Hardness (HRC)	IH Recipes (power and time)	Hardening Depth(mm) (Meas. Error 1%-5%)		
			Top	Bottom	Average
Disc #16	27HRC	Power: 22% of maximum Heating time: 0.75s	~2.44	~2.30	~2.37
Disc #17		Power: 22% of maximum Heating time: 0.25s	~0.82	~0.75	~0.79
Disc #18		Power: 18% of maximum Heating time: 0.25s	~0.61	~0.47	~0.54
Disc #19		Power: 18% of maximum Heating time: 0.75s	~1.97	~1.84	~1.91
Disc #20		Power: 20% of maximum Heating time: 0.50s	~1.54	~1.45	~1.50

Again, the hardening depth discrepancy between discs' top and bottom faces are observed in this group. This discrepancy trend is similar to that of group II, which the larger hardening depth was shown on the top face for all samples. The possible reasons for this are same as the previous two groups.

Furthermore, a set of hardening depth comparisons are carried out between the five discs of group I and those of group III, in order to learn the initial hardness effect on disc's hardening depth. Each comparison is made based on the two discs treated with the same IH recipe, from group I with initial hardness of 43HRC and group III with initial hardness of 27HRC, respectively. For easy explanation, such two discs are further defined as a "comparison pair" and the detailed IH specifications for such five comparison pairs have been summarized in Table 4.4. Moreover, Fig 4.4 shows the plotting of the hardening

depth as a function of the energy given to the part (power multiplied by time), for each comparison pair.

It is clear from both Table 4.4 and Fig 4.4 that every pair having initial hardness of 43HRC always shows a greater hardening depth than that with 27HRC initial hardness. This finding proves that the initial hardness indeed varies the induction hardening depth and the higher the initial hardness, the more the hardening depth, vice versa. A possible explanation for this evidence could be viewed from the point that in order to reach a same induction hardening depth, steel sample with lower initial hardness requires more heat input than that with higher initial hardness, because the lower initial hardness steel has a relative higher austenite transformation temperature. In addition, it can be observed from Fig 4.4, regardless of the initial hardness, the disc's hardening depth almost increases linearly with the increasing input energy. If comparing the slope of the hardening depth line between the 43HRC initial hardness based and the 27HRC one, the 43HRC line shows a slightly bigger slope. However, the reliable explanation for such cannot be given in present study because it requires more experimental tests related in the future works.

Table 4.4 Comparison pairs based on group I and III

Comparison Pairs	Samples	IH Recipes (power and time)	Initial Hardness (HRC)	Hardening Depth (Avg., mm) error 1%-5%
Pair 1	Disc #1	Power: 22% of maximum	43	~2.55
	Disc #16	Heating time: 0.75s	27	~2.37
Pair 2	Disc #2	Power: 22% of maximum	43	~0.88
	Disc #17	Heating time: 0.25s	27	~0.79
Pair 3	Disc #3	Power: 18% of maximum	43	~0.60
	Disc #18	Heating time: 0.25s	27	~0.54
Pair 4	Disc #4	Power: 18% of maximum	43	~2.09
	Disc #19	Heating time: 0.75s	27	~1.91
Pair 5	Disc #5	Power: 20% of maximum	43	~1.69
	Disc #20	Heating time: 0.50s	27	~1.50

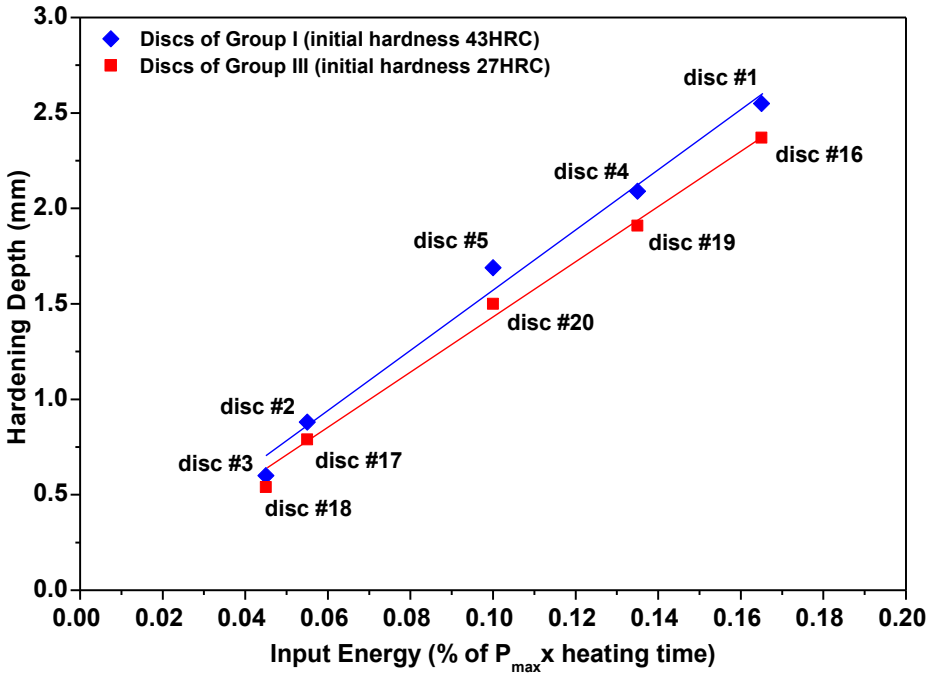

Fig 4.4 Hardening depth comparison between group I with initial hardness of 43HRC and group III with initial hardness of 27HRC

4.2 Distortion Results of the Three Hardness Groups

As documented in chapter III, the axial distortion (ΔZ) measurement of the disc was carried out by measuring the Z coordinate of each investigated point on top/bottom face before and after the IH treatment. The radial distortion (ΔR) measurement was performed by measuring the radius change of each investigated point on disc's lateral face due to the IH process.

Since 48 measuring angles were used to characterize the distortions around one disc, 48 axial distortion profiles (along disc's radius) and 48 radial distortion profiles (along disc's thickness) are available for analysis. However, based on Fig 4.5, it can be seen that although the trend of distortion profile at each angle is similar, the distortion's magnitude at the similar measuring position (same Z coordinate and same radial position) is varied with angles, more or less. Therefore, using the average of 48 distortion profiles to make distortion analysis is somewhat not reliable, because this averaging process could make the originally large or small distortion offset each other, showing a medium value finally. This undoubtedly causes mistakes.

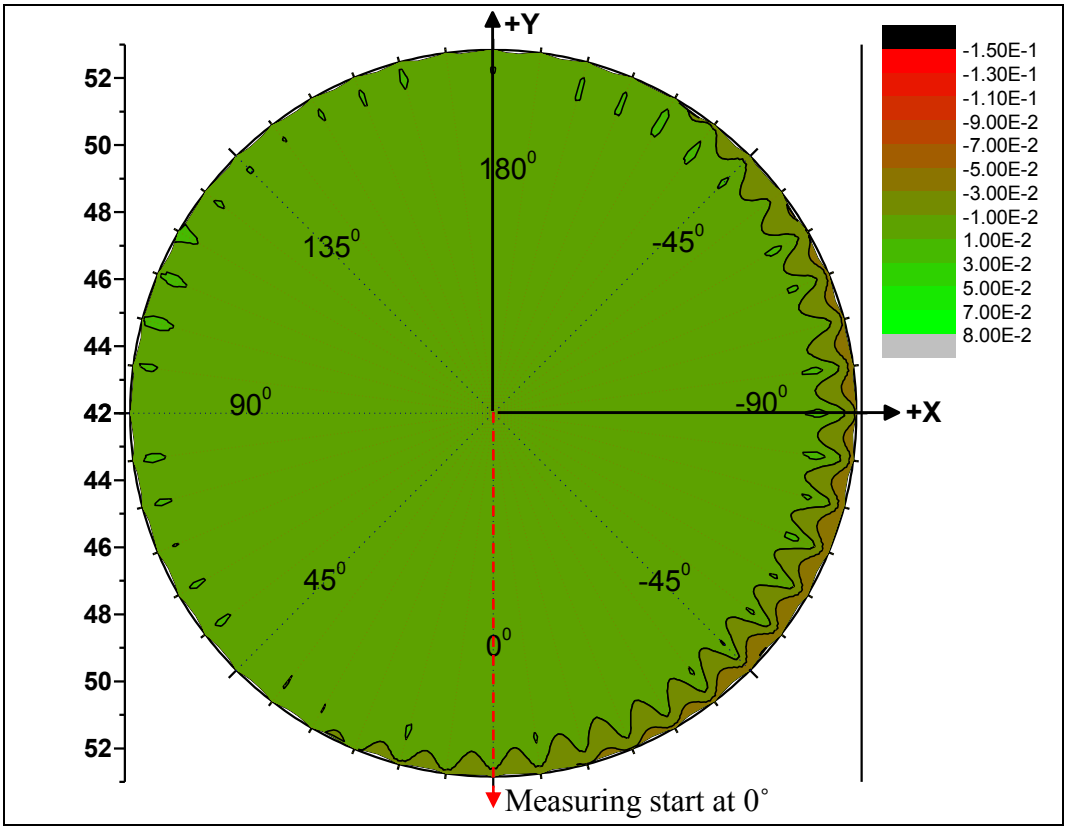

Fig 4.5 Axial distortion at top face of disc #1

Considering above, the distortion data obtained at four specific measuring angles, 0˚ (-Y-axis), 90˚ (-X-axis), 180˚ (+Y-axis) and -90˚ (+X-axis), were chosen to make distortion analysis for each disc, instead of averaging the distortion profiles at 48 angles. Even so, in this chapter, only the distortion data at measuring angle 0˚ are shown and discussed in details, as the representative for the axial and radial distortion analysis for each disc sample. This is taking into account that the measurement error caused by the equipment is assumed to be minimum at angle 0˚: since every distortion measurement was carried out starting from 0˚, the system error accumulation can be largely avoided at this degree. The distortion results at 90˚, -90˚ and -180˚ of all testing discs have been summarized in Appendix II, individually.

4.2.1 Group I-key group: discs with 43HRC initial hardness

4.2.1.1 Axial distortion

Figures 4.6(a) to 4.10(a) demonstrate the dimensional changes of disc samples #1 to #5 in axial direction with the averaged hardening depth (HD_{avg}) of top and bottom faces. The ΔZ profiles on the top and bottom surfaces are approximately symmetric for all disc samples. This means that the axial distortion patterns are almost the same on these two faces for every disc. Besides, although these five disc samples were heat treated by different set of induction hardening parameters, the general trend of axial distortion (ΔZ) profile is more or less similar. In the region that is relatively close to the disc center, the axial distortion (ΔZ) of all samples shows a value approaching zero for both top and bottom surfaces, indicating the fact that there is no distortion generated in this area. Then, with the increasing distance from center, the distortion profile is somewhat contraction particularly with respect to disc #2, #3 and #5. Afterwards, within a few millimeters close to the edge, a characteristic variation of axial distortion (ΔZ) takes place. The distortion profile always firstly goes up with increasing R, reaching a maximum and then followed by an obvious drop. This leads to a "convex" pattern of the axial distortion occurred near the edge of the disc (on both top and bottom surfaces), which points out a material's expansion happened within this region. Considering the axial distortion in the outmost layer of the disc, in other words, in the region most close to the disc edge, it presents a

case to case difference. For example, a big shrinkage in the outmost layer happens on disc #1, whose ΔZ on top/bottom surface reverses its sign and achieves -0.06mm/+0.03mm at the outermost point, as shown in Fig 4.6(a). However, disc #2 to #5 does not demonstrate such big shrinkage in the outermost layer. This could be seen from Fig 4.7(a) to 4.10(a), where these four discs' ΔZ profiles, unlike disc #1, do not show a big drop at the corresponding outermost point.

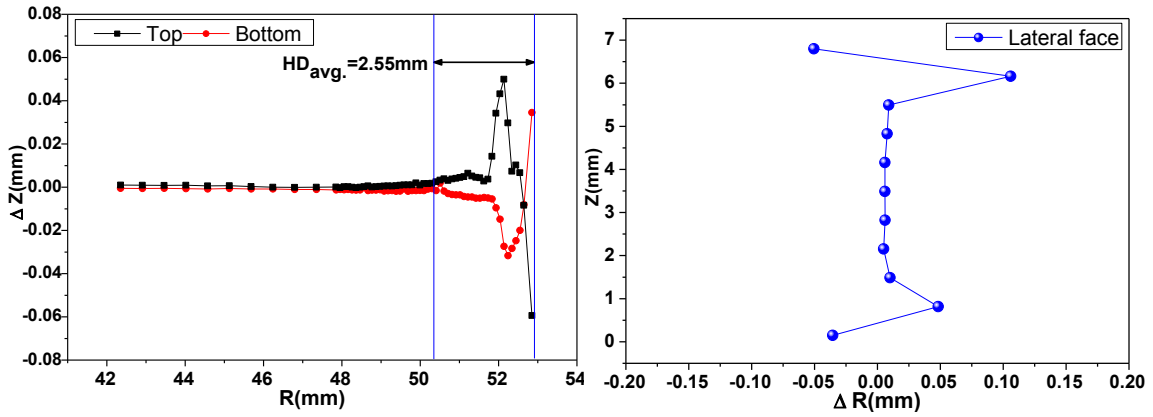

(a) (b)

Figure 4.6 IH distortions of disc #1: (a) axial distortion (ΔZ) on the top/bottom face along radius of the disc; (b) radial distortion (ΔR) on the lateral face along thickness of the disc.

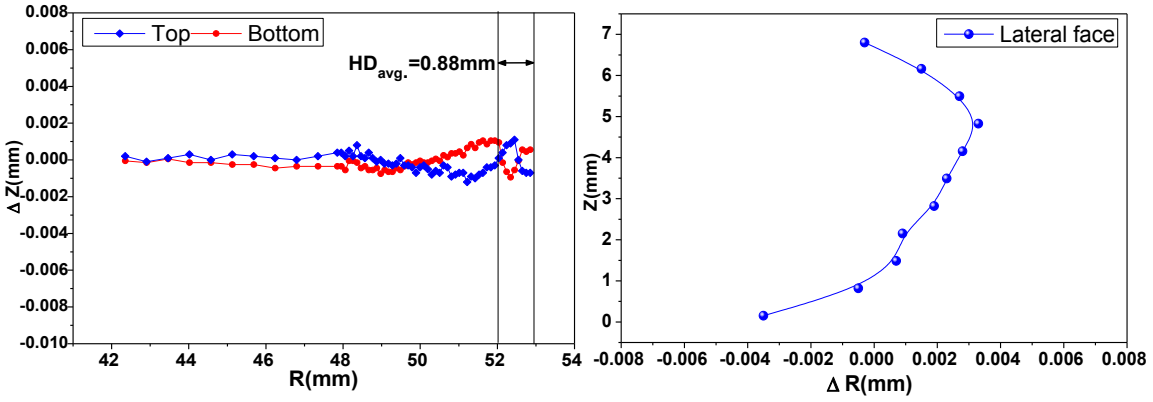

(a) (b)

Figure 4.7 IH distortions of disc #2: (a) axial distortion (ΔZ) on the top/bottom face along radius of the disc; (b) radial distortion (ΔR) on the lateral face along thickness of the disc.

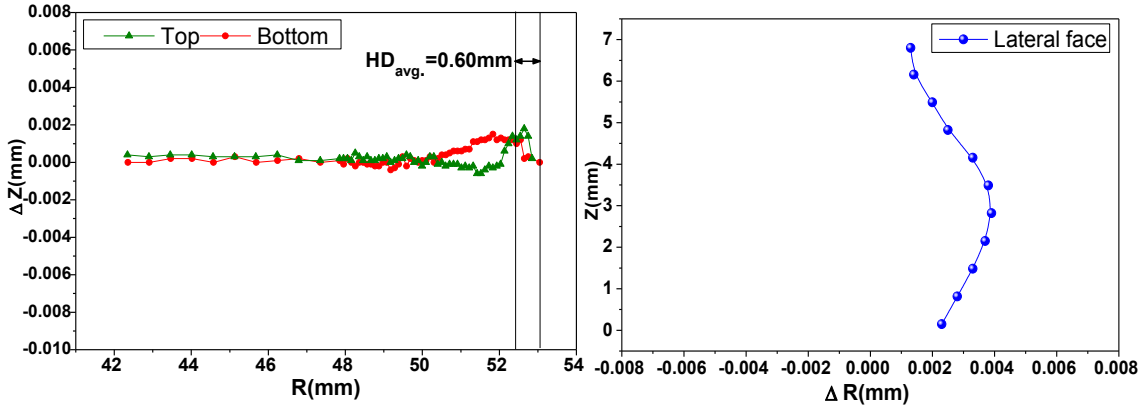

(a) (b)

Figure 4.8 IH distortions of disc #3: (a) axial distortion (ΔZ) on the top/bottom face along radius of the disc; (b) radial distortion (ΔR) on the lateral face along thickness of the disc.

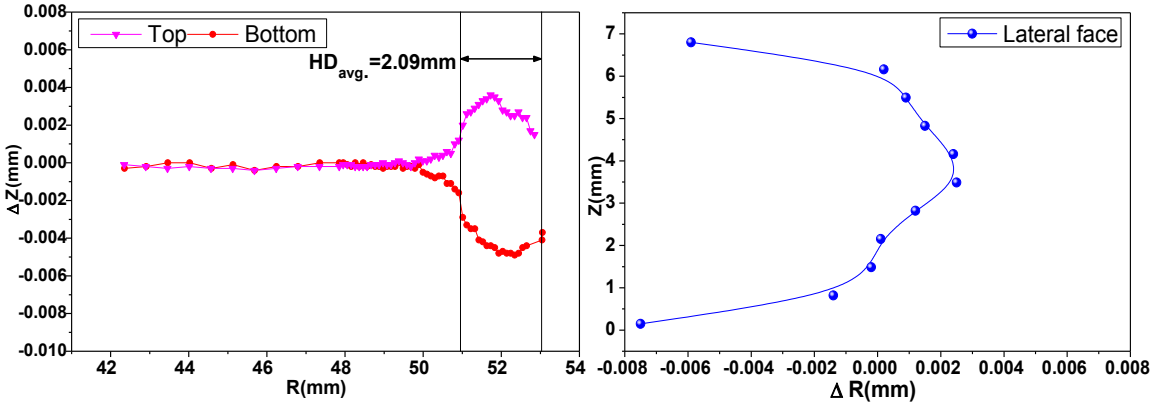

(a) (b)

Figure 4.9 IH distortions of disc #4: (a) axial distortion (ΔZ) on the top/bottom face along radius of the disc; (b) radial distortion (ΔR) on the lateral face along thickness of the disc.

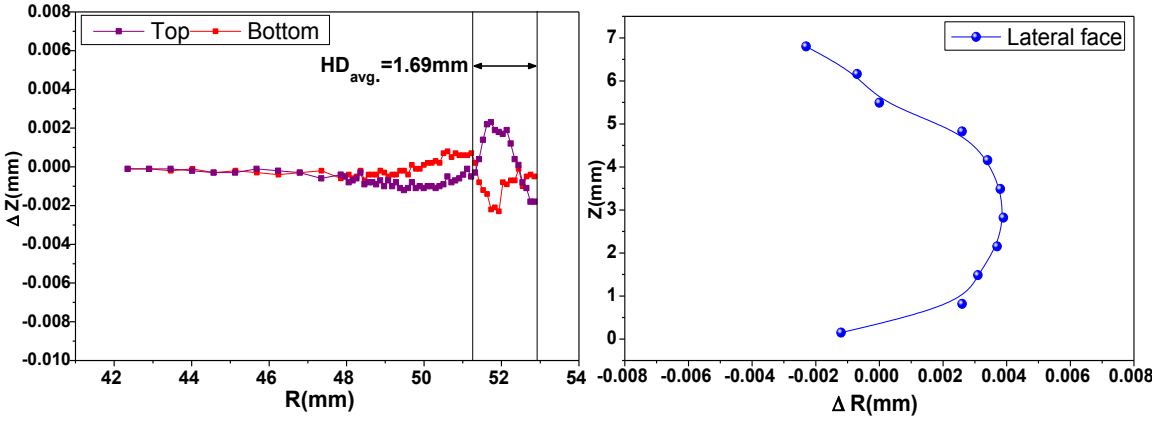

(a) (b)

Figure 4.10 IH distortions of disc #5: (a) axial distortion (ΔZ) on the top/bottom face along the radius; (b) radial distortion (ΔR) on the lateral face along thickness of the disc.

In addition to the distortion trend, a comparison of the size (maximum of absolute ΔZ) and range of axial distortions among these five disc samples is also of great interest, since it can reveal the effects of induction hardening parameters on distortion profiles. Disc #1 is excluded from this comparison because it has the largest distortion size of 0.05mm, which is more than 10 times larger than that of the other disc samples. This phenomenon could be attributed to the "strongest" induction hardening recipe (largest power with longest heating time) applied to disc #1. Considering other four discs, as illustrated in Fig 4.11, disc #4 presents a relatively larger axial distortion size of around 0.04mm with relatively broader extension of the "convex" pattern over approximately 3mm from the outer edge. Discs #2 and #5 display a relatively smaller axial distortion size and narrower "convex" pattern compared with disc #4. For disc #3, the axial distortion profile did not form a clear "convex" pattern, but instead, it formed a slight "concave" shape in the range which suggests a volume shrinkage. This appearance is most likely attributed to the "weakest" induction hardening recipe (smallest power with shortest heating time) applied to disc #3. A slightly larger distortion size of disc #2 than disc #3 is observed, owing to the same heating time as disc #3 but with larger heating power. As for disc #5, this disc was induction hardened by a medium heating power and time, demonstrating a moderate axial distortion size and "convex" pattern. In summary, the axial distortion size (maximum of absolute ΔZ) sequence yields: disc #1 > disc #4 > disc #5 > disc #2 ≥ disc #3. It is not surprising to note that disc #1 has the largest while disc #3 has the smallest

distortion size, since they encountered the "strongest" and "weakest" induction hardening recipes, respectively, as mentioned above. Both the larger heating power and the longer heating time can enhance the distortion magnitude.

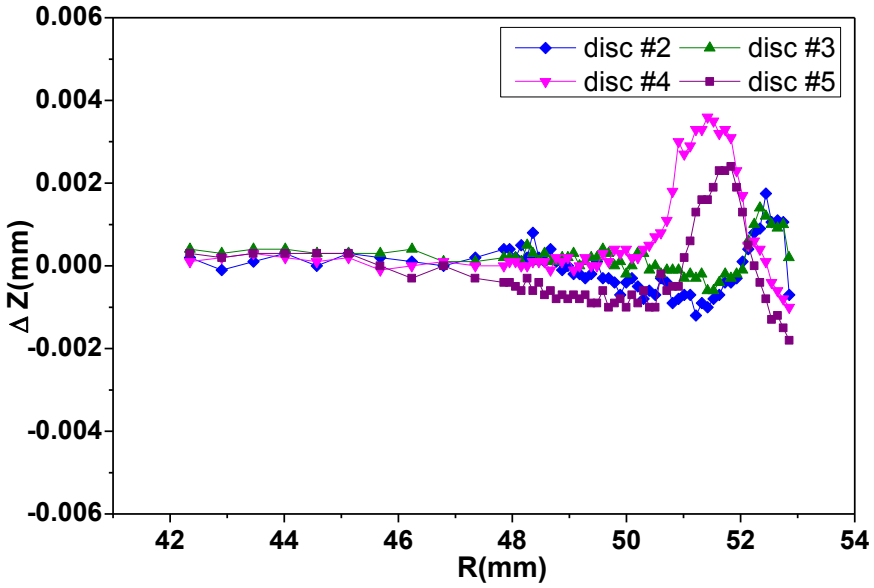

Figure 4.11 Comparison of the axial distortions on top surface among disc sample #2, #3, #4 and #5 due to different induction hardening recipes

Table 4.5 Axial distortion results of discs from group I

Samples	**Initial Hardness (HRC)**	**IH Recipes (power and time)**	**Max. Axial Distortion (mm)**	
			Top face	**Bottom face**
Disc #1	43HRC	Power: 22% of maximum Heating time: 0.75s	~0.050	~0.035
Disc #2		Power: 22% of maximum Heating time: 0.25s	0.001-0.002	0.001-0.002
Disc #3		Power: 18% of maximum Heating time: 0.25s	~0.001	~0.001
Disc #4		Power: 18% of maximum Heating time: 0.75s	~0.004	~0.005
Disc #5		Power: 20% of maximum Heating time: 0.50s	~0.003	~0.004

4.2.1.2 Radial distortion

Figures 4.6(b) to 4.10(b) depict the radial distortion (ΔR) profiles of discs #1 to #5 on the lateral face along the disc thickness Z. The origin point is set at the bottom surface of the disc, therefore Z=0mm and Z=7mm (approximately) represents the bottom surface and the top surface, respectively. It can be noted that disc #1 is still a special case among all samples, since it has a distinctly large radial distortion size with ΔR in the range from approximately -0.06mm to 0.10 mm, and displays a relatively different radial distortion profile, as shown in Fig 4.6(b). The biggest radial shrinkage of disc #1, which is ΔR=-0.06mm, is observed at the upmost part (the part that most closely to the top surface). This shrinkage rapidly changes into expansion, achieving a maximum ΔR=0.10mm at Z=5.5mm approximately. This radial expansion diminishes and a noticeable protuberance pattern is formed finally at the upper part of the lateral face. Besides, another similar protuberance pattern, but with a smaller size, is found at the lower part (the part that is close to the bottom surface) of the lateral face of disc #1.

Concerning the middle part of the lateral face of disc #1, the radial distortion in this region is not significant because of the ΔR with a value approximately approaching zero. This overall radial distortion profile of disc #1, with the two protuberances at the upper and lower part of the lateral face is somewhat reasonable. It can be supported by the corresponding axial distortion profiles of the top/bottom surface of the same disc, as illustrated in an exaggerated drawing in Fig 4.12.

Owing to the “strongest” induction hardening recipe, disc #1 demonstrates the largest distortion size and unique profiles in both axial and radial directions. Relating its axial distortion profiles on top/bottom surface to its radial distortion profile on lateral face, it can be seen that: (1) the axial shrinkage in the outermost layer of the top surface is accompanied with the radial shrinkage at the upper part of the lateral face. This fact could be seen as a kind of “corner shrinkage”; (2) considering the occurrence of shrinkage and the entire disc volume should be almost constant (assuming the Martensite transformation in the outside layer of the disc does not contribute significant volume expansion. This usually is around 0.4-0.5% of the overall volume [76]), the corresponding expansion appeared at the area adjacent to where the shrinkage occurred. (3) The protuberance pattern at the lower part of lateral face is relatively smaller than the upper one, which can be connected to the smaller size convex pattern of the bottom surface.

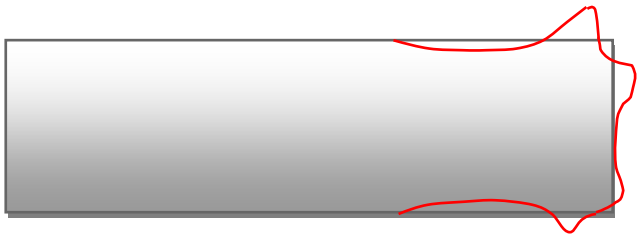

Figure 4.12 Schematic drawing of an exaggerated distortion contour based on disc #1 due to induction surface hardening.

Regarding the other four discs, as shown in Fig 4.7(b) to 4.10(b), all radial distortion profiles demonstrate a more or less convex pattern over the whole disc thickness (Z) usually with a maximum radius nearby the mid-thickness (the middle part of lateral face) of the disc and minimum radius at the upper or lower part of lateral face (Z around

7.0mm or 0.0mm respectively). In terms of each disc, similarly as the analysis of disc #1, the specific radial distortion shape could be largely related to the corresponding axial distortion profile of each one. For example, discs #2, #4 and #5 (Fig 4.7(b), 4.9(b) and 4.10(b)) all display a negative ΔR in the region of Z close to 7.0mm and 0.0mm. This indicates the occurrence of shrinkage at both the upper part and lower part of the lateral face, and the magnitude of this shrinkage could be linked to the size of the convex pattern presented on the corresponding axial distortion profile. Based on the comparison of disc axial distortion in Fig 4.11, the larger convex pattern of the axial distortion of disc #4 gives rise to a corresponding larger radial shrinkage at upper and lower part of the lateral face (Fig 4.9(b)). However, the smaller convex pattern of the axial distortion leads to a relatively smaller radial shrinkage similar to disc #2 (Fig 4.7(b)). This finding, to some degree, could probably be understood by the larger expansion (the convex pattern) on disc top/bottom surface contributing to the greater radial shrinkage at the two "adjacent area" (the upper and bottom parts) of the disc lateral face. This has been further confirmed by disc #3. The ΔR value of disc #3 is positive over the whole thickness with the maximum at the near mid-thickness position, which means a smaller radial expansion not shrinkage happens at the adjacent areas (of the lateral face). This could be also connected to the slight concave shape rather than the convex pattern of the axial distortion profile shown at the relevant top/bottom surface edge. Consequently, the most likely distortion contour after induction hardening heat treatment is illustrated as Fig 4.13,

based on discs #2 to #5. It's interesting to see when approaching to the edge of top and bottom surface, the expansion contour changes to shrinkage. As for the lateral surface, the distortion contour presents expansion in the middle and turns to shrink when close to the top and bottom surfaces.

Figure 4.13 Schematic drawing of an exaggerated distortion contour based on discs #2 to #5 due to induction surface hardening.

4.2.1.3 Relationship between IH input energy and the resulting distortion

It has been found that the distortions of induction hardened discs vary with the IH recipes applied, that is, the input energy (power and heating time). In order to see how distortions change with IH recipes, Fig 4.14 gives the distortions as a function of input energy based on samples in group I.

It is clear from Fig 4.14 that the distortion increases with the input energy. Disc #1 was induction hardened with the most input energy and therefore it demonstrates the largest distortion size. However, it is interesting to see that the distortion curve has a big jump from no more than 0.01mm (disc #2, #3, #4 and #5) up to around 0.05 mm (disc #1). This remarkable increase in distortion of disc #1 can also be seen from the corresponding distortion profiles in Fig 4.6. The reason for this could because of the energy put into disc

#1 has reached the maximal limitation. In the processing of IH heating step, few sparkles were observed, which probably indicates the disc #1 was slightly melted. Fig 4.15 shows the appearance of the lateral face of disc #1 after IH. It can be seen that a very obvious deformation occurred on the lateral face and such deformation is not uniform around the disc.

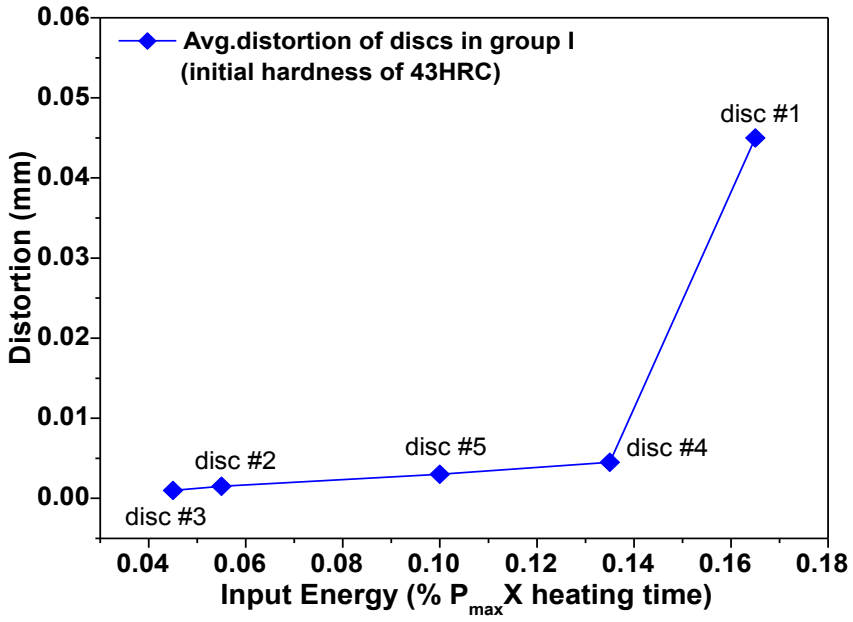

Fig 4.14 Distortions as a function of input energy for discs in group I

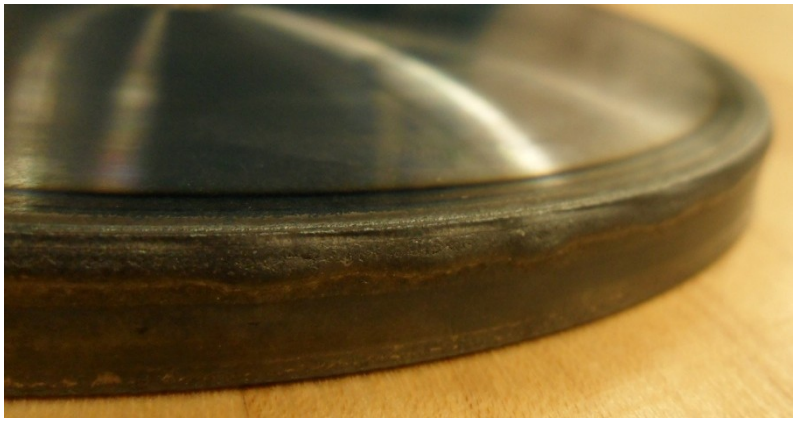

Fig 4.15 Remarkable distortion on disc #1 lateral face due to the most input IH Energy

In summary, based on the distortion and hardening depth investigations of group I, it can be obtained: the stronger IH recipe, which actually means more heat input into the sample, the deeper is the heat penetration giving rise to a larger distortion size as well as hardening depth.

4.2.2 Group II: discs with 35HRC initial hardness

Disc samples (discs #11 to #15) in this group, with a medium initial hardness of 35HRC were induction hardened by selective recipes to further document the influence of time and power applied during the induction hardening on the resulting distortion size and range.

Similar to group I, all distortion results shown here are the distortions measured at 0˚ (-Y-axis). The distortion results at 90˚, -90˚ and -180˚ measuring angles have been also summarized in Appendix II, individually.

Fig 4.16 shows the differences in the axial distortion and hardening depth (HD_{avg}) among discs #12, #15 and #14 resulting from the different induction hardening recipes. These three discs, as given in Table 4.4, were induction hardened for the same duration 0.50s but with different powers which were 18%, 20% and 22% of maximum power, respectively. The resulting distortion profiles reveal that both the distortion size and range follow a sequence: disc #12 < disc #15 < disc #14, which further confirms that increasing the induction power increases the distortions.

Likewise, Fig 4.17 compares the axial distortion and hardening depth (HD_{avg}) among discs #11, #15 and #13. These three discs, as given in Table 4.6, were induction hardened using the same power, 20% of maximum power, but different heating times which were 0.25s, 0.50s and 0.75s, respectively. The resulting distortion profiles uncover that both the distortion size and range yield a sequence: disc #11 < disc #15 < disc #13. This further supports that increasing the time causes more distortions. More detailed information for each disc in group II and the corresponding distortion results are provided in Table 4.6.

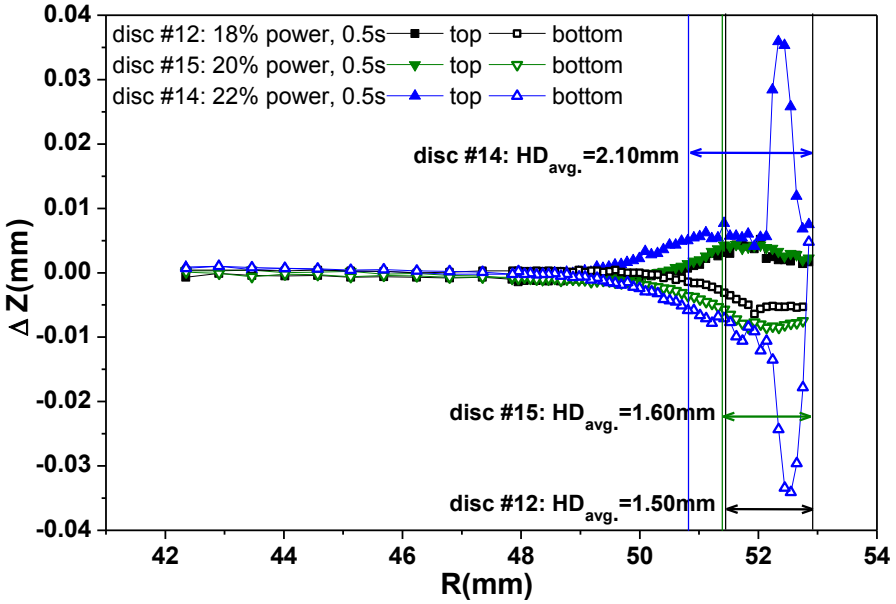

Fig 4.16: Comparison of the axial distortion profiles of the top/bottom surface among discs #12, #15 and #14

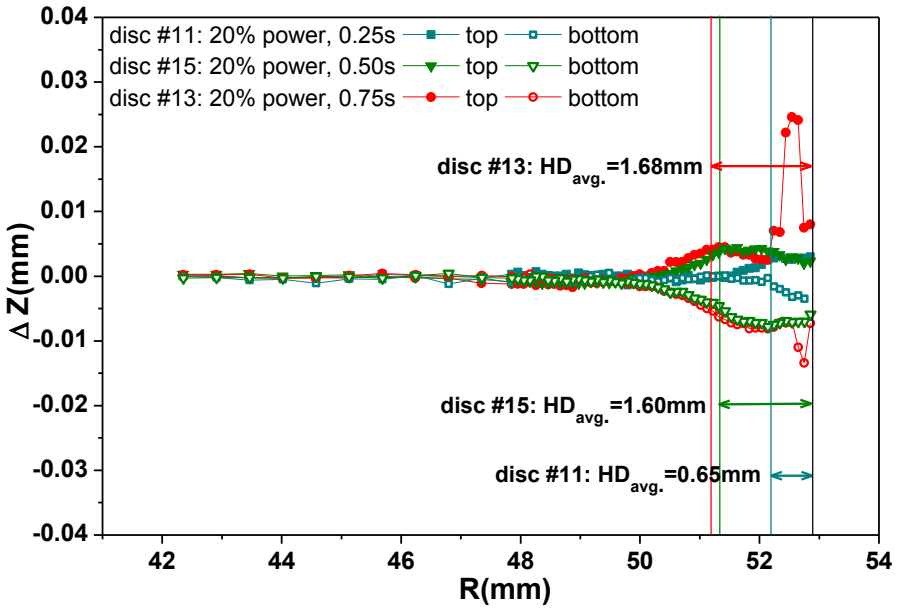

Fig 4.17: Comparison of the axial distortion profiles of the top/bottom surface among discs #11, #15 and #13

Table 4.6 Axial distortion results of discs from group II

Samples	Initial Hardness (HRC)	IH Recipes (power and time)	Max. Axial Distortion (mm)	
			Top face	Bottom face
Disc #11	35HRC	Power: 20% of maximum Heating time: 0.25s	0.003-0.004	0.003-0.004
Disc #12		Power: 18% of maximum Heating time: 0.50s	~0.005	~0.005
Disc #13		Power: 20% of maximum Heating time: 0.75s	~0.025	~0.015
Disc #14		Power: 22% of maximum Heating time: 0.50s	~0.035	~0.035
Disc #15		Power: 20% of maximum Heating time: 0.50s	~0.006	~0.008

Similarly, Fig 4.18 provides the distortions as a function of input energy in terms of samples in group II. As can be seen, in this test matrix again, the higher the energy input, the larger the distortion. The difference in the curve shape between Fig 4.17 and 4.18 is because of the different IH recipe applied.

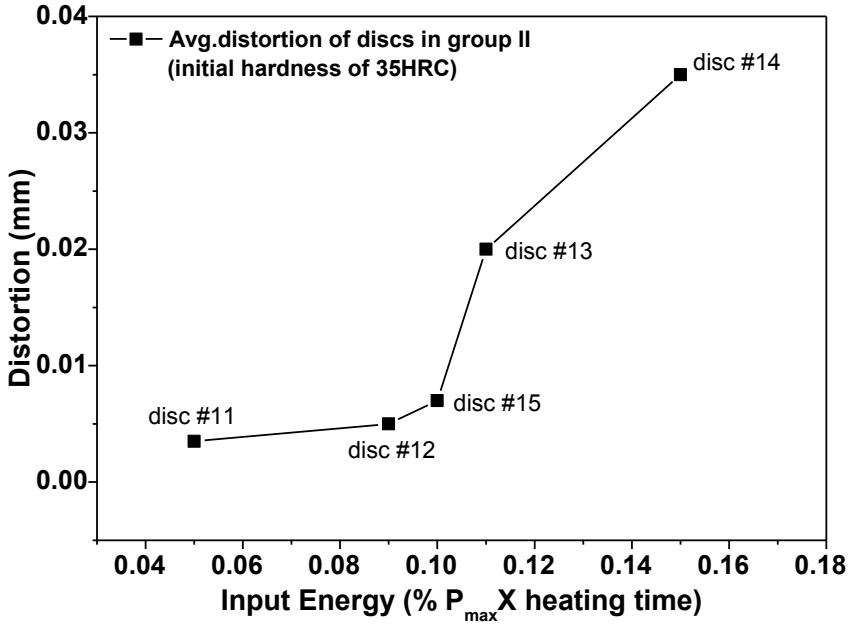

Fig 4.18 Distortions as a function of input energy for discs in group II

4.2.3 Group III-comparison group: discs with 27HRC initial hardness

Disc samples in this group encountered the same induction hardening recipes as that of group I but with a much lower initial hardness 27HRC, in order to see the initial hardness effects on distortion profiles.

Similarly, the distortion results shown here are those measured at 0˚. The axial and radial distortion results for this group at 90˚, - 90˚ and -180˚ are summarized in Appendix II.

Figures 4.19 (a) to (e) provide a series of comparisons of axial distortions and hardening depth (HD_{avg}) between disc samples in group I and group III in order to reveal the effect of initial hardness on distortions. The detailed information and corresponding distortion results for each comparison pair are given in Table 4.7

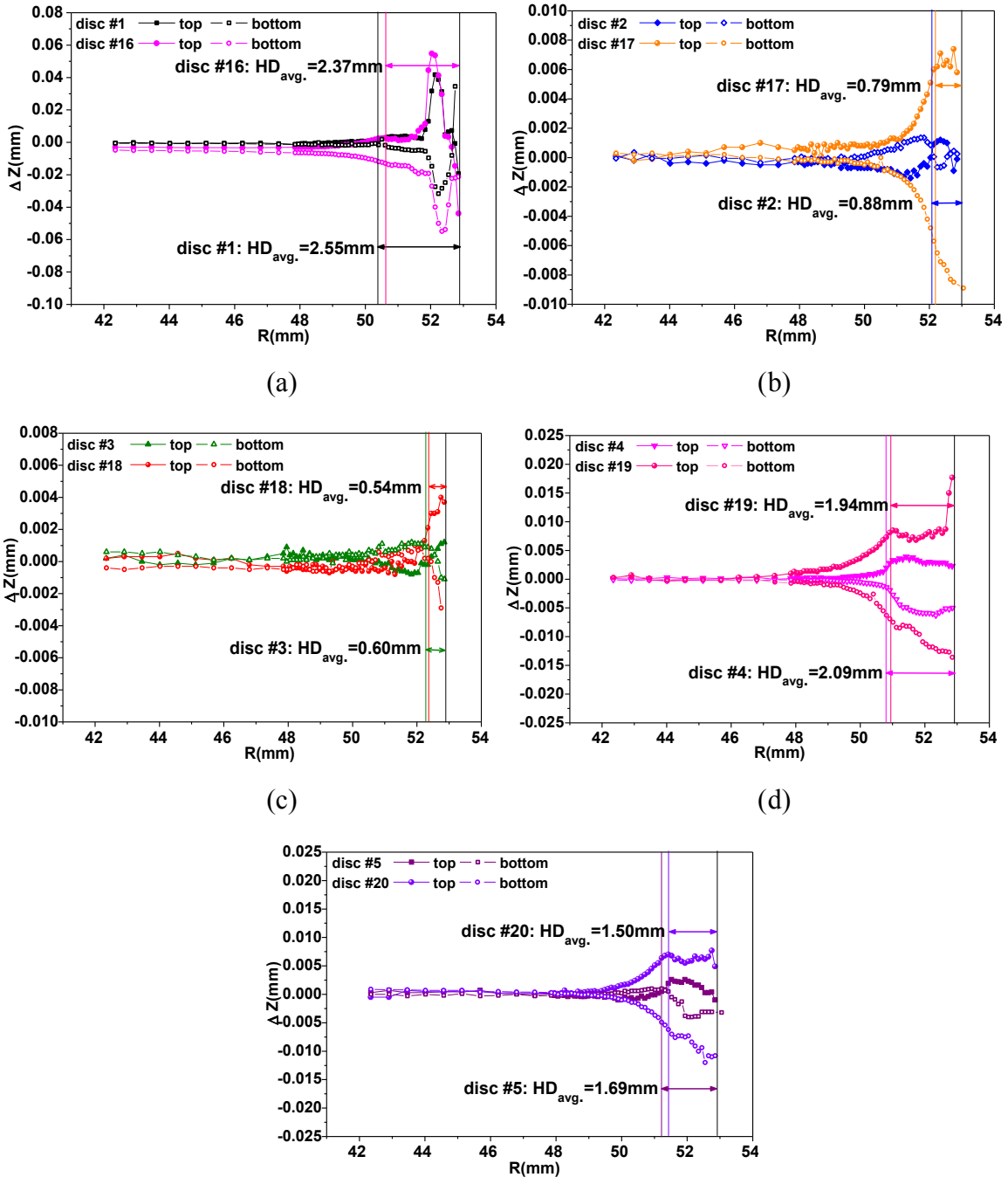

Figure 4.19 Comparisons of the axial distortions on the top/bottom face between samples from group I and group III: (a) pair 1: disc #1 and disc #16; (b) pair 2: disc #2 and disc #17; (c) pair 3: disc #3 and disc #18; (d) pair 4: disc #4 and disc #19; (e) pair 5: disc #5 and disc #20

Table 4.7 Comparison of distortion results between discs from group I and III

Pairs	Samples	Initial Hardness (HRC)	IH Recipes (time and power)	Max. Axial Distortion (mm)	
				Top face	Bottom face
Pair 1	Disc #1	43	Power: 22% of maximum	~0.050	~0.035
	Disc #16	27	Heating time: 0.75s	~0.055	~0.055
Pair 2	Disc #2	43	Power: 22% of maximum	0.001-0.002	0.001-0.002
	Disc #17	27	Heating time: 0.25s	0.007-0.008	0.008-0.009
Pair 3	Disc #3	43	Power: 18% of maximum	~0.001	~0.001
	Disc #18	27	Heating time: 0.25s	~0.004	~0.003
Pair 4	Disc #4	43	Power: 18% of maximum	~0.004	~0.005
	Disc #19	27	Heating time: 0.75s	~0.017	~0.014
Pair 5	Disc #5	43	Power: 20% of maximum	~0.003	~0.004
	Disc #20	27	Heating time: 0.50s	~0.008	~0.011

It is found that for each comparison pair, the disc with lower initial hardness (27HRC) always shows a larger distortion size and broader distortion range compared with the disc in the same pair but with higher initial hardness (35HRC). This fact suggests that the sample initial hardness can significantly affect the resulting distortion size and range. Lower initial hardness results in more distortions. This is due to the fact that material with lower hardness is undergoing plastic deformation more easily during the induction heat treatment process.

The variation of initial hardness can alter both distortion and hardening depth; reducing initial hardness results in a larger distortion but a smaller hardening depth. This is a paradox as it was found earlier that the deepest is the case depth, the largest is the distortion. The effect of the initial hardness on distortions seems to be complex and will be discussed later.

Fig 4.20 displays a comparison of distortion-input energy curve between group I and III. As shown, group III have the similar curve trend to that of group I except the overall distortion size is relatively larger. Therefore, it can be obtained that, under the same IH treatment, the sample with lower initial hardness can demonstrate more distortion than the higher one. This observation is opposite to the hardening depth comparison between these two groups, where the disc with 27HRC initial hardness has the relatively smaller hardening depth.

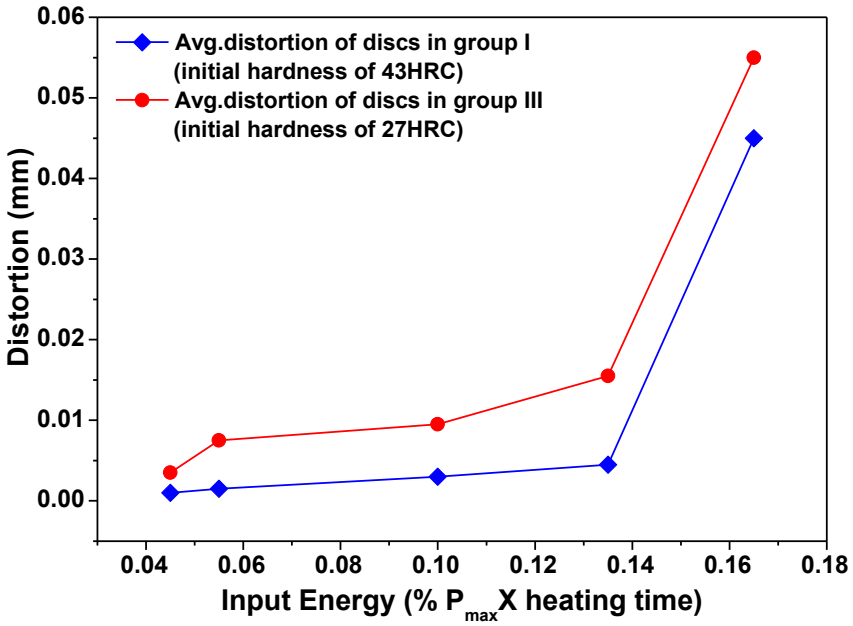

Fig 4.20 Comparison between group I and III: distortions as a function of input energy

4.2.4 Initial hardness effects on IH distortions and hardening depths

Three disc samples, disc #5 (initial hardness 43HRC), disc #15 (initial hardness 35HRC) and disc #20 (initial hardness 27HRC) are selected from group I, II and III, separately,

based on an identical induction hardening recipe 20% of maximum power and 0.50s heating time, aiming to further validate the impact of the sample's initial hardness on the resulting distortion size and range as well as the hardening depth.

4.2.4.1 Distortion and hardening depth (HD_{avg}) comparisons among disc #5, disc #15 and disc #20

Fig 4.21 shows the axial distortion profiles on both top and bottom surfaces of disc #5, #15 and #20. It is not surprising to note that these three axial distortion patterns are quite similar, but the distinct difference of their size and range is of great interest. Among them, disc #5 displays relatively large axial distortion magnitude and range, followed by disc #15 and then disc #20. This sequence is in accord with the ordering of sample initial hardness and therefore further confirms that the lower initial hardness can definitely assist to enlarge the relevant axial distortion size and range caused by induction surface hardening.

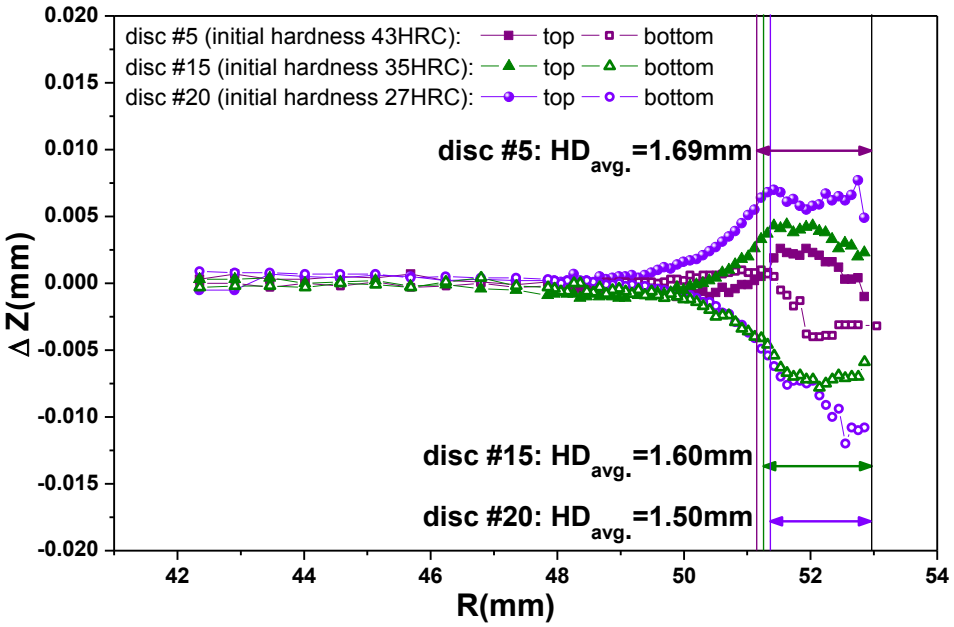

Fig 4.21: Comparison of the axial distortion profiles of the top/bottom surface among discs #5, #15 and #20 based on an identical induction hardening recipe

Fig 4.22 illustrates the radial distortion profiles on lateral face of discs #5, #15 and #20. It is relevant to notice that the radial distortion gradually changes from major expansion into total contraction with increasing the initial hardness. This could be seen that because of the lower initial hardness, the relevant convex pattern of axial distortion profile on top/bottom surface becomes larger. Since the convex pattern indicates a material expansion and in order to offset this increasing expansion, more shrinkage appears on the corresponding lateral face. Besides, it can be found that, for the radial distortion of disc #5, a regular convex pattern appears at the middle of the lateral face. However, for disc #20, a concave pattern is observed in the middle, accompanying with two symmetric protuberances at two sides of this concave pattern. Whereas disc #15, the disc with an intermediate initial hardness, displays profile somewhat in between the discs #5 and #20.

Therefore, it can be expected that with the decrease of initial hardness, the radial distortion of disc attempts to translate from general expansion to complete contraction. Meanwhile, the profile of radial distortion intends to change from the regular convex (in the middle of lateral face) into the irregular shape with two protuberances at two sides.

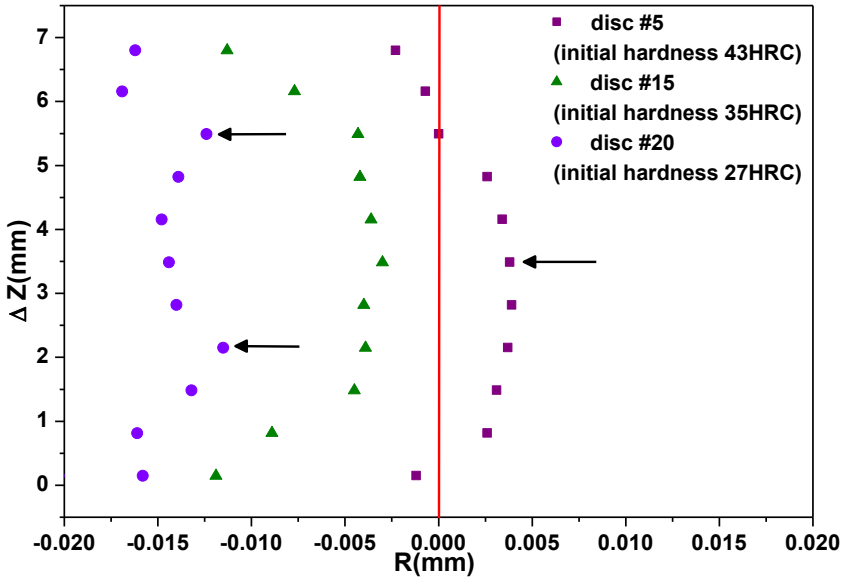

Fig 4.22: Comparison of the radial distortion profiles of the lateral face among discs #5, #15 and #20 based on the identical induction hardening recipe

Nevertheless, the clear explanation for such appearance of lateral distortion profiles of disc #15, #20 and even #5 is still not completely understood, especially for those two protuberances occurred in disc #20 radial distortion profile. One possible reason for this irregular but symmetric pattern could be viewed from the point that the induction surface hardening process can result in a slightly deeper hardened depth at the disc corner than the middle position (of disc thickness) due to the current concentration effect.

4.2.4.2 Distortion and hardening depth variation with initial hardness

The relevant distortion and hardening depth of disc #5, #15 and #20 are summarized in Table 4.8. Fig 4.23 illustrates the hardening depth (avg. of top and bottom) as well as the distortion in axial (avg. of max. top and bottom) and in radial (at mid-thickness) directions versus initial hardness under same induction hardening conditions for three discs. As shown in Fig 4.23(a), the averaged hardening depth of disc #5 is greater than that of disc #15 followed by disc #20. This is just contrary to the axial distortion size ordering of the same discs, as indicated by the first graph in Fig 4.23(b). This evidence, undoubtedly, again confirms that the increase of sample initial hardness contributes to a larger hardened depth while causing smaller axial distortions. Moreover, if comparing the two graphs in Fig 4.23(b), it can be found that the increasing of axial distortion is accompanied with the radius reduction from expansion to shrinkage.

Table 4.8 Distortion and hardening depth result of disc #5, #15 and #20

Disc #	**#5**	**#15**	**#20**
Initial hardness (HRC)	43	35	27
IH recipe	Power: 20% of maximum; Heating time: 0.50s		
Max. axial distortion (mm) (avg. of top and bottom)	~0.0035	~0.007	~0.0095
Radial distortion (mm) (at mid-thickness)	~0.004 (expansion)	~(-0.003) (contraction)	~(-0.014) (contraction)
Hardening depth (mm) (avg. of top and bottom)	1.69	1.60	1.50

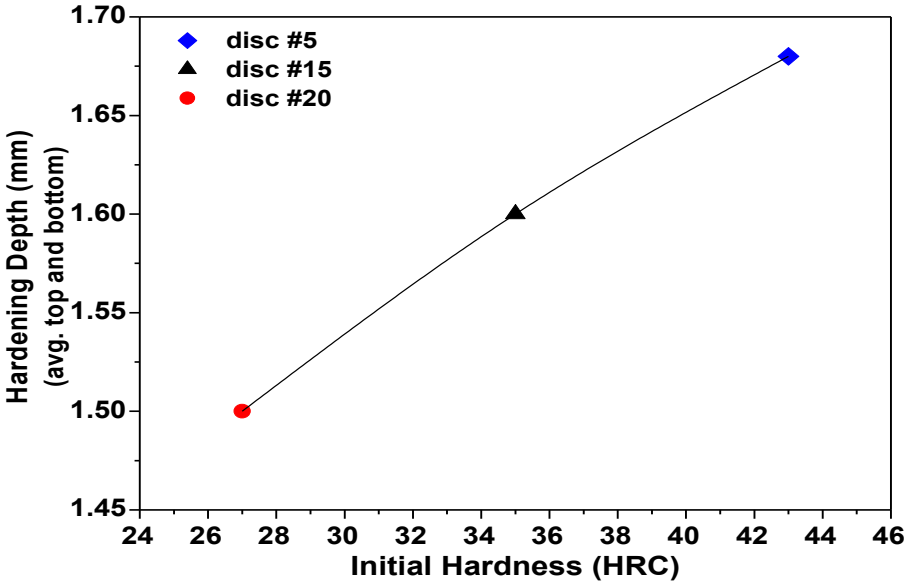

(a)

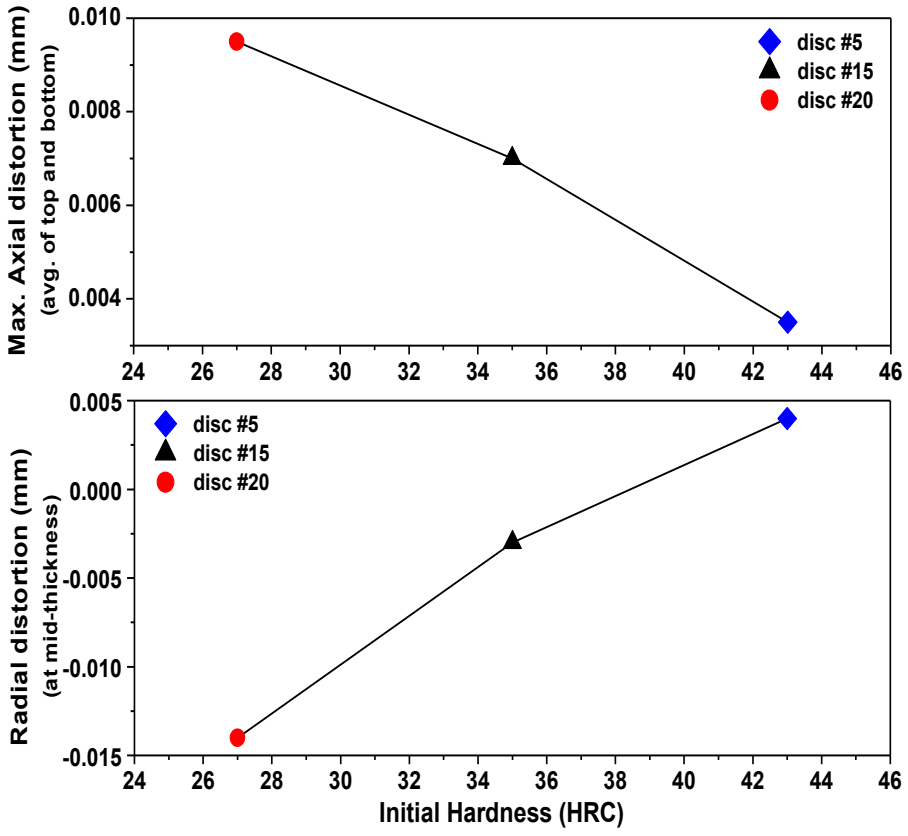

(b)

Fig 4.23: Hardening depth and distortion variation with initial hardness under the same induction hardening recipe, in terms of disc #5, #15 and #20: (a) hardening depth versus initial hardness; (b) distortion versus initial hardness

4.3 Full Characterization of Disc #7

As mentioned earlier, disc #7 is a selected key sample which was induction hardened by a duplicate recipe to disc #5 and was then employed in not only distortions but also residual stresses and micro-hardness measurements. This has been done in order to have a better understanding of the induction hardened sample behaviors and further establish a relationship between sample distortions, residual stresses as well as micro-hardness.

4.3.1 Distortion result

Figs 4.24 (a) and (b) demonstrate the axial distortion profiles (on top and bottom surfaces) and the radial distortion profile of disc #7, respectively, measured along -Y-axis (measuring angle of 0˚). A usual symmetric convex pattern appears on the axial distortion profile (Fig 4.24(a)) in the region close to the disc outside surface. The radial distortion profile along the disc thickness exhibits a regular convex pattern as well, with the maximum positive in the vicinity of disc mid-thickness position (Fig 4.24(b)). This suggests that both the axial and the radial distortion profiles of disc #7 are quite similar to those of disc #5 (Fig 4.10), owing to the same induction hardening recipe applied to both samples. However, regarding the slight discrepancy in the distortion size between discs #7 and #5, it could be considered as the experimental error. However since this difference is only around 1μm, it can be neglected.

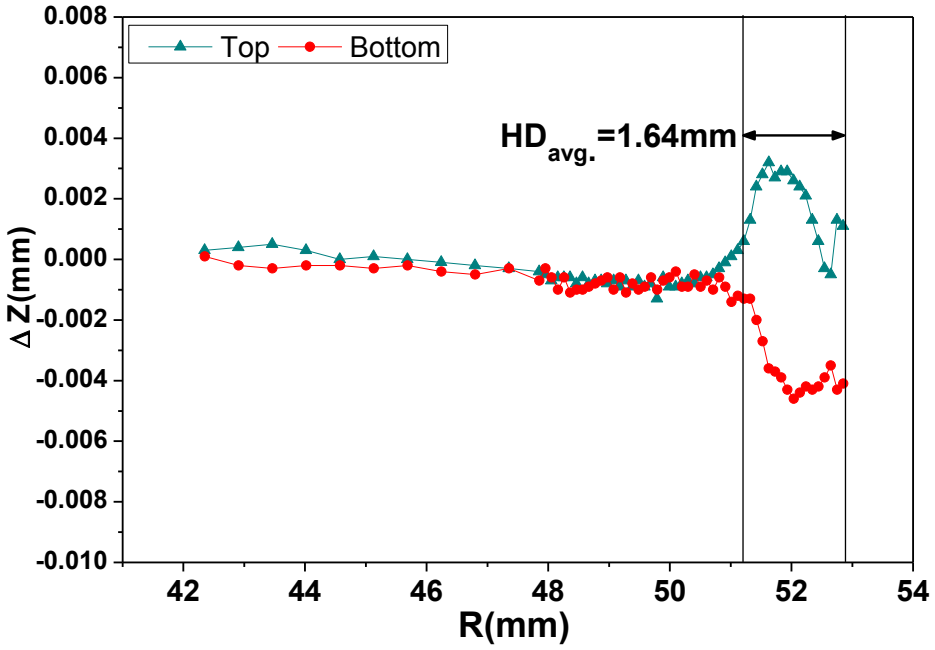

(a)

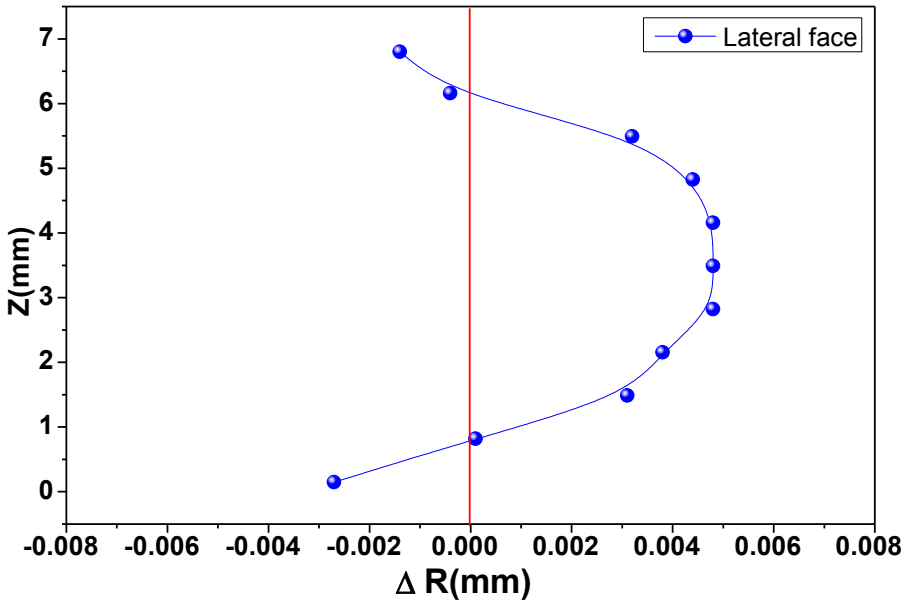

(b)

Fig 4.24 Distortion profiles of disc #7 (measured at 0˚): (a) axial distortion profiles on the top and bottom faces along radius of the disc; (b) radial distortion profile on the lateral face along thickness of the disc

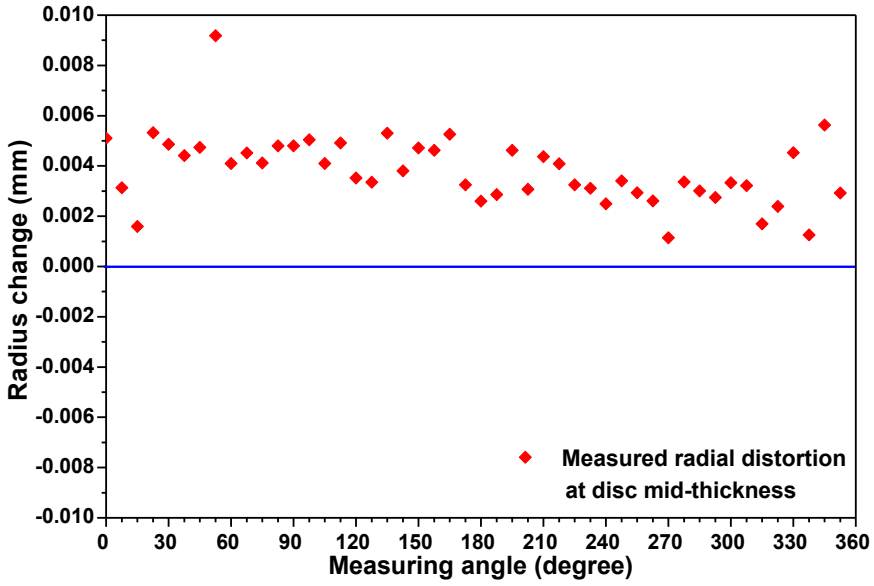

(a)

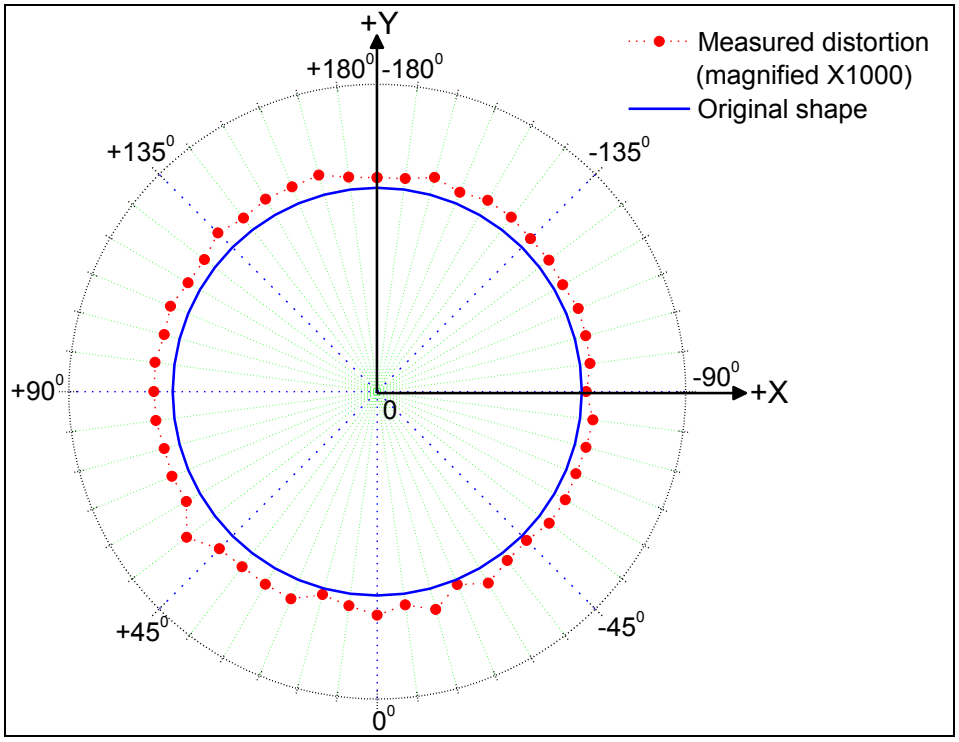

(b)

Figure 4.25: Radius changes (radial distortion) variations of disc #7 around the disc, measured at the mid-thickness position of the disc: (a) one dimensional view; (b) 2D map

Besides, Figs 4.25 (a) and (b) illustrate the radial distortion variations around the disc under each given measuring angle. It reveals that the disc radius at mid-thickness always shows an expansion behavior after the induction hardening process, no matter at which measuring angle. Moreover, an agreement is found when comparing the radial distortion at measuring angle of 0˚ in Fig 4.25(a) with the radial distortion at the mid-thickness (Z=3.5mm approximately) shown in Fig 4.24(b). Both of them display an expansion in radius around 0.005mm at the mid-thickness position. However, with respect to the scatter in the radial distortion measurements, it could be ascribed to the experimental error or probably the non-uniform temperature gradient formed during the induction heat treatment. Similar roundness examinations on sample suffered different heat treatment have been reported by other researchers [65-67].

4.3.2 Micro-hardness result

A typical hardness profile after induction hardening treatment is in the literature [77] and cited in Fig 4.26 as a reference for comparison with the present hardness studies. As illustrated, z1 to z4, in order, represent the hardened zone, the zone made of a mixture of fresh (hard) and tempered Martensite, the over-tempered zone and finally the zone non-affected by the induction treatment. The related characteristic temperature range during the induction hardening process is provided at the top of this figure as well.

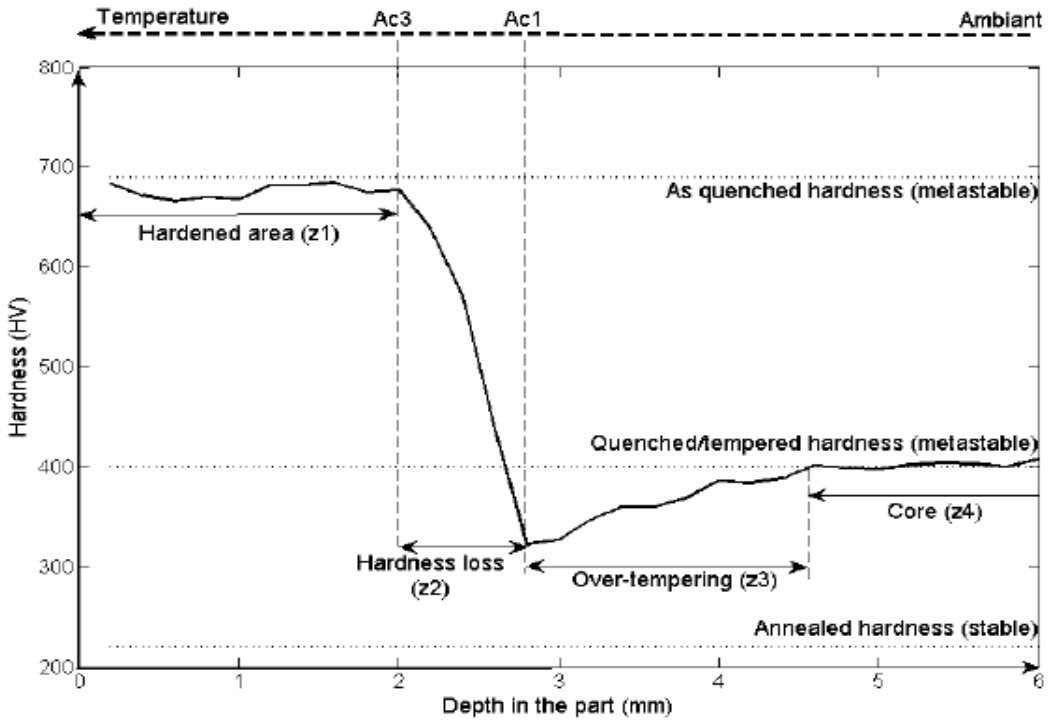

Fig 4.26: A typical hardness profile obtained after IH treatment on AMS 6414 steel [77]

Fig 4.27 illustrates the three thickness positions which the micro-hardness test performs at. As explained before (in chapter 3), the micro-hardness measurement is carried out at top-, middle- and bottom-thickness positions along the radius (see Fig 4.27).

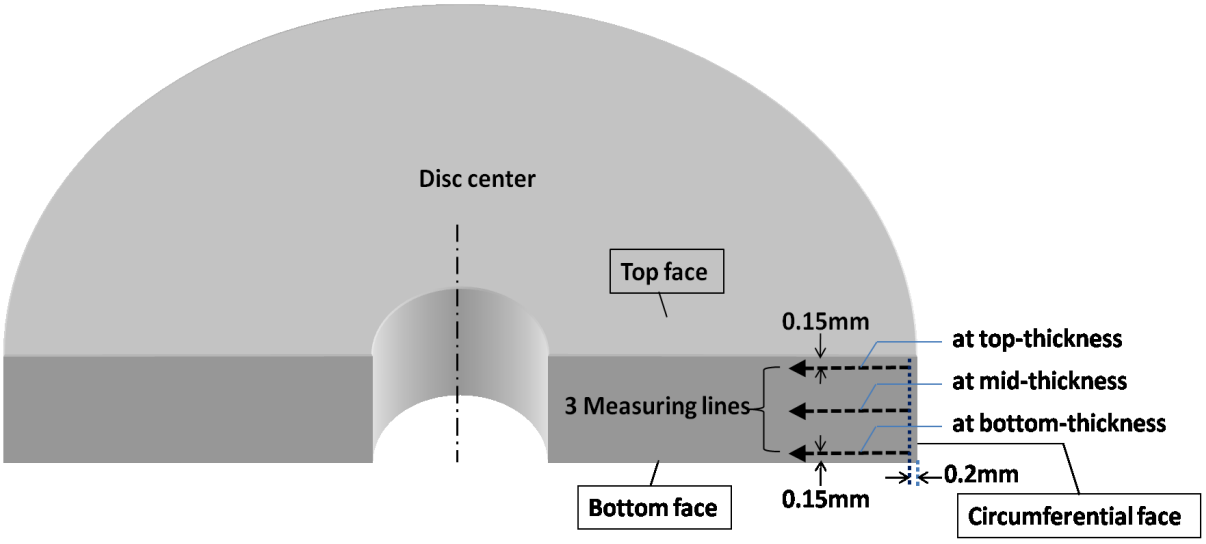

Fig 4.27: The schematic sketch of the micro-hardness measurement path at three different thickness positions of disc #7

The micro-hardness profiles obtained at two angles 0˚ (-Y-axis) and 180˚ (+Y-axis), for disc #7 after induction hardening treatment through these three thickness positions, are shown in Fig 4.28(a) and (b), respectively. A hardness profile comparison between these two angles (0˚ and 180˚), only considering the mid-thickness position, is presented in Fig 4.29 to provide a clearer view. Besides, the corresponding vertical cross-section view of the hardening depth contour across the thickness of disc #7 after IH treatment is shown in Fig 4.30. The detailed hardening depth results at three thickness positions (top-, mid- and bottom-thickness) at these two angles are summarized in Table 4.9.

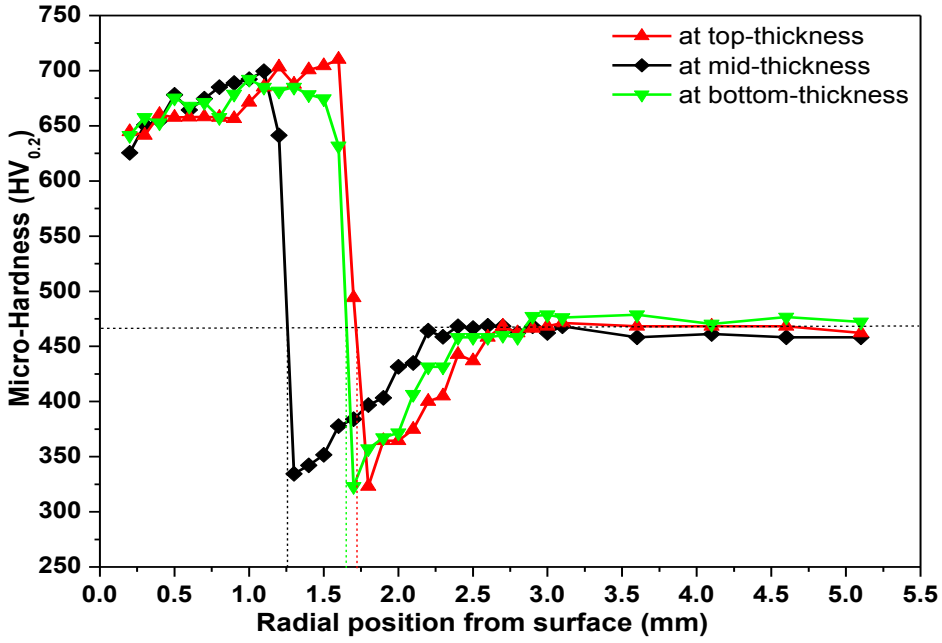

(a)

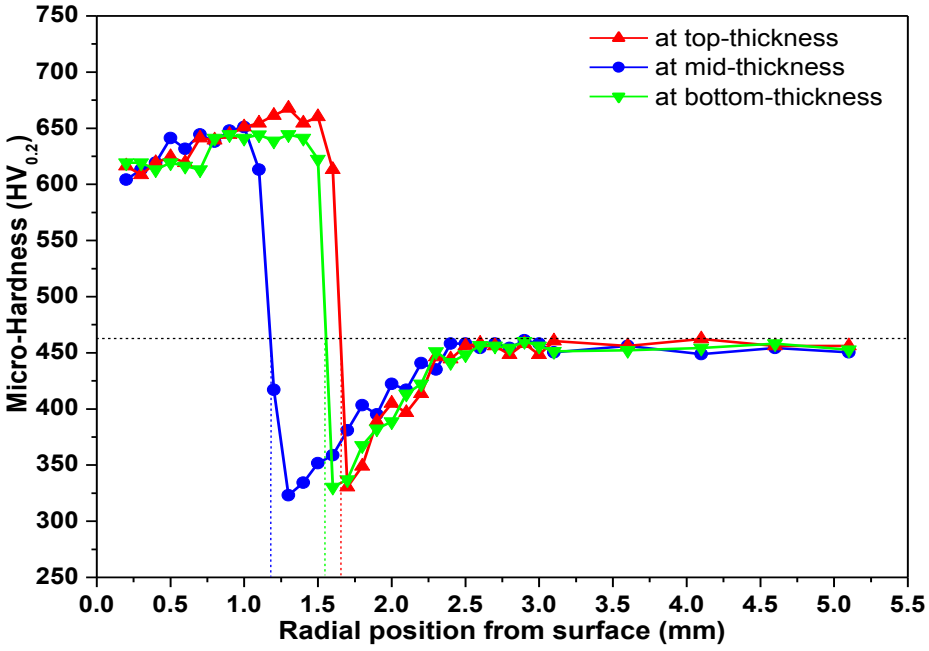

(b)

Fig 4.28 Hardness profiles obtained through three thickness positions: (a) at angle=0˚ (–Y-axis); (b) at angle=180˚ (+Y-axis)

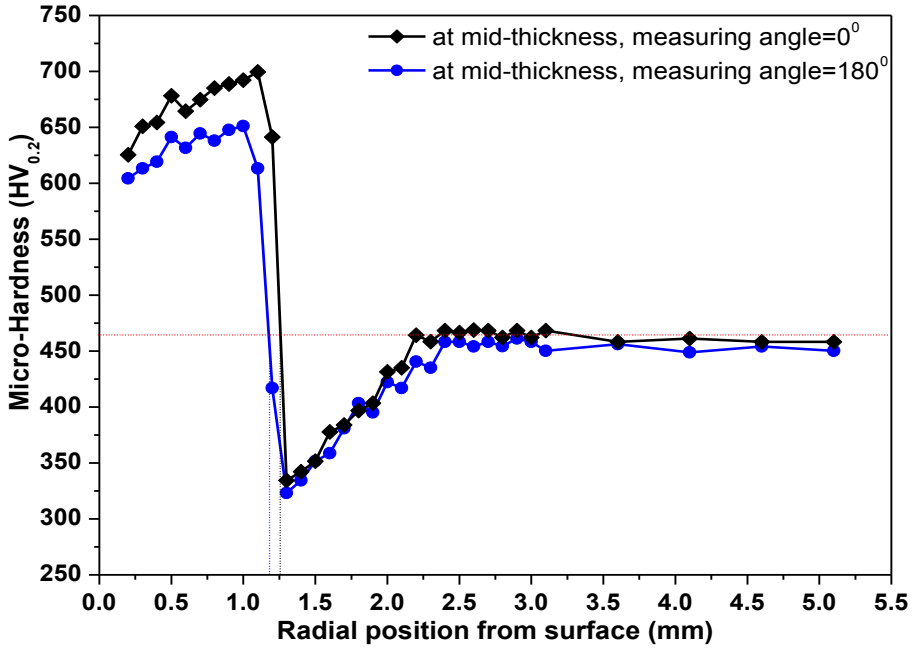

Fig 4.29: Comparison of the mid-thickness micro-hardness profile between measured at angle=0˚ (-Y axis) and angle=180˚ (+Y-axis)

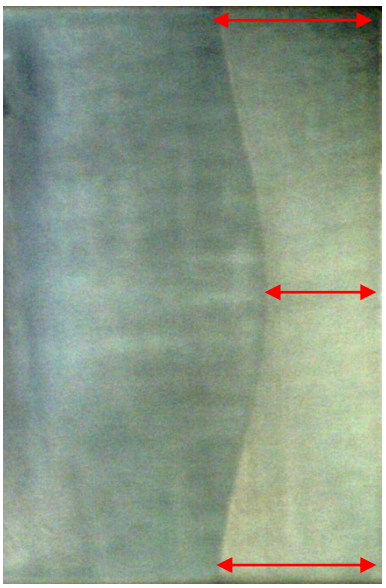

Fig 4.30 Vertical cross-section view of the hardening depth contour across the thickness of disc #7, measured at angle=0˚

Table 4.9 Hardening depth of disc #7 at three thickness locations of angle=0˚ and 180˚

Hardening depth (mm)	**At measuring angle of 0˚**			**At measuring angle of 180˚**		
	Top-thickness	**Mid-thickness**	**Bottom-thickness**	**Top-thickness**	**Mid-thickness**	**Bottom-thickness**
	1.72	1.25	1.68	1.68	1.20	1.55

It has been observed from Fig 4.28 (a) that the micro-hardness distributions along radial directions measured at mid-thickness, top-thickness and bottom-thickness have similar trends. Also, they are rather similar to the typical hardness profile in Fig 4.26. As shown, all three curves demonstrate a typically high hardness value varying from $625HV_{0.2}$ to $700HV_{0.2}$ near the surface. This is consistent with the normal hardness value in the hardened layer of similar material (AMS 6414) reported by others [72, 78], suggesting a hardened zone (z1). This region followed by a sharp decrease until reaching a minimum around $320HV_{0.2}$, indicating the hardness loss zone (z2). Then, the hardness gradually goes up to approximately 470 $HV_{0.2}$, forming the over-tempered zone (z3). Afterwards,

the hardness keeps a nearly constant value around 470$HV_{0.2}$ in the core material. This is the same value as the initial hardness before induction hardening and therefore reveals the non-affected zone (z4).

The slight rise in the hardness of the surface hardened layer with moving toward the center was also observed by Grum [5]. This could be explained by the formation of very fine martensitic microstructure in the inner region of the hardened layer. Essentially, this is owing to the non-uniform cooling rates in the disc surface during the IH process. The "groove" in the hardness profile, which occurs between the region close to the surface and nearby the core demonstrating the so-called over-tempered zone (z3), is a fairly common feature for a fast heat treatment. This is due to the tempering effect of the thermal flow happening during the IH treatment [77]. More detailed study on the entire hardness profile especially the over-tempered zone of the induction hardened specimen was reported by Ducassy [78]. Further, comparing the hardness profile with the relevant distortion pattern shown in Fig 4.28 (a), one can find that the largest axial distortions occurs exactly in the over-tempered zone of the hardness profile. This could be simply understood by the fact that lower hardness material is relatively easier to undergo deformation.

Analyzing the hardening depth at the mid-, top- and bottom-thickness, a distinct difference has been noted. In the present study, the hardening depth is defined as the radial position where the hardness profile intersects with the horizontal core hardness line

(indicated by the horizontal dashed line in Figs 4.28 and 4.29). Clearly, the hardening depth measured at top-thickness and bottom-thickness are very close to each other and are in the order of 1.6~1.7mm. However, they are considerably larger than the mid-thickness hardening depth which shows a value of only around 1.2mm. This variation in the hardening depth has been viewed as a result of the edge effect caused by induction hardening and is further described in details elsewhere [73].

Generally speaking, Fig 4.28(b) is quite similar to Fig 4.28(a). The only slight difference is the hardness magnitude of three hardness profiles in the hardened layer, which varies from $625HV_{0.2}$ to $700HV_{0.2}$ in Fig 4.28 (a) and $600HV_{0.2}$ to $670HV_{0.2}$ in Fig 4.28 (b). However, for the minimum hardness in the over-tempered area and the uniform hardness in the core material, no noticeable difference is observed.

In Fig 4.30, the red arrows indicate the hardening depth at the top-, mid- and bottom-thickness of the disc. A clear and characteristic hardened case profile has been exposed with a convex shape towards the lateral face. This suggests a smaller hardening depth at the mid-thickness position and accordingly confirms the previous conclusion drawn from the relevant hardness profiles. Table 4.9 shows again that the results are in accord with each other. The maximum difference between two corresponding thicknesses is 0.13mm.

4.3.3 Residual stress result

The results of the residual stress measurements of disc #7 using neutron diffraction (ND) are discussed in details in this section. Prior to the stress analysis, the analysis of the reference d_0 result is necessary.

4.3.3.1 Reference d_0 result

It should be noted that the ND-determined radial and hoop stress-free lattice spacing (d_0) distributions are obtained at the same mid-thickness position of the comb specimen which is described in section 3.5. Fig 4.31 shows the d_0 distributions obtained by ND in present work and its comparison with that determined by XRD in previous work (based on an induction hardened 4340 disc, but the induction heating time is relatively longer), as well as the reference constant d_0 value of 4340 steel based on the X-ray machine database[79].

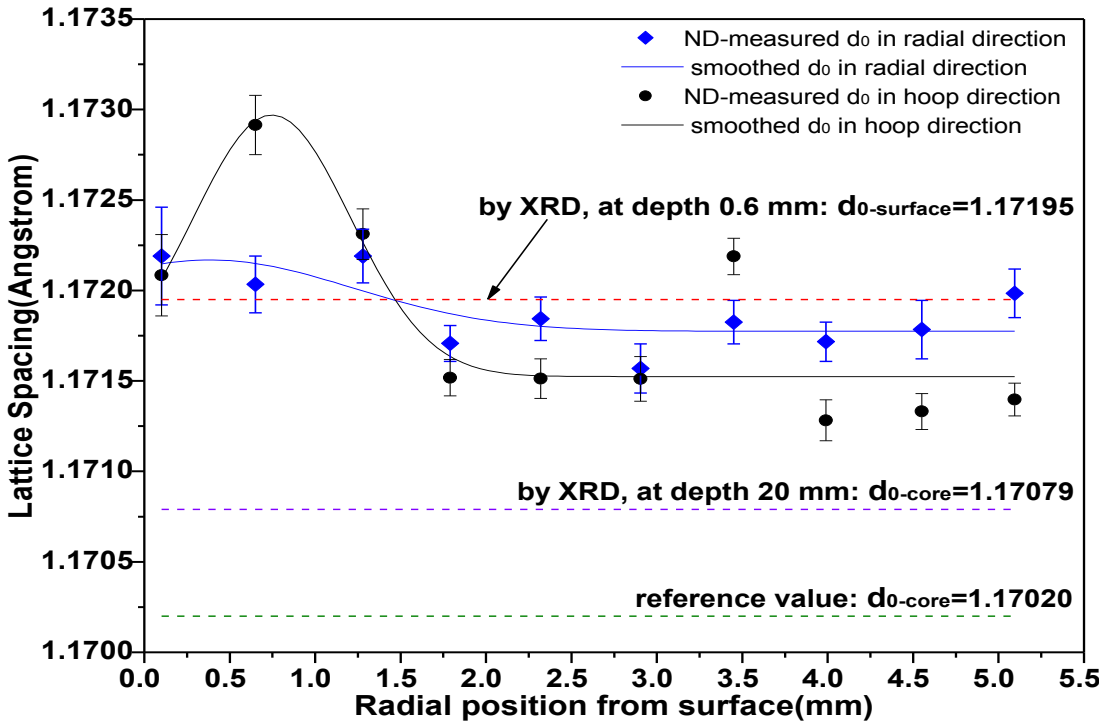

Fig 4.31: {112} radial and hoop stress-free lattice spacing (d_0) distributions along disc radius, determined from the comb specimen

Firstly, attentions are paid to the ND-measured stress-free lattice spacing (d_0) of the *{112}* planes shown in Fig 4.31. In the hoop direction, the d_0 value firstly demonstrates an increase near the surface, reaching a maximum of 1.1729Å, then followed by a diminishment with increasing depth through the hardened case and finally approaching a constant value of approximately 1.1715Å at a depth of around 2.0mm. A point deviating from the trend is observed at around 3.5mm. This point is ignored from the smoothed pattern but the cause of the deviation of this point has not been fully understood. One possible reason could be related to the impact of the wire-EDM machining applied to the comb production process. For example, if the tooth corresponding to the deviation point is affected by the wire-EDM machining largely than other teeth, the measured d_0 data on

this tooth is not reliable. Concerning the data in the radial direction, there is only a small variation in the stress-free lattice spacing near the surface unlike the noticeable increase observed for the hoop direction. This is followed by a smooth decrease towards the inside and finally reaching a constant value of approximately 1.1718Å at 2.2mm.

Clearly, in ND measurement, both the hoop and the radial stress-free lattice spacing present a relatively higher values close to the surface than towards to the core. This may be due to the presence of C (carbon) in the Martensite lattice of the surface layer leads to the increase of atomic spacing during the Martensite transformation process [80]. However, since the core material does not undergo any phase transformation-keeping the unaltered microstructure (unstable tempered Martensite) during the IH treatment, the d_0 shows a relatively smaller size and displays a nearly constant value till the center of the disc. For the transition area, which has a mixed microstructure of that in the surface and in the core, the corresponding d_0 consequently displays a decreasing tendency towards the inside.

In addition, it is worth noting that data scattering has been observed for both the hoop and radial directions. The exact reason for this variation, again, has not been completely understood. It is possibly due to the uncertainty and errors of ND experiment or the issues stemming from the sample machining processes (e.g. the wire-EDM process may alter the original state of this comb reference sample).

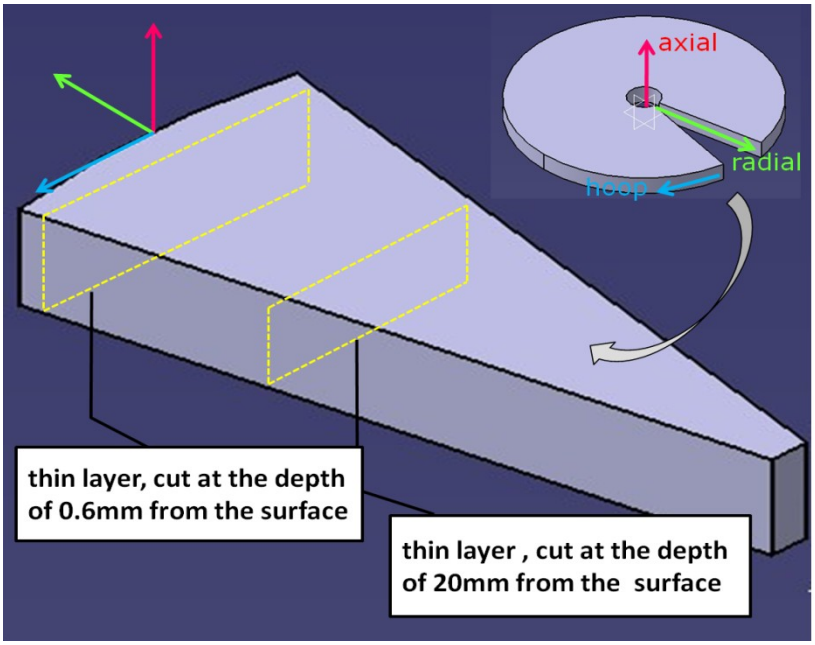

Fig 4.32 Thin layers preparation for d_0 measurement by XRD

Now, based on Fig 4.31, a comparison is made between the ND-determined d_0 profile in radial direction and the two d_0 data obtained by XRD experiment. As illustrated in Fig 4.32, these two d_0 values are measured from two thin (0.07mm) layers which are cut from a similar induction hardened disc at the depth of 0.6mm and 20mm from the surface, separately. Since the layer is very thin, it is assumed that there is no residual stress existed in the normal direction of the layer. This means the d_0 in the radial direction of the disc can be obtained. As indicated by two dashed lines in Fig 4.31, the d_0 values at the depth of 0.6mm and 20mm are 1.17195Å and 1.17079Å, respectively. The hardening depth at this case is around 1.6mm and the larger value of d_0 is related to the Martensite microstructure at the outside layer of the sample. In both, the ND and the XRD measurement demonstrate larger values near the surface, but the values determined by XRD and ND are somewhat different. The XRD-determined $d_{0\text{-}surface}$ value is close to the

ND-determined radial d_0 values at the near surface area, but a considerable discrepancy happened between the $d_{0\text{-}core}$ values in the core material. The ND-determined d_0 is clearly larger than the $d_{0\text{-}core}$ of XRD, and they are both larger than the reference constant d_0 value of the 4340 steel. This discrepancy of the d_0 value, however, could probably be attributed to the different diffraction angle (2θ) used in ND and XRD measurement, the system errors and also maybe the inherent difference existed in the investigated sample.

Similar stress-free lattice spacing investigations have been done in recent years. Prevey and Mason [81] calculated the d_0 depth distribution of an induction hardened sample based on the obtained stress data. Their result is quite similar to the hoop one shown in Fig 4.31 in present study. The calculated d_0 profile showed a reduction at the surface and a fluctuation in the core material. Besides, by virtue of ND approach, Ezeilo and Webster [63] reported the d_0 distribution of a laser hardened weld specimen where their results demonstrated a significant variation of d_0 in the hardened layer. Nevertheless, the information of the experimental-based d_0 depth profile for samples' stress determination is still limited in the literature, even for the weld specimens (the parts often display local composition variations). The lack of induction hardened d_0 data in the literature makes it difficult to compare the d_0 result between present study and the others' work.

In addition to all above, one thing should be noted that each point shown on the ND-measured d_0 profiles are the actual stress-free lattice spacing data obtained from the neutron diffraction experiment on each teeth of the comb sample. 10 teeth enable 10 d_0

points available in the 5mm measurement length. However, for obtaining the residual strains with a smaller gradient (e.g. residual strains measurement was taken every 0.2mm in the sample's hardened layer), d_0 at finer spacing is required. Hence, interpolation of the smoothed d_0 profile is used. The effect of d_0 depth distribution in the calculation of residual stress fields are discussed next.

4.3.3.2 Disc residual strain and stress results

As previously indicated, the residual strains measurements by ND are performed on a disc sample at mid-thickness from around 0.2mm beneath the circumferential surface until at a depth of about 5.0mm approximately. The residual stress results in three directions are calculated from the measured strains based on Equation 2.

Considering that there are two d_0 profiles (d_0 in radial and d_0 in hoop direction) obtained from ND measurement and both of them could be used for the residual stress determination, the comparisons of the residual stress distribution based on these two d_0 profiles are therefore made in hoop, axial and radial directions, respectively, along the radius of the disc, as shown in Fig 4.33(a) to (c). Besides, the ND stress calculations based on the two d_0 values obtained by XRD (see Fig 4.31) as well as the previous XRD results are also given in Fig 4.33(a) and (b) for comparison. One thing should be clear that the hardening depth (HD) indicated in following figures is the value measured at the mid-thickness position of disc #7, at the same measuring angle where the residual stress measurement applied on.

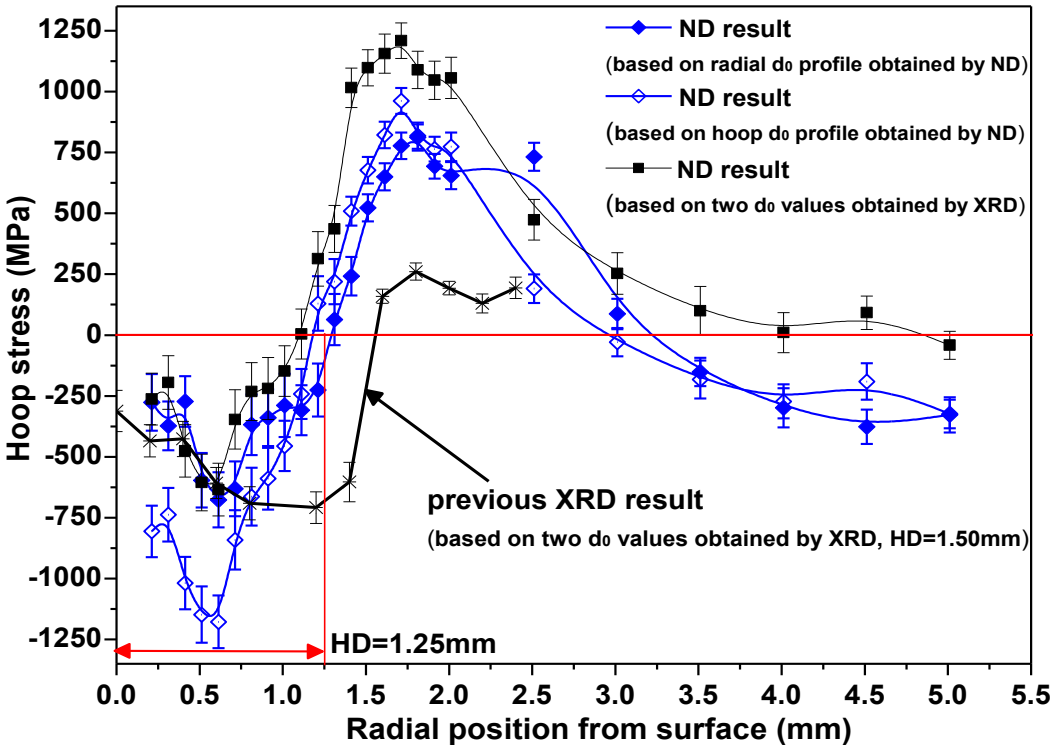
ND result
(based on radial d0 profile obtained by ND)
ND result
(based on hoop d0 profile obtained by ND)
ND result
(based on two d0 values obtained by XRD)
previous XRD result
(based on two d0 values obtained by XRD, HD=1.50mm)
HD=1.25mm
Hoop stress (MPa)
Radial position from surface (mm)
1250
1000
750
500
250
0
-250
-500
-750
-1000
-1250
0.0
0.5
1.0
1.5
2.0
2.5
3.0
3.5
4.0
4.5
5.0
5.5

(a)

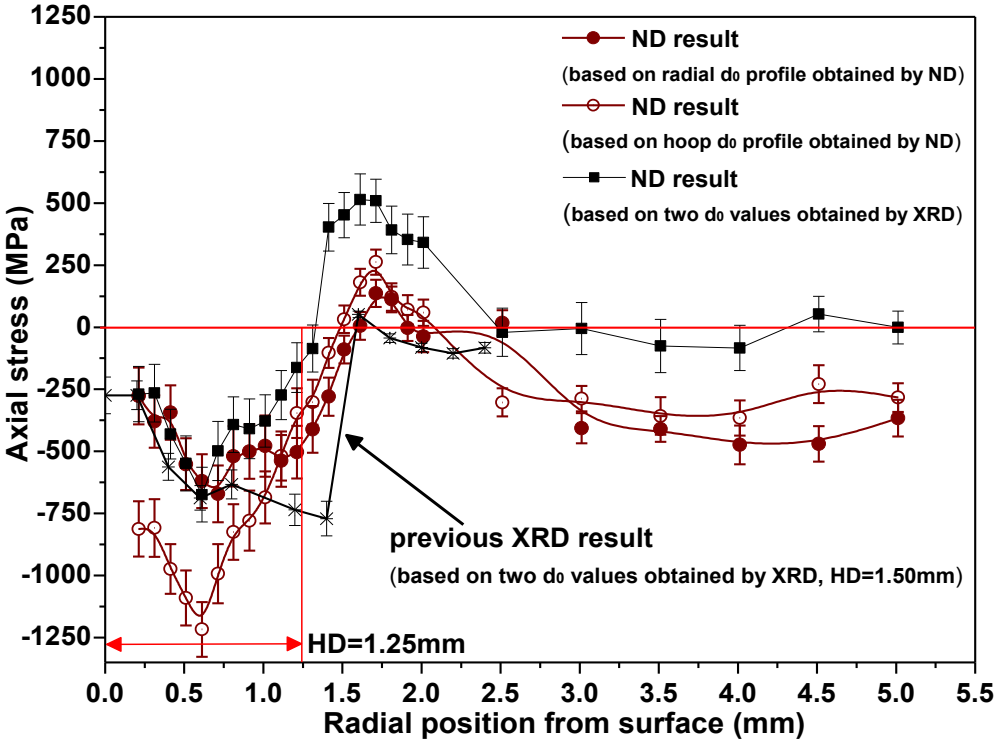
ND result
(based on radial d0 profile obtained by ND)
ND result
(based on hoop d0 profile obtained by ND)
ND result
(based on two d0 values obtained by XRD)
previous XRD result
(based on two d0 values obtained by XRD, HD=1.50mm)
HD=1.25mm
Axial stress (MPa)
Radial position from surface (mm)
1250
1000
750
500
250
0
-250
-500
-750
-1000
-1250
0.0
0.5
1.0
1.5
2.0
2.5
3.0
3.5
4.0
4.5
5.0
5.5

(b)

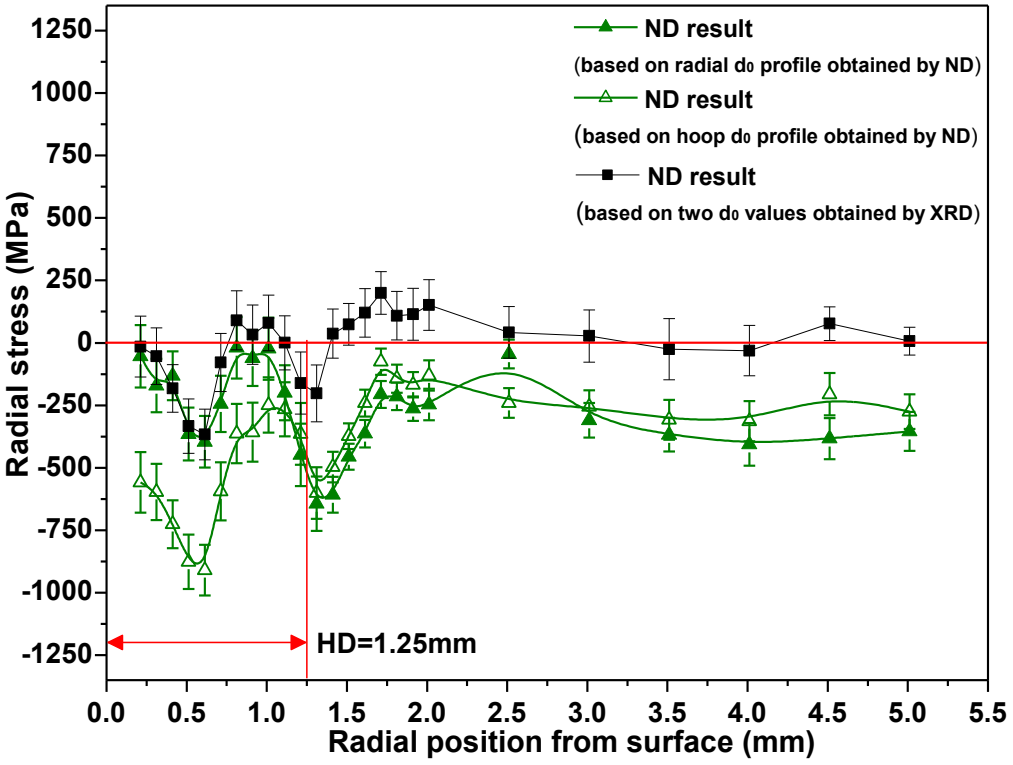

(c)

Fig 4.33 Comparisons between the residual stress results obtained by ND in present study and that by XRD in previous work: (a) in hoop direction; (b) in axial direction; (c) in axial direction (the previous XRD result is not available). Here, the ND result are calculated based on both (radial and hoop) d_0 profiles obtained by ND and two d_0 values obtained by XRD in Fig 4.31; the previous XRD result is calculated based on two d_0 values measured by XRD in Fig 4.31.

As can be seen from Fig 4.33(a) to (c), the general trend of the residual stress obtained from the d_0 measured in the radial direction by ND is quite similar to that obtained from one given by in the hoop direction. The significant difference of the strain or the stress only happens at the near surface area. This could be understood by the significant difference of the d_0 value shown between the hoop and the radial direction at the near surface area (as displayed in Fig 4.31). In the range of around 1.2mm from the surface, both the residual stress based on the d_0 in the radial direction demonstrate a smaller

negative value than that obtained from the d_0 obtained in the hoop direction. Besides, the ND stress result based on the two d_0 obtained by XRD shows a similar stress profile to that determined by ND-measured d_0, except that the overall stress profile shifts up which makes it much closer to the zero in the core.

If comparing the three ND stresses in Fig 4.33(a) with the corresponding ones in Fig 4.33(b), it is found that in the hardened layer the stress profiles in hoop direction are quite similar to that in axial direction. This is also observed from the previous XRD results shown in Fig 4.33(a) and (b). Hence, it could be supposed that in the hardened layer, the residual stress in the hoop and in the axial directions are somewhat comparable. For the depth beyond the hardened layer, however, only the stress in hoop direction shows a noticeable tensile stress which suggests a critical stress state. In addition, the hardening depth of the induction hardened disc (4340 steel) used for previous XRD study is 1.60mm, larger than that of present sample. This is due to the different IH recipe (longer heating time) applied to the previous sample.

Based on above residual stress analysis, it can be seen that the stress can vary to a certain extent with the different d_0 reference used. For present study, although the ND-based two d_0 profiles are somewhat questionable (e.g. the scattering data found), the better choice is still using the hoop d_0 profile and the radial d_0 profile obtained by ND to calculate the corresponding hoop and radial residual strain/stress, respectively, other than using the two d_0 data obtained by XRD or the d_0 constant to make the stress calculation. Since the

axial d_0 profile is missing, the averaged value of the ND-measured d_0 in the radial and hoop direction is applied to calculate the residual strain/stress in the axial direction. The relevant residual strains and stresses distributions (based on ND-measured d_0) in these three directions along the radius of disc sample are shown in Fig 4.34(a) and (b) respectively. Additionally, only in the purpose of comparison, the residual strains and stresses profiles based on the two XRD-determined d_0 values are also given in Fig 4.35(a) and (b).

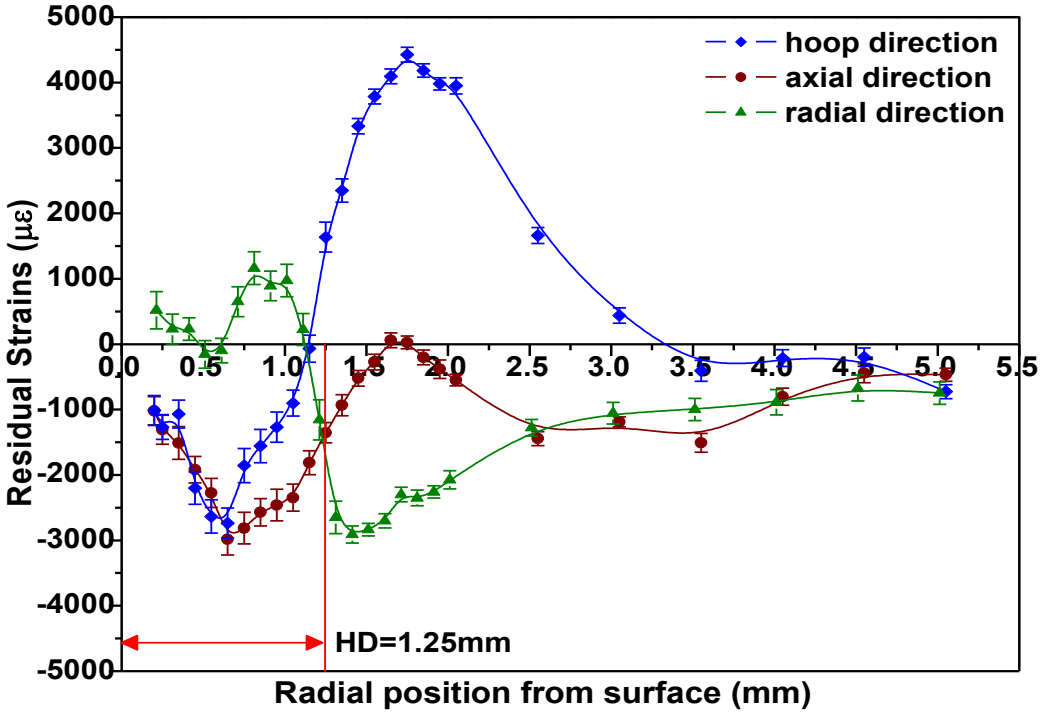

(a)

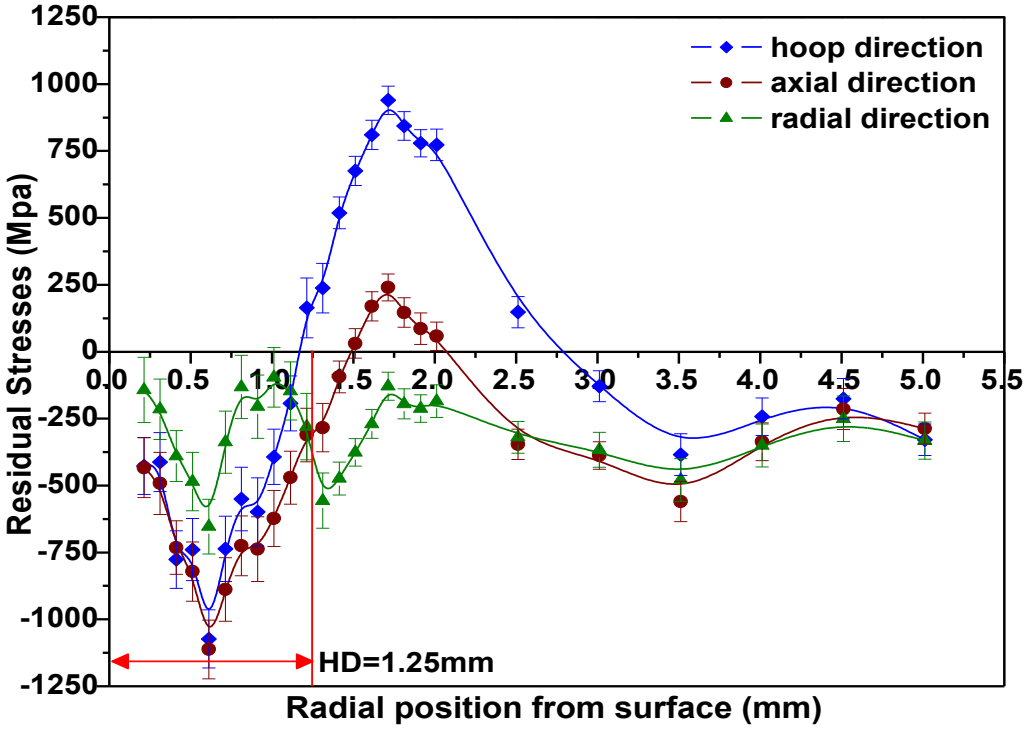

(b)

Fig 4.34: Disc #7 residual strains and stresses results based on ND-measured d_0: (a) residual strains distributions in three directions; (b) residual stresses distributions in three directions

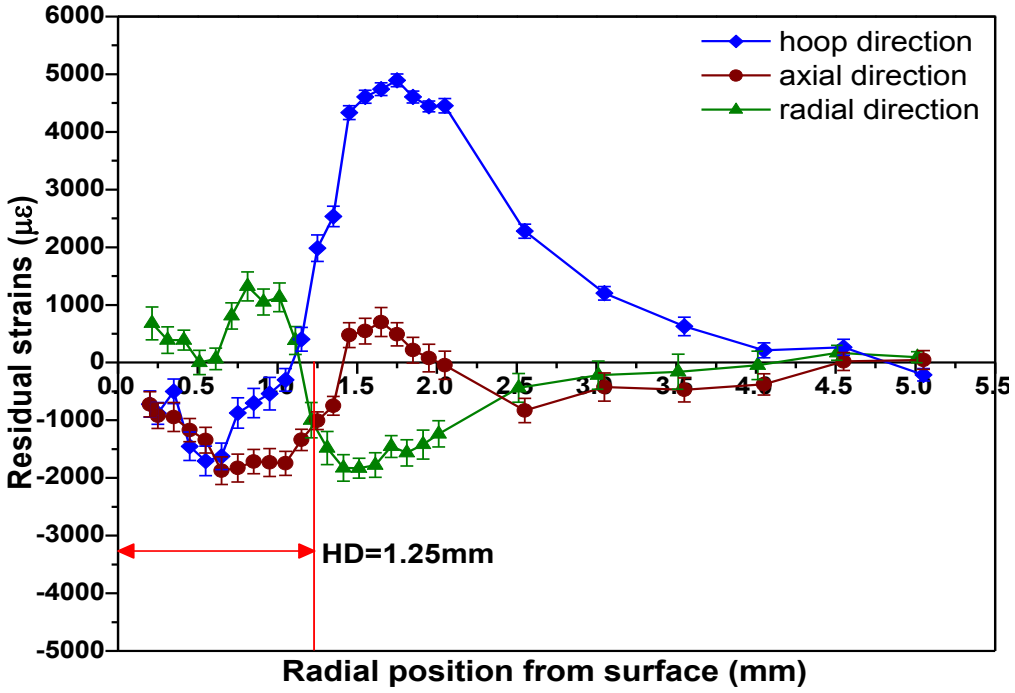

(a)

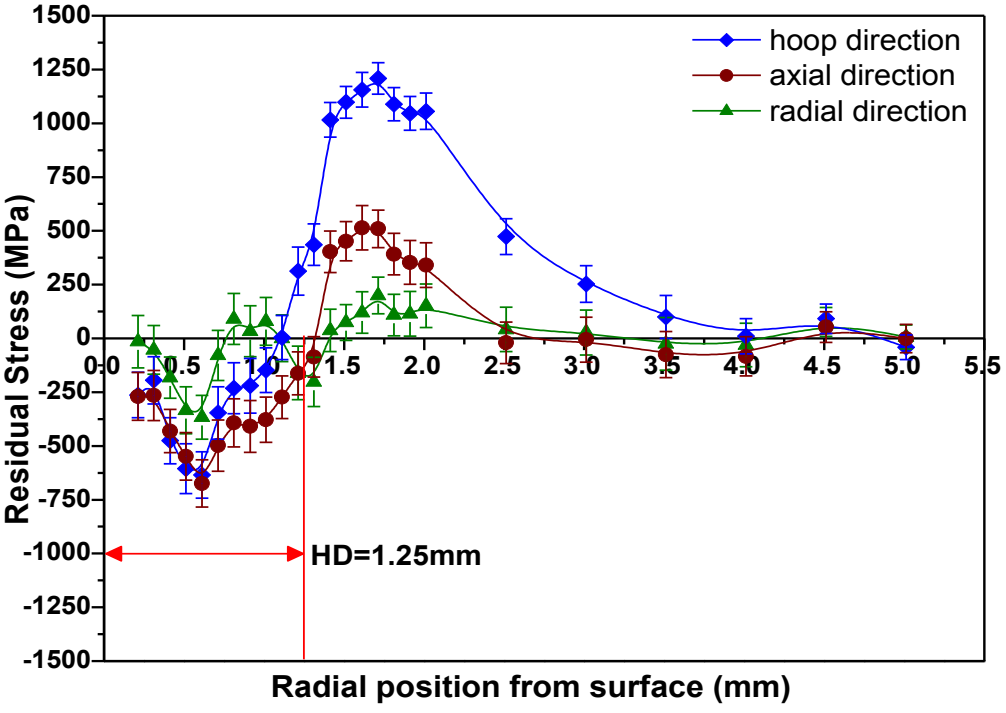

(b)

Fig 4.35: Disc #7 residual strains and stresses results calculated based on the two d_0 values obtained by XRD: (a) residual strains distributions in three directions; (b) residual stresses distributions in three directions

As can be seen from Fig 4.34(a), the hoop strain is compressive near the surface, turning to tensile towards the disc center at radial position of approximately 1.2mm and then gradually approaching to zero. A quite similar shape of strain depth profile has been observed in the axial direction but the value of the axial strain is negative throughout the radius. As for radial strain, in contrast, it is tensile near the surface, altering to compressive and afterwards closing to zero at the core. Such radial strain distribution, which more or less displays an opposite strains tendency along radius to hoop and axial directions, is reasonable to some degree since it suggests a material deformation balance: two directional compressive deformations should be accompanied with one directional tensile deformation. However, the reduction in the radial strain appeared within 0.5mm below the surface is unexpected and has not been fully understood.

The triaxial stress distributions are calculated and shown in Fig 4.34(b). As expected and reported in other published works [54, 55] on induction hardened samples, it reveals a compressive residual stress field in the hoop and axial directions in the area close to the surface. Then a reversal into tensile stress happens at the radial depth of 1.2mm from the surface in hoop direction and 1.5mm in axial direction. The maximum compressive stress in hoop and axial directions are quite close, both on the order of -1120MPa, and they are observed at exactly the same radial position (~0.65mm) from the surface. Besides, a maximum tensile stress is also found in hoop direction with an approximate value of 930 MPa whilst the axial one is much smaller, only 250MPa. It implies that disc hoop

direction encountered the most critical stress condition (maximum tensile stress and largest change) over the other two directions, and this is relatively normal for heat-treated cylindrical samples as reported by other researchers, such as [82, 83]

The stress in the radial direction, which in most cases is supposed to be an almost constant value close to zero or only showing a slight tensile over the whole radial positions [11], it found to be always compressive here and demonstrates a considerable variation along the radial positions within 2mm from the surface. This finding is somewhat puzzling and contradicts the relevant results obtained by others [55, 81, 84], for example. Nevertheless, Douglas J. Hornbach et al. [54] reported an induction hardened gear with large variation in radial residual stress using XRD investigation. In present study, the obvious variation in the radial direction can be attributed to the relatively large experimental uncertainty (indicated by the error bars in Fig 4.34) resulted from the neutron diffraction experiment, especially investigating the strains at near-surface area. For example, in the ND stress measurement, the overlapped and broad double-peak diffraction pattern occurred in the near surface area of the disc sample. This could suggest a multi-phased hardened layer where the phases are highly distorted. However, considering these two peaks are largely overlapped, such double-peak pattern was finally treated as a single peak. The single peak center location is determined by a Gaussian fit, which has been discussed in detail by Hutchings [28] for ND-based stress measurements. As seen, such kind of data processing can be considered as a source of

error particularly at the near-surface area. According to the calculation of Δd/d (precision in strain), the near-surface area of the sample demonstrate a slightly larger value ($>2\times10^{-4}$) than that near the core (between1×10^{-4}~2×10^{-4}).

In stress research field, the problem and challenge of residual stress studies in subsurface area of the surface enhancement sample has been attracting great attention all the time. Some researchers agreed that the strains measurement in the near-surface area is still troublesome whether X-ray or even neutron diffraction methods were used [28, 55, 85, 86]. For example, in the near surface, if the significant stress gradient existed in the XRD irradiated area or the ND sampling volume, the assumed constant stress condition in the targeted area or volume used for stress calculation will cause error and affect the stress results [85]. Considering this and also the issue of d_0 determination (discussed before), the present radial residual stress profile is questionable to a large extent, particularly in the close-to-surface region, and it cannot be further used as the ground to draw the conclusion of the real radial stress field within the material.

Now, keeping an eye at the radial depth after 2.5mm, the three stress profiles gradually merge towards the center. They nearly coincide at the radial depth of around 5.0mm, where probably insinuates the beginning of the non-affected core region of the sample. Since the three component residual stresses should be all approaching to zero in the core material due to the nature of residual stress [7, 11, 27] and this has been proved by numerous experimental works (e.g. the radial residual stress depth profile measured by

ND [84] and XRD [87]), the present uniform stress value of -250MPa approximately could be similarly explained by the significant uncertainty originated from the neutron diffraction technique.

Very commonly, the residual stress distribution is always related and combined with the corresponding hardness profile. The hardness depth profile along radial positions as depicted in Fig 4.29 has highly conformed to the relevant residual stress distributions shown in Fig 4.34(b). Firstly, due to the Martensite microstructure formed in the disc hardened layer, the residual stress demonstrates compressive value and meanwhile the corresponding micro-hardness shows a high value. Besides, the maximum compressive residual stress in hoop, axial and even the radial directions are both observed at somewhere below the surface, which could be closely linked to the slight increase of hardness in the surface hardened region. The real reason for this is not clear so far. However, one explanation could be the very fine Martensite formation happening at a certain depth below the surface according to Grum [5].

Moreover, in the present case, the hardness profile (Fig 4.29) displays a sharp drop in transition area. Meanwhile, the residual stress profile, for example, in the hoop direction (Fig 4.34(b)), also demonstrates a relative steep transition from compressive to tensile. This could suggest that the hardness variations in the transition area (an area defined by the range between the hardened and core material zone of the hardness profile) can affect the residual stress transition shape. A steeper reduction in hardness may contribute a

sharp change of residual stress. This finding is in agreement with the reported standpoint mentioned by Grum [5]. In addition, Grum also pointed out that when the hardening depth of the induction hardened sample is less than 2mm, the stress transition from compressive to tensile usually occurs in obedience to the transition zone in hardness profile. Clearly, our case highly supports this statement.

In the present case, both the hoop and the axial residual stress transition points are exactly located within the transition zone of the corresponding hardness profile and the measured hardening depth is 1.25mm, smaller than 2mm. Furthermore, with respect to the radial positions after 2.5mm until around 5.0mm below the surface, the hardness distribution and the three residual stress profiles show a consistent trend. Both of them approach to a nearly constant value towards the core. This reveals the existence of a non-affected region with the initial microstructure prior to the induction surface hardening process.

Now, comparisons are carried out between the strains and stresses in Fig 4.34 and that in Fig 4.35. It is noted that all the strains and stresses profiles in Fig 4.35 have shifted up. The maximum compressive stress in Fig 4.34(b) is around -1000MPa whereas it is only -750MPa in Fig 4.35(b), approximately. Moreover, at the depth relatively far from the surface, the strains and stresses in Fig 4.35, which are based on the XRD-determined d_0, are almost zero, in contrast to the stress value of -250MPa in Fig 4.34(b). Clearly, the difference of the residual strains and stresses shown in between Fig 4.34 and 4.35 are resulting from using different stress-free lattice spacing d_0. Since the XRD-determined

two d_0 values (Fig 4.31) are relatively smaller than that determined by ND, the corresponding strain and stress profile shown in Fig 4.35 shift up compared with that in Fig 4.34, and display much closer to zero near the core. Hence, it could be guessed that, at the depth relatively far from the surface, the value of $d_{0\text{-}depth}$ (determined by XRD) may be more close to the real stress-free lattice spacing of the sample. However, in spite of this, all analysis based on Fig 4.35 is only aimed at giving a comparison of the strains and stresses determined by different d_0 to that determined by present ND measurement. The curves shown in Fig 4.35 cannot be used as the residual stress result of present work.

In summary, for the induction hardened sample (e.g. disc #7 is present study), the knowledge of d_0 depth distribution is necessary. This is because the d_0 in the hardened layer can show a relatively larger size than that in the core material, which may finally affect the stress calculation to a considerable extent. For example, in present ND study, the variation of 0.001Å in d_0 can result in a difference in residual stress more than 200MPa in the hardened layer. However, the reliability and accuracy of the ND-based d_0 measurement itself is still more or less under question, since the supposed stress-free sample (the comb in present study) may be not completely stress-free. This is an issue left in present ND work and needed to be fully studied in the future.

4.3.3.3 Full Width Half Maximum (FWHM) results

The FWHM profile of the Fe *{112}* $K\alpha_1$ diffraction peak is illustrated in Fig 4.36. The relevant hardness curve is also shown in Fig 4.36 for giving a clear explanation. As seen, the overall FWHM profile in the hoop, axial and radial directions are quite similar. The only noticeable difference in peak width among them appears within the hardened layer. Regarding the transition zone and core material region, the three FWHM curves are very close to each other even overlapping at many radial positions. Besides, all the three FWHM profiles display a visible variation in the hardened region up to a radial depth around 1.0mm below the surface, and such variations could be related to the likewise hardness fluctuation in surface hardened region, suggesting the inhomogeneous microstructure generated in the surface layer, possibly caused by the dislocations existed in the hardened layer.

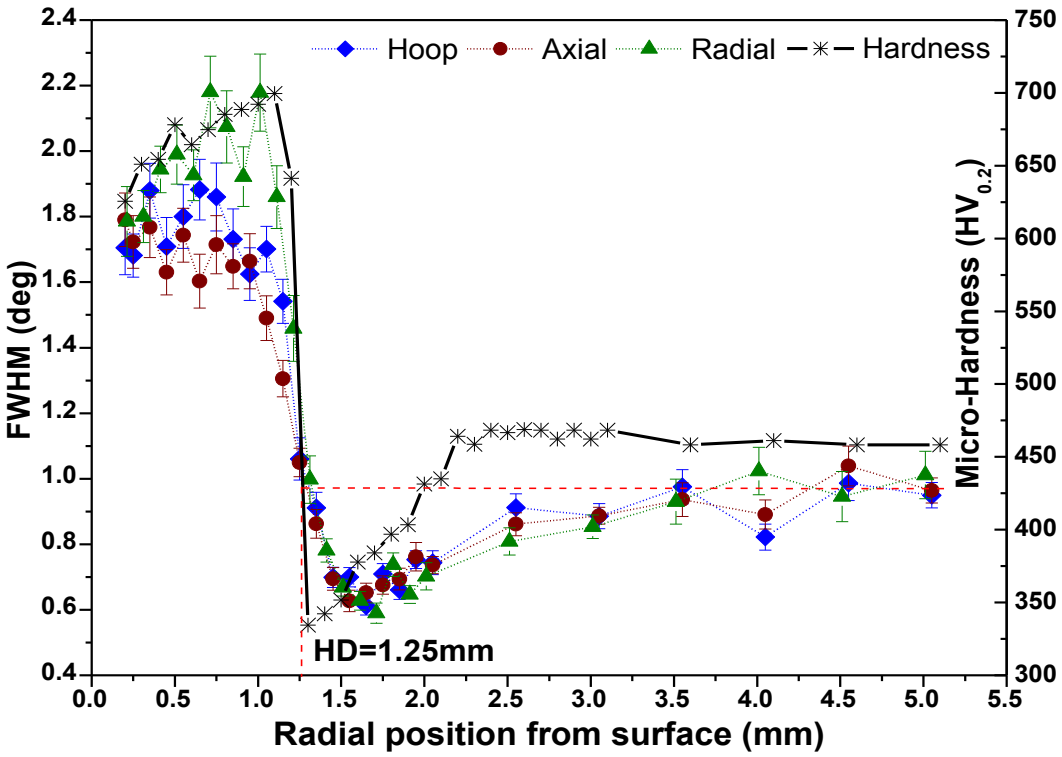

Fig 4.36 Fe *{112}* diffraction peak FWHM distributions along radius

Moreover, after the hardened region, the peak width declines quickly towards the center until reaching a minimum value around 0.6 degree at a radial depth of 1.5mm approximately. This is closely followed by a gradual increase to approach a nearly constant value of 1.0 degree, revealing the core material zone. The remarkable trough appeared in the FWHM curve is consistent with the similar groove pattern found in the hardness profile (Fig 4.28 and 4.29), which could be seen as the material over-tempering nature taking place at the end of the hardened region.

CHAPTER 5

Concluding Remarks, Contributions and Suggestions for Future Work

5.1 Concluding Remarks

The results show that with the same initial hardness, the disc which is induction hardened using longer heating times and higher input powers can finally generate deeper hardening depth and larger distortions. This indicates that IH parameters can significantly affect the distortion outcomes. Increasing heating time or power increases the distortion size. Meanwhile, based on the comparison among discs with different initial hardness but encountering the same IH recipe, it can be concluded that the initial hardness can as well influence the hardening depth and final distortion results. Discs with lower initial hardness demonstrate a smaller hardening depth and greater distortion magnitude, which raises the apparent contradiction.

In addition, a two-dimensional schematic disc distortion contour has been constructed. It displays a general symmetric distortion profile with a convex-shape pattern near the outer edge while gradually approaches zero towards the center of the disc's top and bottom faces. The extension and size of this distortion pattern of each disc sample are related to

the applied IH recipe. Besides, for the circumferential face there is no specific distortion shape tendency that can change according to the experimental conclusions: a convex-shape can be always observed from the samples with higher initial hardness, where the apex is located around the disc mid-thickness. Considering the discs with lower initial hardness, however, an irregular distortion profile on the circumferential face was usually observed.

For the same initial hardness, hardening depth supports the distortion results. The larger distortion is always accompanied with a greater hardening depth. However, when probing the effect of sample initial hardness for a given recipe, an opposite conclusion is drawn: larger distortions are related to smaller hardened case. This can be attributed to the increase of Martensite transformation temperature with decreasing the initial hardness.

The d_0 radial and hoop results both indicate a relatively large value near the disc surface, within the transformed zone. A smaller and constant d_0 is measured towards the core. The hoop residual stress distribution along the disc radius displays a compressive value near the surface changing into tensile at approximately the transition zone, followed by a nearly constant value in the core material. This is quite normal for induction hardened steel due to the martensitic transformation happening in the hardened layer. The disc residual stress profile in axial direction is similar to that in the hoop direction in the area near the surface and shows the same constant value in the core, except that it only has a very small tensile stress region. With respect to radial residual stress, however, it is

always compressive and demonstrates a relatively large variation along the radius but also shows the same constant value in the core material as that of the hoop and axial directions.

Since the uncertainty of residual stress measured by ND is relatively large due to the larger sampling gauge volume compared with XRD, especially in the near surface area due to the heterogeneous microstructure of the newly-formed Martensite, the noticeable variation of the disc radial residual stress is unreliable to some extent. Therefore, for sample near surface residual stress investigation, XRD technique is considered as an alternative choice instead of ND. However, for deeper stress measurement by XRD, since a series of layer removal process is required and its corresponding stress relaxation correction may also cause significant errors, the reliability of stress data obtained by XRD is also under question. Accordingly, other methods, such as the contour approach, are suggested to probe the residual stress in depth to validate the ND-based stress result in present study.

The over-tempered zone located between the hardened and core region. This kind of hardness profile has been further documented by the FWHM distributions obtained by ND which also demonstrated a groove-shape at the same depth range. Furthermore, the mid-thickness hardness profile and the relevant residual stress distribution are in good agreement. The hoop residual stress transformed from compressive to tensile in the same hardness transition region. Interestingly, hardness displays a constant value after 2.5mm

from the surface until the core whereas the residual stress seems to level off at deeper values. Relating this to the corresponding distortion profile, it has been noted that the distortion magnitude also gradually approaches zero after 2 or 3mm away from the edge of the disc.

5.2 Contributions

A coordinate measuring machine (CMM) and the neutron diffraction (ND) technique are employed in present work to characterize the distortion pattern and the residual stress distribution of the induction hardened discs. The contributions of this work can be summarized as:

- The relationship between the IH parameters (time and power) applied to discs and the resulting distortion size as well as the hardening depth has been established.
- The influence of the initial hardness of the discs on the IH distortion size and the hardening depth has been found.
- 3-dimensional residual stress distribution in depth of the induction hardened disc has been documented by non-destructive ND method.
- The relationship between the residual stress field and the corresponding hardness profile has been characterized.

5.3 Suggestions for Future Work

Based on the research performed in this thesis, the following issues are suggested for future work:

- Distortion Measurement

Since the distortion measurements carried out in present studies are all based on the touch-probe CMM technique, the sample surface could be more or less impacted by the touching movement which probably leads to increasing the uncertainty in the distortion measurements. Accordingly, it is better to use laser-scan CMM technique to study distortion.

In addition, as mentioned in the distortion result of Chapter IV, the paradox effect of initial hardness on the distortion results is worthy to be further studied. This could be based on a series of distortion measurements on different samples with various initial hardness levels.

- Residual Stress Measurement

ND method is applied for disc sample residual stress investigation at the depth from 0.2mm to 5mm, but for the near-surface stress distribution within 0.2mm from the surface, there is no data. Therefore, XRD technique is recommended to investigate the residual stress distribution within 0.2mm. This should be combined with the ND result to uncover the entire residual stress profile.

Moreover, considering only one disc sample was examined by ND in this study, the relationship between the residual stress and various applied IH recipes were not established. Hence, more hardened disc specimens with different IH parameters should be further investigated by ND in the future work.

- Other method to investigate RS

Destructive methods, for example the contour method could be used on the same disc to compare with the non-destructive ND approach.

- Modeling of IH

Complete IH process modeling is needed and the obtained ND residual stress result can be applied to validate the effectiveness of this simulation works.

- Improvement of the RS determination by ND technique

Firstly, for improving the RS measurement by ND, more accurate and reliable stress-free lattice spacing (d_0) values are needed. This, on the one hand, requires an appropriate manufacturing process for the reference sample. In the present study, the wire-EDM machining is employed for reference sample (comb) preparation. However, a slight bend and deflection appeared on the comb teeth, which could be a source of error of the residual stress result. Therefore, an alternative technique should be selected carefully to avoid or at least reduce the machining effect on reference sample to a large extent. Besides, on the other hand, the accuracy of the d_0 measurement is also expected to be

improved. This could be achieved by increasing the neutron counting time or by adjusting the sampling gauge volume to obtain a better diffraction peak with lower background, for example.

Secondly, a successful residual stress determination also depends on the accuracy of the stressed lattice spacing (d) measurement. As mentioned in the present ND study, the double-peak (overlapped peaks) diffraction pattern appeared at the near surface area of the disc sample is treated as the single peak, which can be a source of error. Therefore, one improvement can be made to figure out the precise center location of the double-peak diffraction pattern.

Furthermore, the ND equipment set-up prior to the experiment also affects the residual stress result. However, since the sample positioning and the apparatus alignment of the present ND experiment have been proved to be good enough, the significant improvement of the stress measurement cannot be expected only by improving the equipment set-up.

In addition to above, the characters of the investigated sample itself such as the grain size, the texture, the plastic anisotropy and the inhomogeneous attenuation [27, 28] are all capable to influence the stress outcomes obtained by ND. Nevertheless, these factors are material-dependent and therefore hardly to be controlled to improve the accuracy of stress measurement.

References

[1] R.E. Haimbaugh, *Practical Induction Heat Treating*. Materials Park, OH: ASM International, 2001, pp. 5-18.

[2] J.R. Davis, Ed., *Surface Hardening of Steels: Understanding the basics*. Material Park, OH: ASM International, 2002, pp. 242-263.

[3] T.V. Rajan, C.P. Sharma, and A. Sharma, *Heat Treatment: Priciples and Techniques,* 2nd ed., New Delhi: PHI Learning Private Limited, 2011, pp. 145-153.

[4] R.E. Haimbaugh, *Practical Induction Heat Treating*. Materials Park, OH: ASM International, 2001, pp. 183-214.

[5] J. Grum, "A review of the influence of grinding conditions on resulting residual stresses after induction hardening and grinding," *J. Mater. Process. Technol.*, vol. 114, 2001, pp. 212-226.

[6] K.E. Thelning, *Steel and its Heat Treatment: Bofors Handbook*. London: Butterworth, 1975, pp. 432–451.

[7] P.J. Withers and H.K.D.H. Bhadeshia, "Overview residual stress Part 1-measurement techniques," *Mater. Sci. Technol.*, vol. 17, 2001, pp. 355-365.

[8] F.A. Kandil, J.D. Lord, A.T. Fry, and P.V. Grant, "A review of residual stress measurement methods," *Measurement of Residual Stress in Components*, NPL Report, UK, Feb. 2002.

[9] J. Lu and SEM Inc., *Handbook of Measurement of Residual Stresses*. NJ: Pearson Prentice Hall, 1997.

[10] Y.F. Kudryavtsev, "Residual stress," in *Springer Handbook of Experimental Solid Mechanics*, W.N. Sharpe Jr., Ed. NY: Springer Science+Bussiness Media, 2008, pp. 371-386.

[11] C. Ruud, "Measurement of residual stresses," in *Handbook of Residual Stress and Deformation of Steel*, G.E. Totten, M.A.H. Howes, and T. Inoue, Eds. Materials Park, OH: ASM International, 2002, pp. 99-117.

[12] G.S. Schajer, "Destructive methods for measuring residual stresses: Techniques and opportunities," in *Experimental and Applied Mechanics: Proc. SEM Annual Conf.*, T. Proulx, Ed. NY: Springer, 2011, pp. 220-231.

[13] J. Mathar, "Determination of initial stresses by measuring the deformation around drilled holes," *Trans. ASME,* vol. 56, no. 4, 1934, pp. 249-254.

[14] J. Lu and J. F. Flavenot, "Application of the incremental hole-drilling method for the measurement of residual stress distribution in shot-peened components," in *Shot Peening: Science Technology Application (the 3rd int. conf. on shot peening),* Frankfurt am Main, Germany: DGM, 1987, pp. 279–288.

[15] E. Procter and E. M. Beaney, “The Trepan or Ring Core Method, Centre-Hole Method, Sach’s Method, Blind Hole Methods, Deep Hole Technique,” 1987, http://www.shotpeener.com/library/pdf/1987123.pdf
[16] W. Soete and R. Vancrombrugge, “An industrial method for the determination of residual stresses,” *Proc. SESA*, vol. 8, no. 1, 1950, pp. 17-28.
[17] R. G. Boiten and W. Ten Cate, “A routine method for the measurement of residual stresses in plates,” *Appl. Sci. Res.,* vol. 3, 1952, pp. 313-343.
[18] M. B. Prime, "The contour method: A new approach in experimental mechanics," in *Proc. SEM Annual Conf.,* June 2009.
[19] M. B. Prime and A. R. Gonzales, "The contour method: simple 2-D mapping of residual stresses," in *Proc. 6th Int. Conf. on Residual Stresses*, Oxford, U.K., July 2000, pp. 617-624.
[20] C.O. Ruud, “A review of selected non-destructive methods for residual stress measurement,” *NDT International*, vol. 15, Feb. 1982, pp. 15-23.
[21] I.C. Noyan and J.B. Cohen, *Residual Stress Measurement by Diffraction and Interpretation*. NY: Springer-Verlag, 1987.
[22] S.F. Silva Jr., “Determining residual stresses in ferromagnetic materials by barkhausen effect,” M.A. thesis, UFMG, Belo Horizonte, Brazil, 1998.
[23] Y.F. Kudryavtsev, J. Kleiman, and O. Gushcha, “Residual stress measurement in welded elements by ultrasonic method,” in *9th Int. Congress on Experimental Mechanics,* 2000, pp. 954-957.
[24] M.E. Hilley, Ed.,“Residual stress measurement by X-ray diffraction,” *SAE*, vol. 784, 1971, pp. 21-24.
[25] G.A. Webster, “Role of neutron diffraction in engineering stress analysis,” in *Measurement of Residual and Applied Stress Using Neutron Diffraction,* vol. 216, NATO ASI Series E, M.T. Hutchings and A.D. Krawitz, Eds., Dordrecht, Netherlands: Kluwer Academic Publishers, 1992, pp. 21-36.
[26] M.G. Moore and W.P. Ewans, “Mathematical correction for stress in removed layers in X-ray diffraction residual stress analysis,” *SAE Trans.*, vol. 66, 1958, pp. 340.
[27] A. Allen, M. Hutchings, and C. Windsor, “Neutron diffraction methods for the study of residual stress fields,” *Adv. Phys.*, vol. 34, 1985, pp. 445–473.
[28] M.T. Hutchings, P.J. Withers, T.M. Holden, and T. Lorentzen, *Introduction to the Characterization of Residual Stress by Neutron Diffraction.* Boca Raton, FL: Taylor & Francis, 2005.
[29] O. Kirstein, V. Luzin, A. Brule, H. Nguyen, and D. Tawfik, “Kowari-OPAL’s residual-stress diffractometer and its application to materials science and engineering,” *Advanced Materials Research*, vols. 41-42, 2008, pp. 439-444.
[30] A.K. Bewoor and V.A. Kulkarni, *Metrology & Measurement*. New Delhi: McGraw-Hill, 2009, pp. 367-384.

[31] K.A. Young, "Machining-induced residual stress and distortion of thin parts," Ph.D. dissertation, Washington University, Saint Louis, MO, May 2005.
[32] H.J. Yu, "Berechnung von Abkuehlungs-, Umwandlungs-, Schweiss- sowie Verformungseigenspannungen mit Hilfe der method der Finiten Elemente," PhD thesis, University Karlsruhe, Karlsruhe, Germany, 1977, cited in J. Rohde and A. Jeppsson, "Literature review of heat treatment simulations with respect to phase transformation, residual stresses and distortion," *Scand. J. Metall.*, vol. 29, 2000, pp. 47-62.
[33] K.F. Wang, S. Chandrasekar, and H.T.Y. Yang, "Finite-element simulation of induction heat treatment," *J. Mater. Eng. Perform.*, vol. 1, no. 1, pp. 97-112.
[34] S. Denis, M. Zandona, A. Mey, and S.A. Boufoussi, "Calculation of internal stresses during surface heat treatment of steels," in *Proc. European Conf. on Residual Stresses,* V. Hauk, H.P. Hougardy, E. Macherauch, and H.D. Tietz, Eds., (Frankfurt, Germany), 1992, DEM Informationsgesselschaft mbH, Oberursel, 1993, pp. 1011-1020.
[35] O. Longeot and C. Delalean, "Simulation numerique des procedes de traitement par induction," *Traitement Thermique*, 1995, pp. 33-47.
[36] Y.S. Yang and S.J. Na**, "**Effect of transformation plasticity on residual stress fields in laser surface hardening treatment," *J. Heat Treat.,* vol. 9, 1991, pp. 49-56.
[37] G.A. Mesmer, Arch. Elsenhuttenwesen, vol. 10, 1936, pp. 59, cited in C.N. Hu, "Recent developments achieved in China about the center hole relaxation technique for residual stress measurement," *Strain*, vol. 22, 1986, pp. 119-126.
[38] R.A. Kelsey, "Measuring non-uniform residual stresses by the hole drilling method," *Proc. SESA*, vol. 14, no. 1, 1956, pp. 181.
[39] E.M. Beaney and E. Procter, "A critical valuation of the centre hole technique for the measurement of residual stress," *Strain*, vol. 10*,* no. 1, 1974, pp. 7-14.
[40] E.M. Beaney, "Accurate measurement of residual stress on any steel using the centre hole method," *Strain*, vol. 12, no. 3, 1976, pp. 99-106.
[41] B.P. Gupta, "Hole-drilling technique: modification in the analysis of residual stress," *Experimental Mechanics*, vol. 13, 1973, pp. 23-27.
[42] S. Redner and C.C. Perry, "Factors affecting the accuracy of residual stress measurements using the blind hole drilling method," in *Proc. 7th Int. Conf. on Experimental Stress Analysis*, 1982, pp. 604-616.
[43] H. Zhou and M.D. Rao, "On the error analysis of residual stress measurements by the hole-drilling method," *J. Strain Anal. Eng. Des.,* vol. 28, no. 4, 1993, pp. 273-276.
[44] P. Barsanescu and P. Carlescu, "Correction of errors introduced by hole eccentricity in residual stress measurement by the hole-drilling strain-gage method," *Measurement*, vol. 42, no. 3, 2009, pp. 474-477.
[45] L. Mordfin, *Mechanical Relaxation of Residual Stresses*. Baltimore: ASTM, 1988.

[46] P.J. Withers, M. Turski, L. Edwards, P.J. Bouchard, and D.J. Buttle, "Recent advances in residual stress measurement," *Int. J. Pressure Vessels and Piping*, vol. 85, 2008, pp. 118-127.
[47] M.B. Prime, R.J. Sebring, J.M. Edwards, D.J. Hughes, and P.J. Webster, "Laser surface-contouring and spline data-smoothing for residual stress measurement," *Experimental Mechanics*, vol. 44, no.2, 2004, pp. 176-184.
[48] M.B. Prime, "Cross-sectional mapping of residual stresses by measuring the surface contour after a cut,"*J. Eng. Mater. Tech.*, vol. 123, 2001, pp. 162-168.
[49] M.B. Prime, et al., "Residual stress measurements in a thick, dissimilar aluminum alloy friction stir weld," *Acta Mater.*, vol. 54, 2006, pp. 4013-4021.
[50] Y. Zhang, M.E. Fitzpatrick, and L. Edwards, "Measurement of the residual stresses around a cold expanded hole in an EN8 steel plate using the contour method," *Mater. Sci. Forum*, vols. 404-407, 2002, pp. 527-532.
[51] D.W. Brown, et al., "Critical comparison of two independent measurements of residual stress in an electron-beam welded uranium cylinder: neutron diffraction and the contour method," *Acta Mater.*, vol. 59, no. 3, 2011, pp. 864-873.
[52] P. Pagliaro, M.B. Prime, H. Swenson, and B. Zuccarello, "Measuring multiple residual-stress components using the contour method and multiple cuts," *Experimental Mechanics*, vol. 50, no. 2, 2010, pp. 187-194.
[53] M. Kartal, et al., "Residual stress measurements in single and multi-pass groove weld specimens using neutron diffraction and the contour method," *Mater. Sci. Forum*, vols. 524-525, 2006, pp. 671-676.
[54] D.J. Hornbach, P.S. Prevey, and P.W. Mason, "X-ray diffraction characterization of the residual stress and hardness distributions in induction hardened gears," in *Proc. of the 1st Int. Conf. on Induction Hardened Gears and Critical Components*, Indianapolis, IN, Gear Research Institute, May 1995, pp. 69-76.
[55] D. Coupard, T. Palin-luc, P. Bristiel, V. Ji, and C. Dumas, "Residual stresses in surface induction hardening of steels: Comparison between experiment and simulation," *Mater. Sci. Eng., A*, 2008, pp. 328-339.
[56] C. Balasingh and A.K. Singh, "Residual stresses and their measurements by X-ray diffraction methods," *Met. Mater. Proc.*, vol. 12, no. 2-3, 2000, pp. 269-280.
[57] C.H. Gür, A.E. Tekkaya, and T. Ozturk, "Numerical and experimental investigation of quench process," *in Proc. 2nd Int. Conf. on Quenching and Control of Distortion*, Cleveland, OH, Nov. 1996, pp. 305–314.
[58] R. Schröder, "Influences on development of thermal and residual stresses in quenched steel cylinders of different dimensions," *Mater. Sci. Technol.* vol. 1, 1985, pp. 754-764.

[59] S. Hossain, M.R. Daymond, C.E. Truman, and D.J. Smith, "Prediction and measurement of residual stresses in quenched stainless-steel spheres," *Mater. Sci. Eng., A*, vol. 373, 2004, pp. 339-349.
[60] V. Marthandam, "Metallurgical characterization and residual stress measurement of target structural materials," M.S. thesis, University of Nevada, Las Vegas, Aug. 2004.
[61] G. Albertini, et al., "Neutron diffraction measurements for the determination of heat treatment effectiveness in generating compressive residual stress in an automotive crown gear," *Physica B,* vols. 276-278, 2000, pp. 925-926.
[62] A. Paradowska, T.R. Finlayson, J.W.H. Price, R. Ibrahim, A. Steuwer, and M. Ripley, "Investigation of reference samples for residual strain measurements in a welded specimen by neutron and synchrotron X-ray diffraction," *Physica B*, vols. 385-386, 2006, pp. 904-907.
[63] A.N. Ezeilo, G.A. Webster, P.J. Webster, M. Roth, and W.J. Muster, "Comparison of X-ray and neutron diffraction determinations of residual stresses in a laser treated martensitic steel," in *Proc. 2nd European Conf. on Adv. Materials and Processes* (T.W. Clyne and P.J. Withers, Eds.), Euromat 91, Cambridge, 1991, pp. 389-394.
[64] R. Ramanathan and R.P. Foley, "Effect of prior microstructure on Austenite decomposition and associated distortion," Illinois Institute of Technology, U.S.A., Aug. 2001.
[65] A. Thuvander, A. Melander, M. Lind, N. Lior, and F. Bark, "Prediction of convective heat transfer coefficients and examination of their effects on distortion of cylindrical tubes quenched by gas cooling," in *Proc. 4th ASM Heat Treatment and Surface Engineering Conf.*, Florence, Italy, 1998.
[66] A. Thuvander, "Calculation of distortion during case hardening of ring samples of steel DIN16MnCr5," Swedish Institute for Metals Research, Report IM.2671, 1990.
[67] E. Brinksmeler, J. Solter, and C. Grote, "Distortion engineering-Identification of causes for dimensional and form deviations of bearing rings," Annals of the CIRP, vol. 56, 2007, pp. 109-112.
[68] A.A. Deshpande, L. Xu, W. Sun, D.G. McCartney, and T.H. Hyde, "Finite-element-based parametric study on welding-induced distortion of TIG-welded stainless steel 304 sheets," *J. Strain Anal. Eng. Des.,* vol. 46, 2011, pp. 267-279.
[69] G. Ascanio, R. Nava, R. Trejo-Luna, and J. Rickards, "A method for measuring dimensional distortion in Ion-Nitrided steels," *Instrumentation and Development*, vol. 3, no. 5, 1995, pp. 21-24.
[70] Alloy Digest, Steel-Alloy Collection (ASM International 2002), "AISI-4340," Filing Code: SA-14, Feb. 1954.
[71] W-S. Lee and T-T. Su, "Mechanical properties and microstructural features of AISI 4340 high-strength alloy steel under quenched and tempered conditions," *J. Mater. Process. Technol.*, vol. 87, 1999, pp. 198-206.

[72] G. Blut, “Effet de la géométrie sur les paramètres du générateur et le profil de dureté lors d’une chauffe par induction : expérience et simulation,” M.Ing. thesis, Ecole de Technologie Superieure, Montreal, QC, Canada, 2010.
[73] N. Barka, A. Chebak, and J. Brousseau, “ Study of edge effect of 4340 steel specimen heated by induction process using Axi-symmetric simulation,” in *Proc. Progress In Electromagnetics Research Symposium*, Marrakesh, Morocco, Mar. 2011, pp. 1207-1203.
[74] K.H. Ho, S.T. Newman, S. Rahimifard, and R.D. Allen, “State of the art in wire electrical discharge machining (WEDM),” *Int. J. Mach. Tool Manufact.*, vol. 44, 2004, pp. 1247-1259.
[75] F. Xu, J.C. Fredette, R.A. Holt, R.B. Rogge, D. Pickard, and L. Tuck, “Investigation of residual stress in a bent Ti-clad Cu bus-bar by neutron diffraction and finite element modeling,” *Journal of Neutron Research*, vol. 15, no. 3-4, 2007, pp. 259-266.
[76] J.M. Moyer, and G.S. Ansell, “The volume expansion accompanying the Martensite transformation in Iron-Carbon alloys,” *Metall. Mater. Trans. A*, vol.6, 1975, pp. 1785-1791.
[77] C. Ducassy, F. Bridier, P. Bocher, and P. Arkinson, “Semi-empirical method to predict hardness during fast induction heating of a tempered martensitic AMS 6414 steel,” in *Proc. 48th Conf. of Metallurgists,* Sudbury, ON, Canada, 2009.
[78] C. Ducassy, “Prediction de la durete et de la profondeur de la zone de sur-revenu lors d'une chauffe rapide par induction d'un acier 4340 trempe revenu,” M.Ing. thesis, Ecole de Technologie Superieure, Montreal, QC, Canada, 2010.
[79] Database of X-ray machine BRUKER D8.
[80] T.V. Rajan, C.P. Sharma, and A. Sharma, *Heat Treatment: Priciples and Techniques,* 2nd ed., New Delhi: PHI Learning Private Limited, 2011, pp. 87-94.
[81] P.S. Prevey and P.W. Mason, “The use of X-ray diffraction to determine the triaxial stress state in cylindrical specimens,” in *Practical Application of Residual Stress Technology*, C. Ruud, Ed., Materials Park, OH: ASM, 1991, pp. 77-81.
[82] M. B. Prime, V. C. Prantil, P. Rangaswamy, and F. P. Garcia, “Residual stress measurement and prediction in a hardened steel ring,” *Mater. Sci. Forum*, vols. 347-349, 2000, pp. 223-228.
[83] G.E. Totten, N.I. Kobasko, and L.C.F. Canale, “Mechanism of surface compressive stress formation by intensive quenching,” *in MECOM 2005-VIII Congreso Argentino de Mecanica Computacional (A. Larreteguy, Ed.)*, Buenos Aires, Argentina, 2005, pp. 1041-1058.
[84] M.A. Wells, B.H-Morales, J.H. Root, and E.B. Hawbolt, “Neutron diffraction in the materials science toolbox,” *Physica B*, vols. 241-243, 1998, pp. 1274-1276.

[85] P.S. Prevey, “Problems with non-destructive surface X-ray diffraction residual stress measurement,” in *Practical Applications of Residual Stress Technology*, C. Ruud, Ed., Materials Park, OH: ASM, 1991, pp. 47-54.
[86] P.S. Prevey, “Current application of X-ray diffraction residual stress measurement,” in *Developments in Materials Characterization Technologies*, G. V. Voort and J. Friel, Eds., Materials Park, OH: ASM International, 1996, pp. 103-110.
[87] P.M.C.L. Pacheco, M.A. Savi, and A.F. Camarão, “Analysis of residual stresses generated by progressive induction hardening of steel cylinders,” *J. Strain Anal.*, vol. 36, no. 5, 2001, pp. 507-512.

Appendix I

SGV (sampling gauge volume) Determination

The SGV determination is important for ND stress measurement since the inappropriate SGV selection can result in a big error in stress result. The SGV dimensions chosen are generally based on two considerations: the stress scan step used and the sufficient grains involved in the SGV.

In present ND studies, the IH case depth (1.25mm) of disc sample is in between 1mm and 2mm and therefore the relatively smaller stress scan step of 0.2mm near the surface was used. The three principal directions for stress measurement are shown in Fig 1.

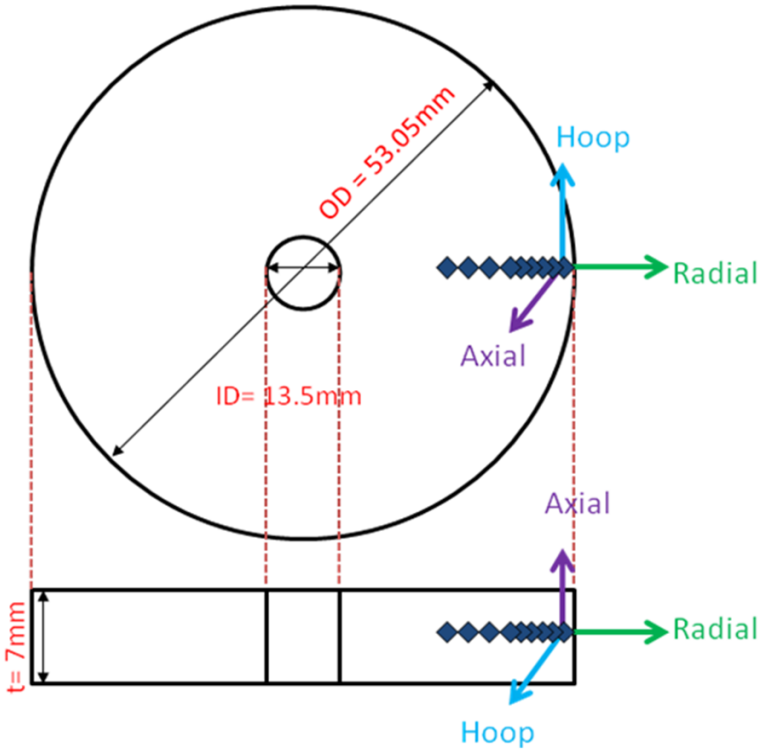

Fig 1 Three principal directions for stress measurement by ND

- **SGV determination in radial direction**

For disc radial residual strain investigation, the stress scan step is limited by the dimension of the two slits (incident and diffraction beam slits) used, as shown in Fig 2(a). Therefore, the wide of slit was decided as 0.3mm. Now, considering the requirement of sufficient grains covered in the SGV, the dimension of gauge height should not be too small. However, since the sample used in present study is disc sample, the increase of gauge height is accompanied with the increase of error. For example, as shown in Fig 3, the 10mm gauge height covers point A, D and C. However, the stress value at point A equals to that at point C but different from the one at point D. Therefore, the error comes from the stress difference between point A (same as C) and D, that is, BD. Clearly, the length of BD increases with the increasing of gauge height adapted. The calculation of such error (BD) based on different gauge height is summarized in the table of Fig 3.

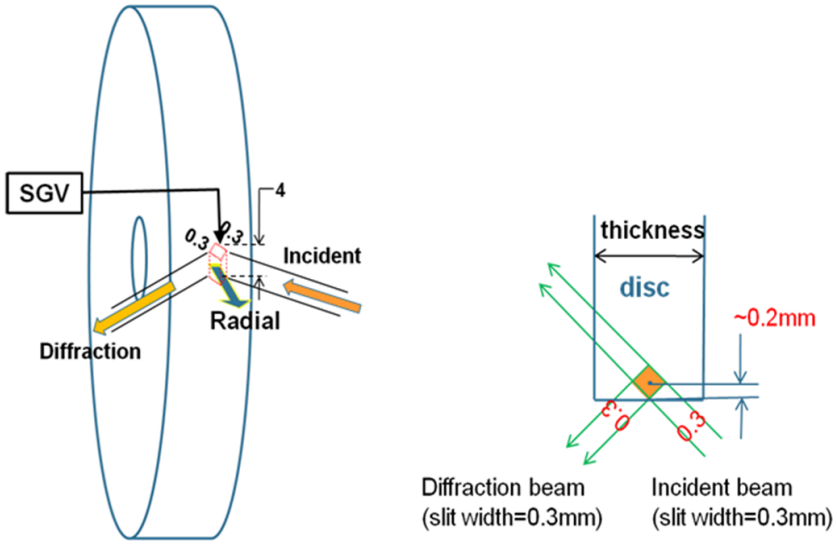

Fig 2 SGV determination in radial direction: (a) the SGV used for radial stress measurement; (b) the sampling area decided by two slits

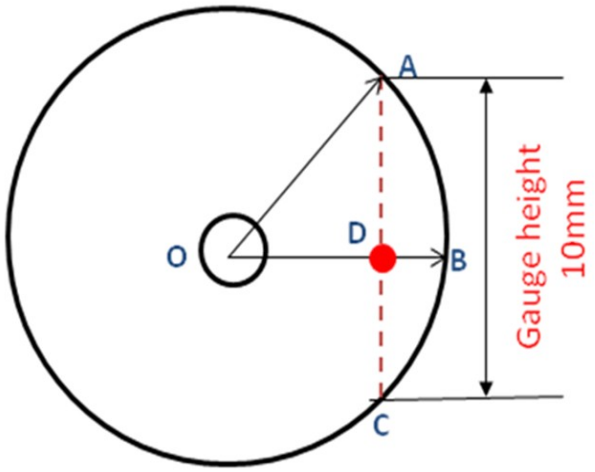

Gauge height (mm)	BD (μm)
10	236
9	191
8	151
7	116
6	85
5	56
4	38
3	21
2	9
1	2
0.3	0.2

Fig 3 Stress measurement error variation with different gauge height value

The finally gauge height used for radial direction is 4mm, with a relatively smaller error close to 40μm. This selection is because for those gauge heights smaller the 4mm, although the resulting measurement error is much smaller, the resulting SGV size is also very small. Too small SGV cannot include enough grains and therefore the diffraction signal will be weak.

Hence, based on all above, the SGV used in radial direction was determination by 0.3mm width of two slits with 4mm gauge height, was 0.36mm^3 (0.3×0.3×4).

- **SGV determination in hoop and axial directions**

For disc hoop and axial strain exploration, the stress scan step is limited by the dimension of the gauge height instead of slits in radial direction, as shown in Fig 4 and Fig 5.

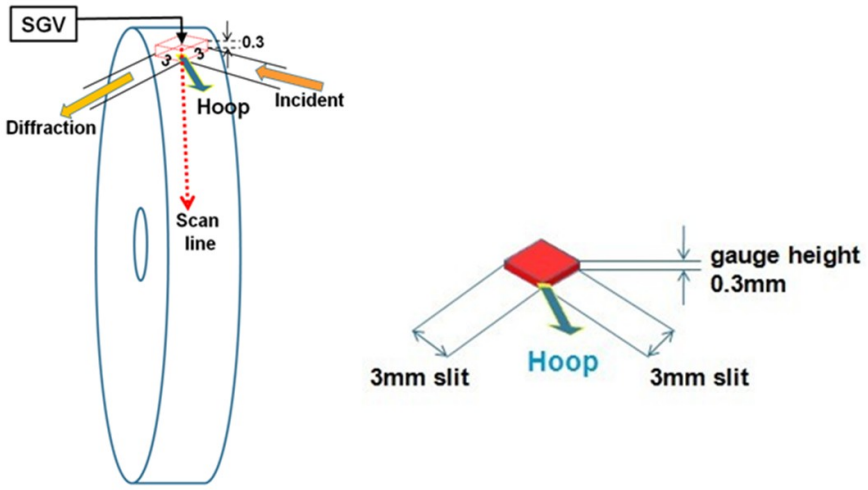

Fig 4 SGV determination in hoop direction

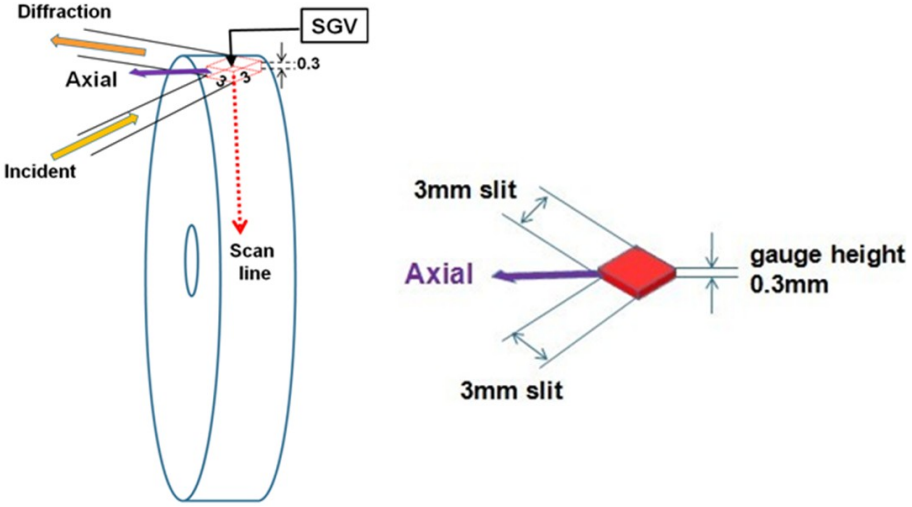

Fig 5 SGV determination in axial direction

Therefore, the gauge height in these two cases is chosen as 0.3mm. In comparison to the SGV determination in radial direction, the SGV dimensional error now is related to the wide of slits. Similarly as previous error analysis (see Fig 3), 3mm slits with relatively smaller error (4mm is also acceptable, but 3mm is enough to generate a larger SGV) was adopted for stress measurements.

Hence, the SGV dimensions for hoop and axial direction was determination by 3mm width of two slits with 0.3mm gauge height, was 2.7mm^3 (3×3×0.3).

Appendix II

IH Distortion Results of Three Testing Groups at Measuring Angles of: 90° (-X-axis), 180° (+Y-axis) and -90° (+X-axis)

- **Group I (disc #1 to #5 with initial hardness of 43HRC)**

1. At measuring angle of 90° (-X-axis):

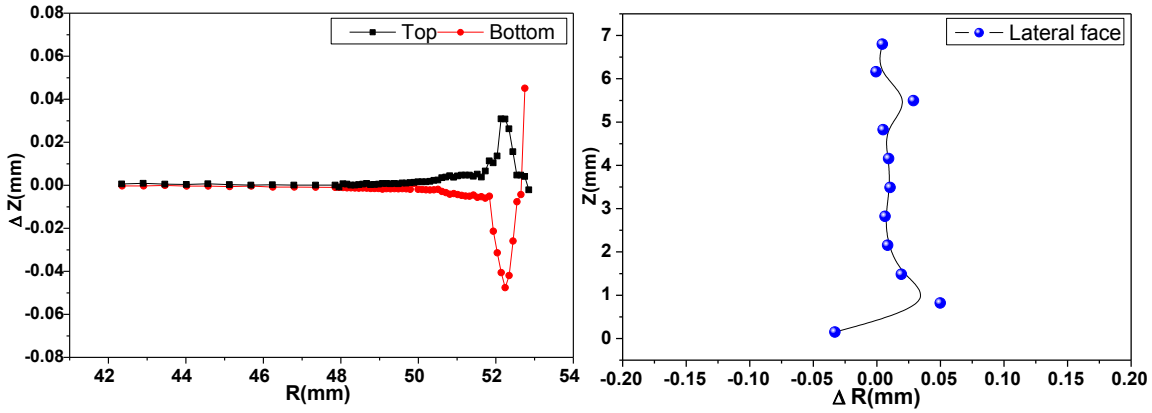

(a)

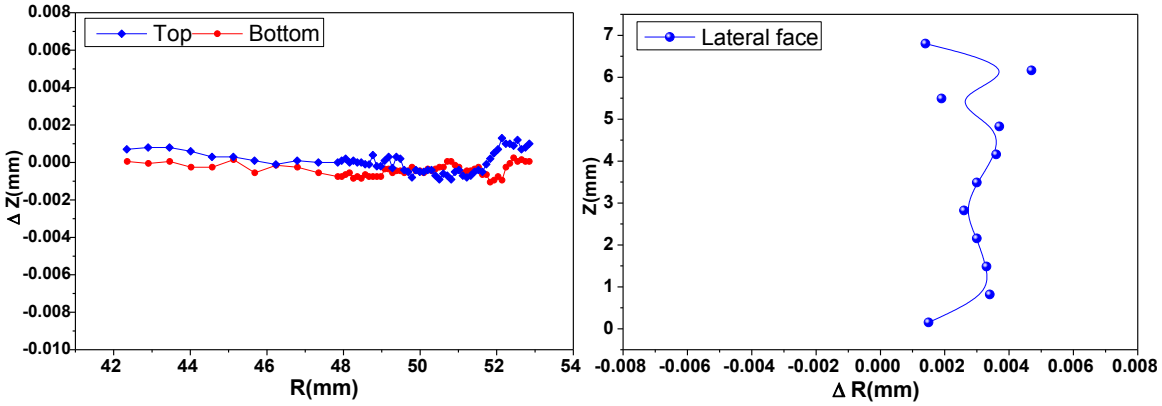

(b)

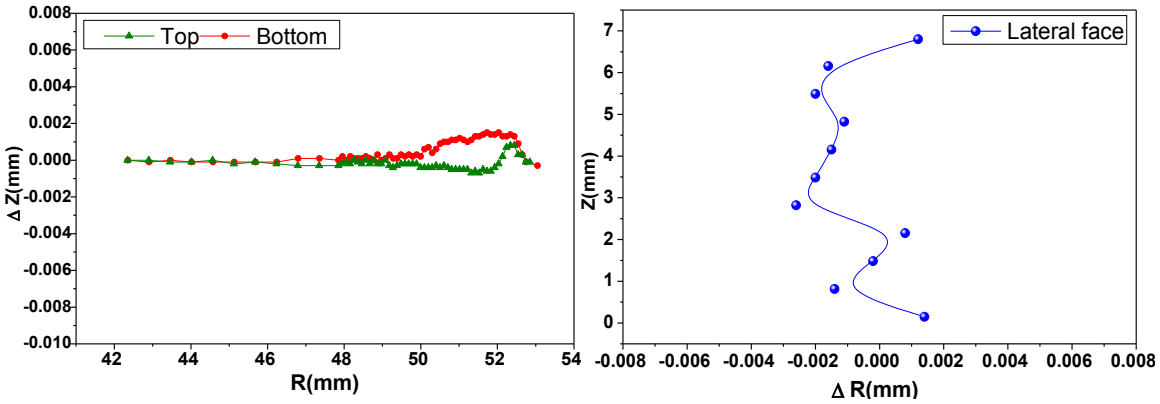

(c)

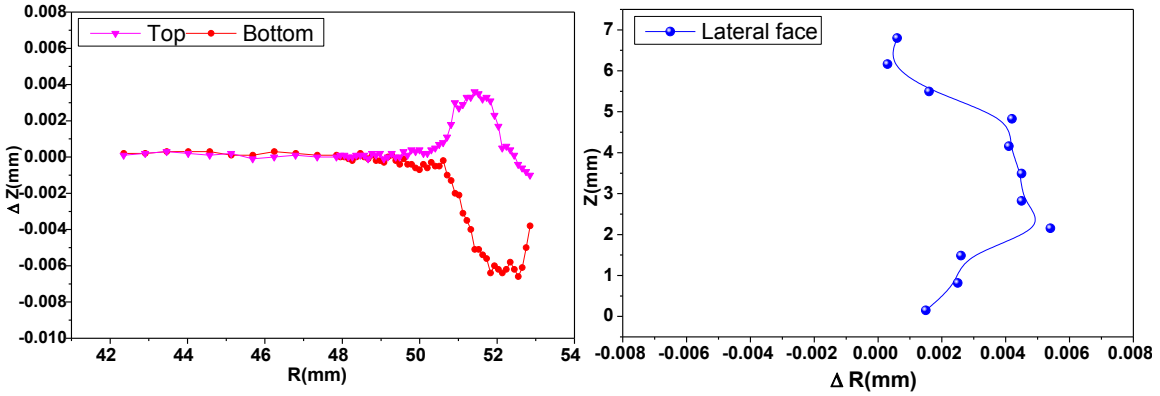

(d)

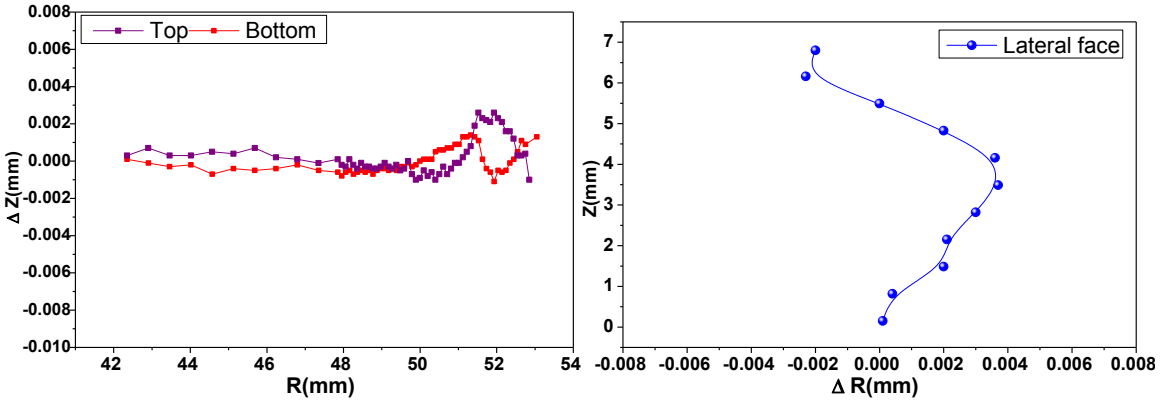

(e)

Fig 1 (a) to (e): axial (left) and radial (right) distortion profiles of disc #1 to #5 at measuring angle of 90˚

2. At measuring angle of 180˚ (+Y-axis):

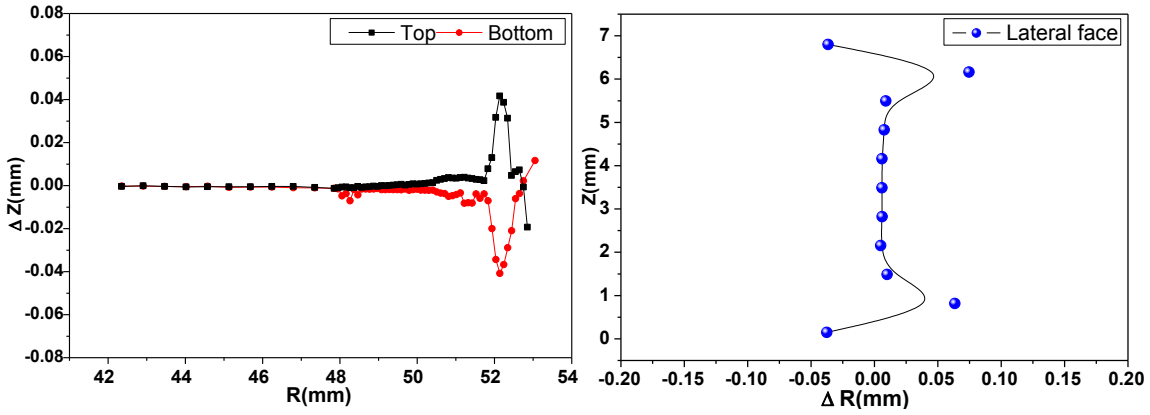

(a)

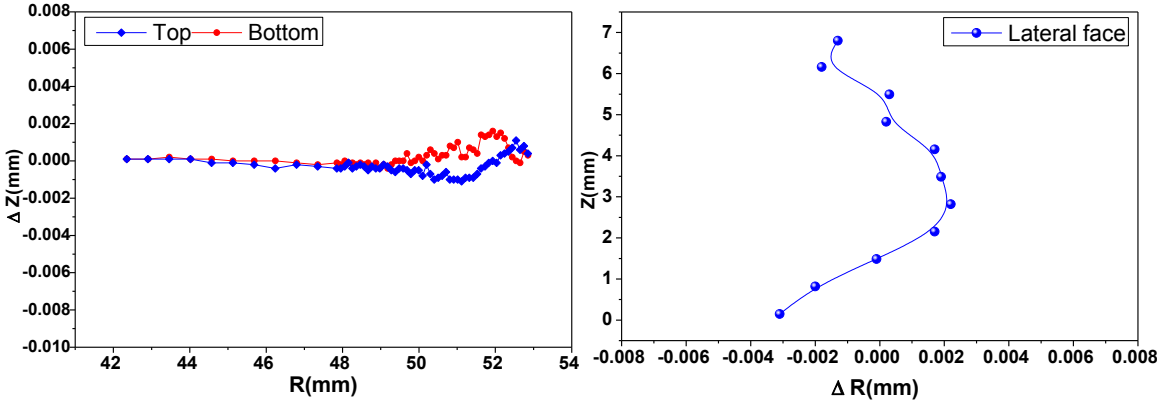

(b)

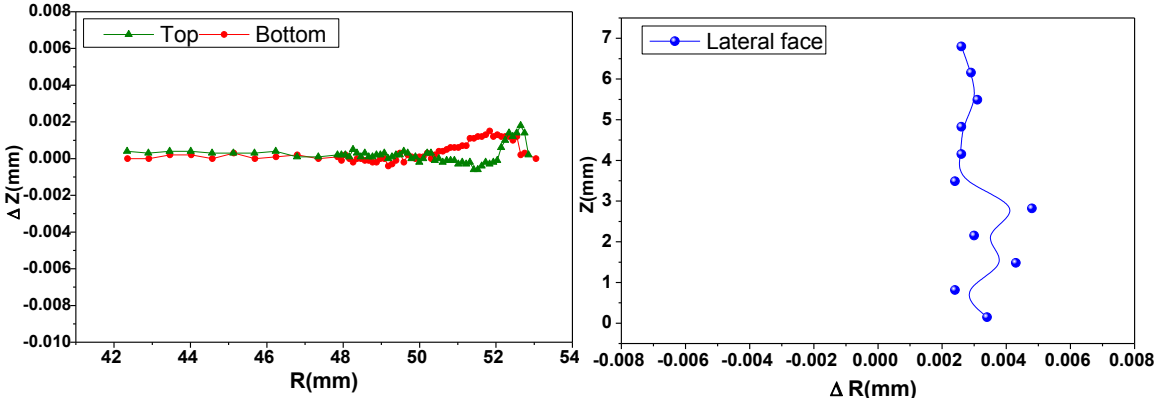

(c)

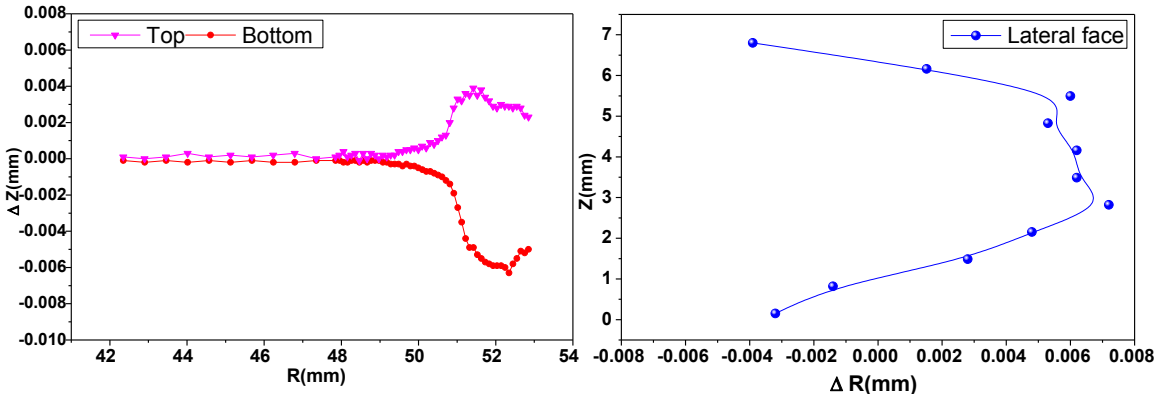

(d)

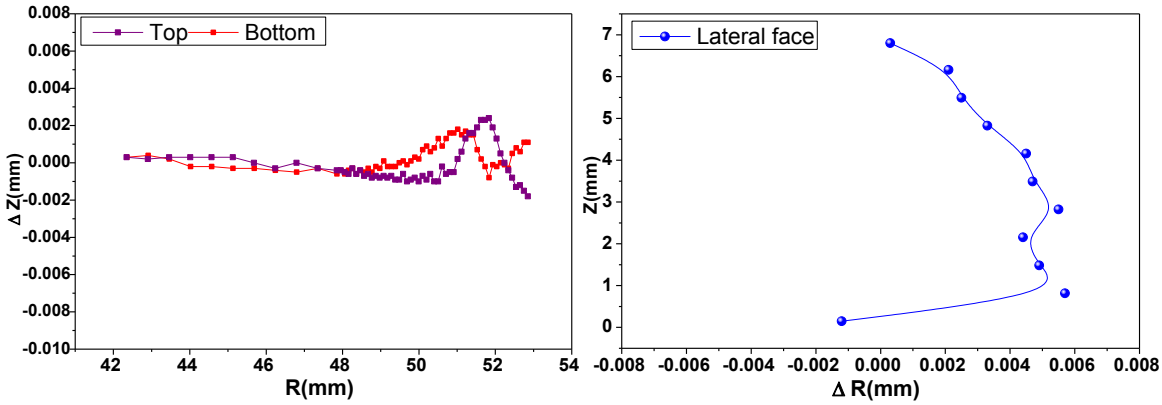

(e)

Fig 2 (a) to (e): axial (left) and radial (right) distortion profiles of disc #1 to #5 at measuring angle of 180˚

3. At measuring angle of -90˚ (+X-axis):

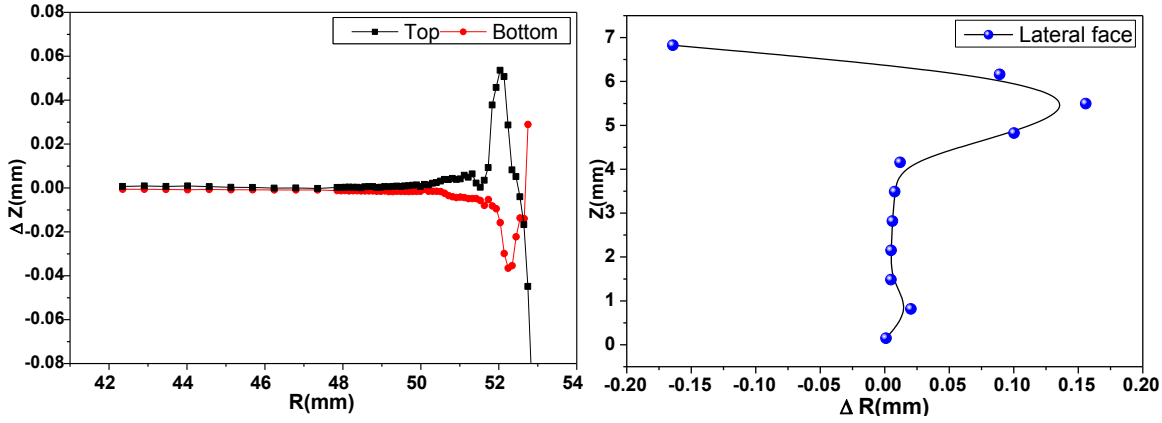

(a)

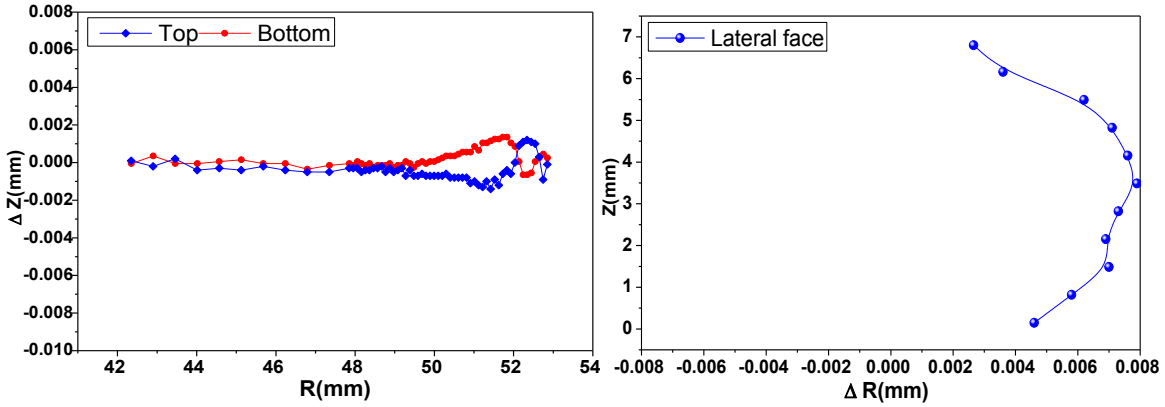
Top
Bottom
Δ Z(mm)
R(mm)
Lateral face
Z(mm)
Δ R(mm)

(b)

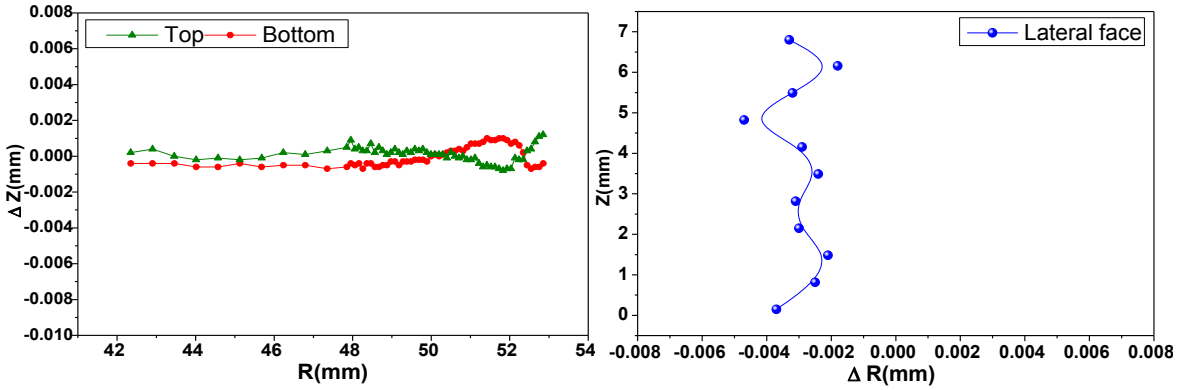
Top
Bottom
Δ Z(mm)
R(mm)
Lateral face
Z(mm)
Δ R(mm)

(c)

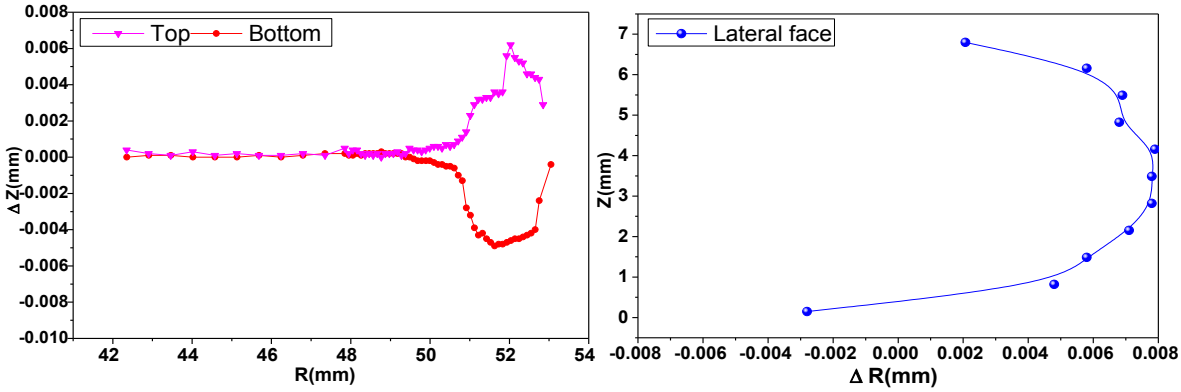
Top
Bottom
Δ Z(mm)
R(mm)
Lateral face
Z(mm)
Δ R(mm)

(d)

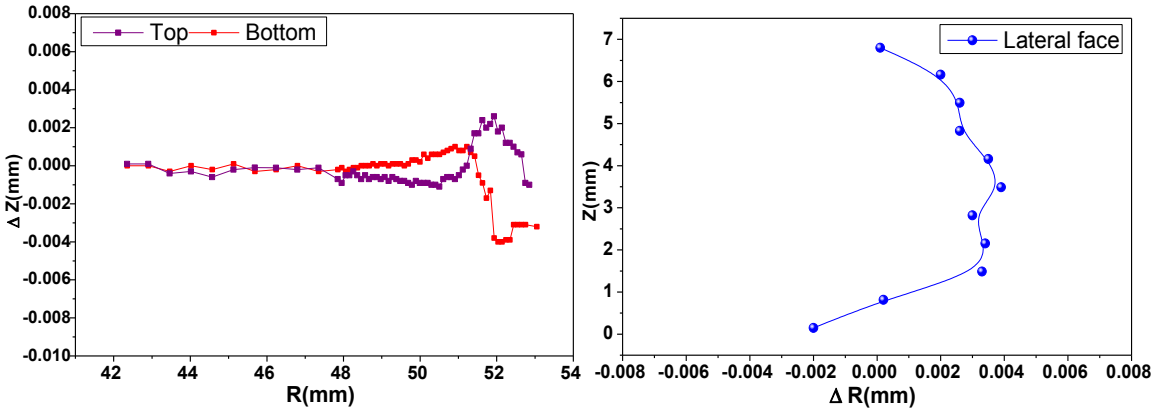

(e)

Fig 3 (a) to (e): axial (left) and radial (right) distortion profiles of disc #1 to #5 at measuring angle of -90˚

- **Group II (disc #11 to #15 with initial hardness of 35HRC)**

1. At measuring angle of 90˚ (-X-axis):

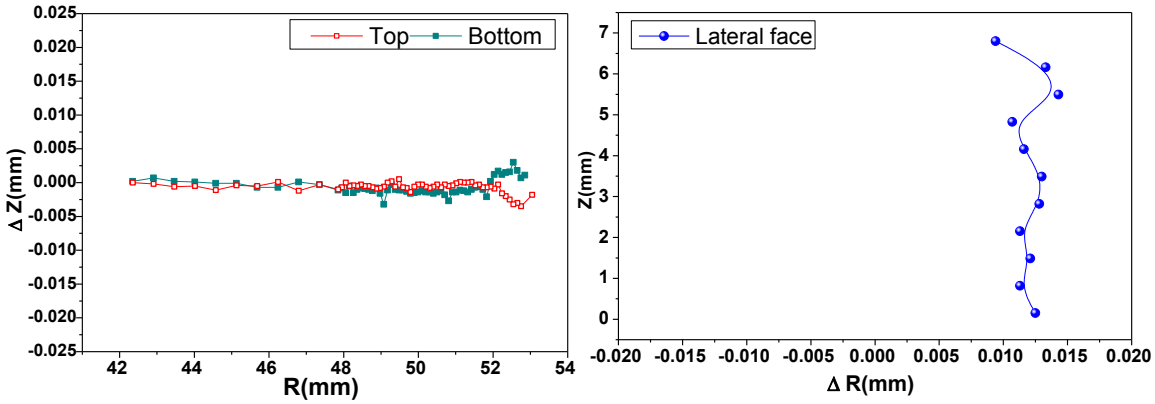

(a)

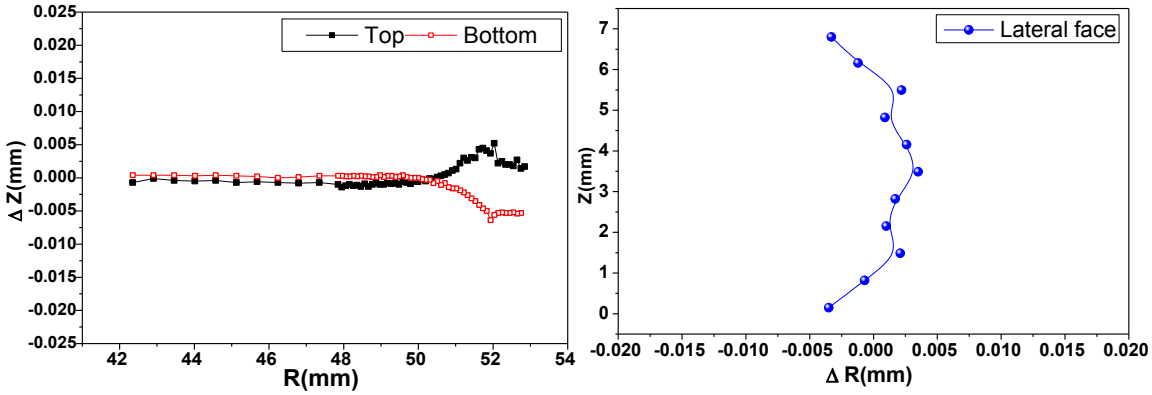
Top
Bottom
Δ Z(mm)
R(mm)
Lateral face
Z(mm)
Δ R(mm)

(b)

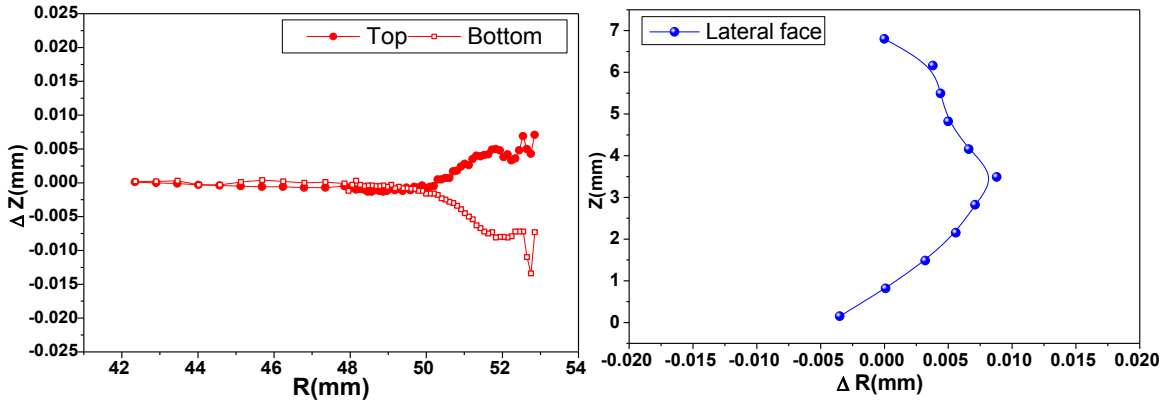
Top
Bottom
Δ Z(mm)
R(mm)
Lateral face
Z(mm)
Δ R(mm)

(c)

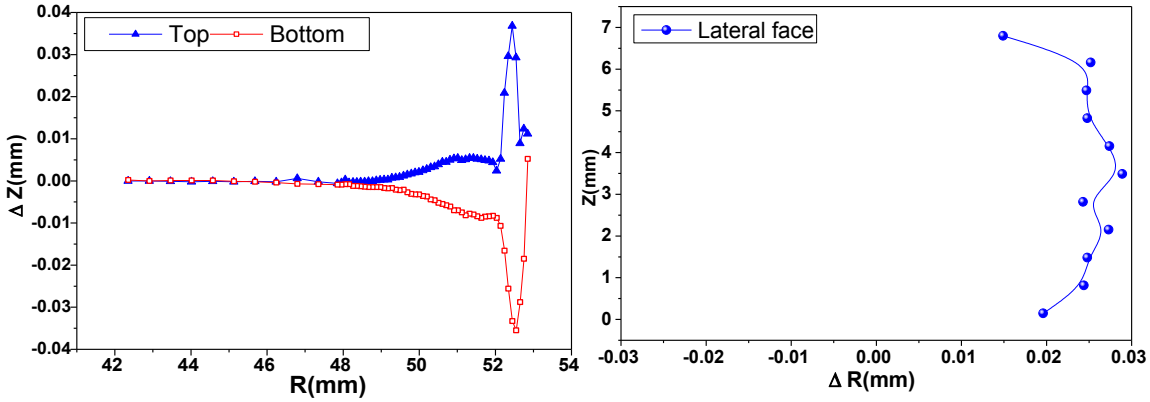
Top
Bottom
Δ Z(mm)
R(mm)
Lateral face
Z(mm)
Δ R(mm)

(d)

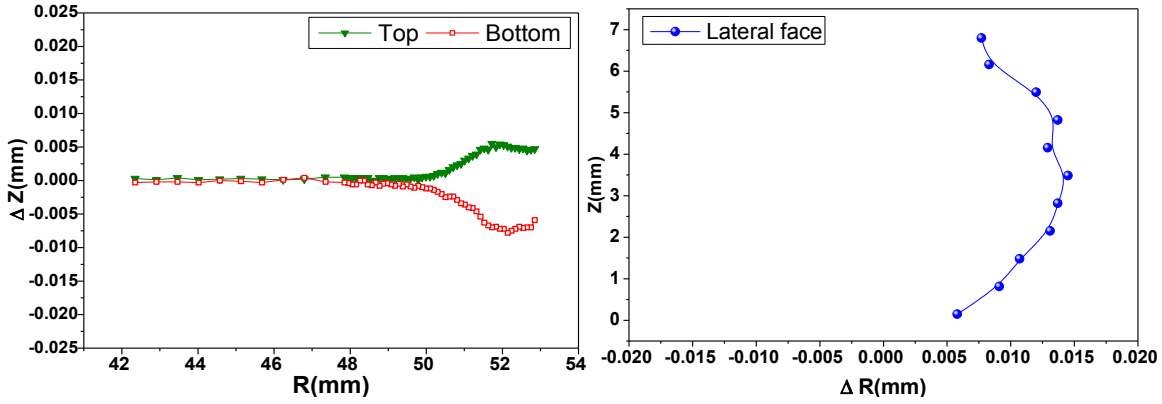

(e)

Fig 4 (a) to (e): axial (left) and radial (right) distortion profiles of disc #11 to #15 at measuring angle of 90˚

2. At measuring angle of 180˚ (+Y-axis):

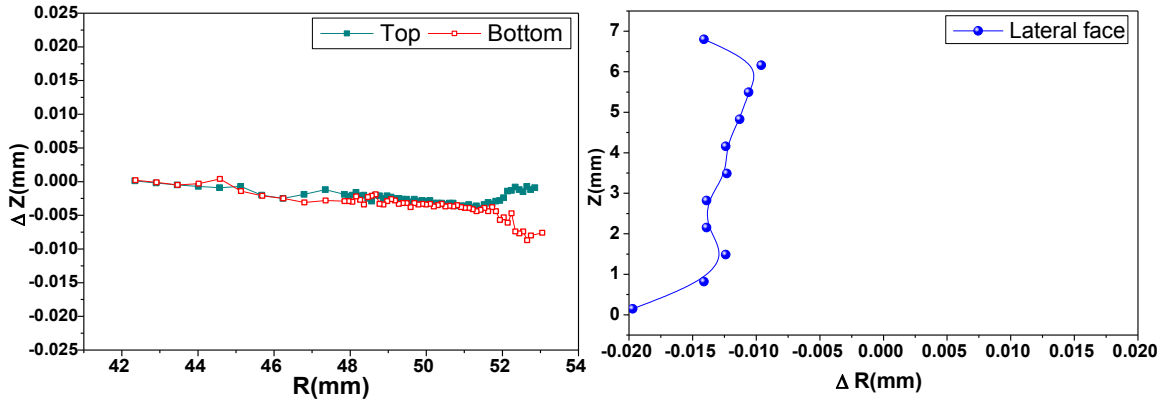

(a)

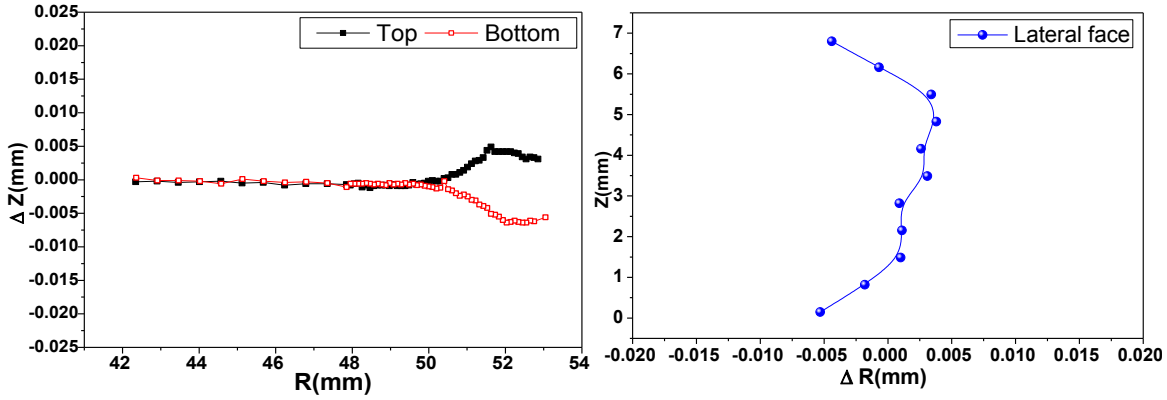

(b)

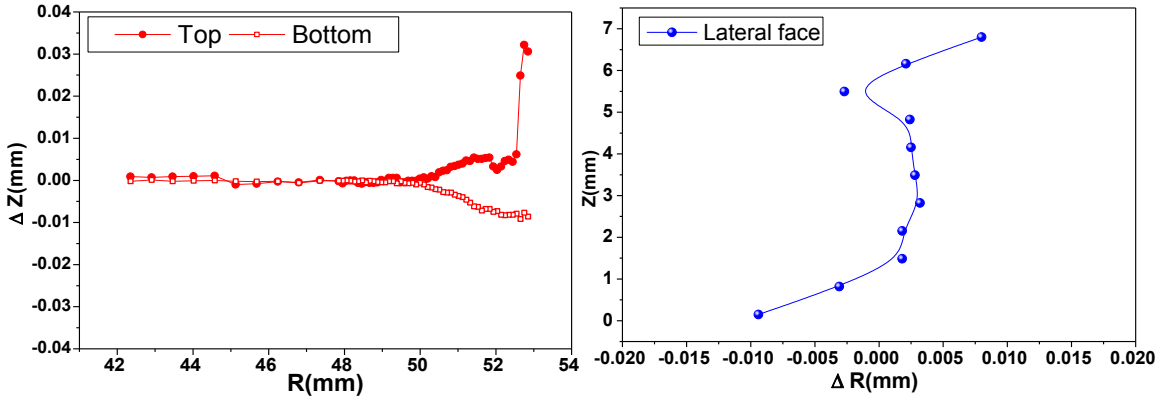

(c)

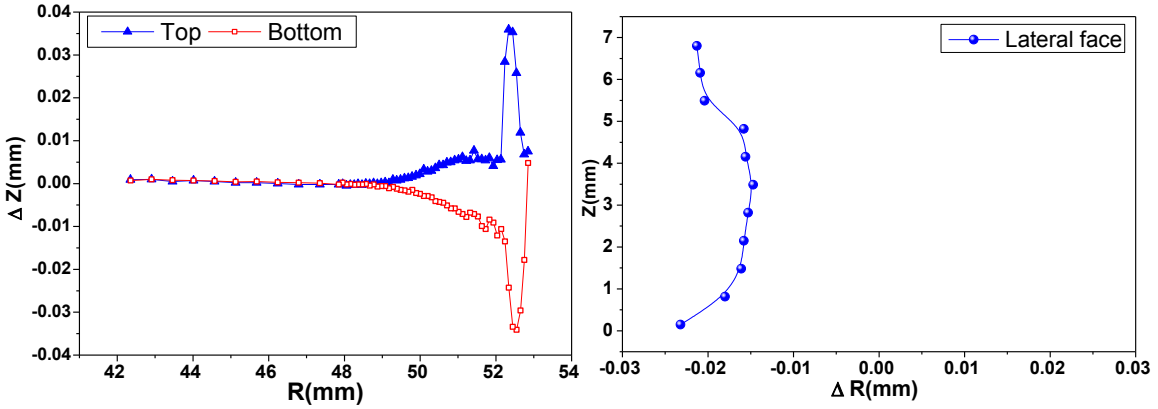

(d)

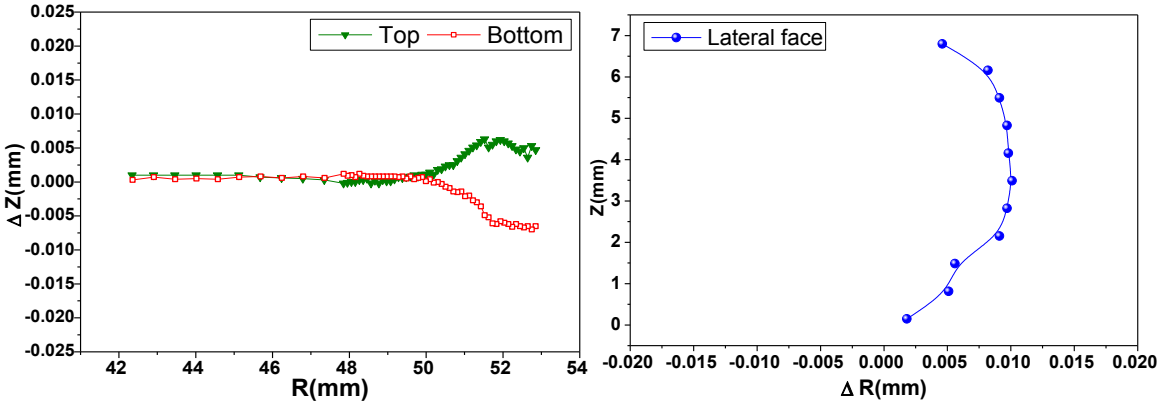

(e)

Fig 5 (a) to (e): axial (left) and radial (right) distortion profiles of disc #11 to #15 at measuring angle of 180˚

3. At measuring angle of -90° (+X-axis)

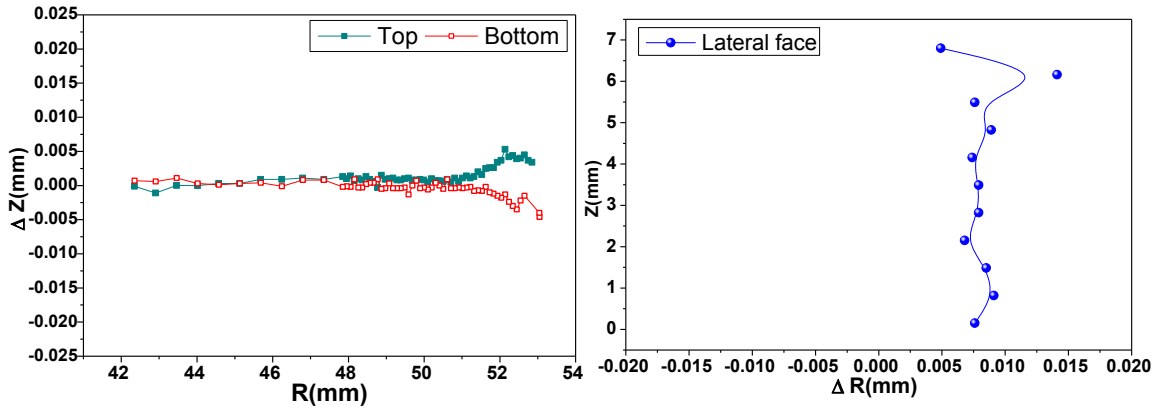

(a)

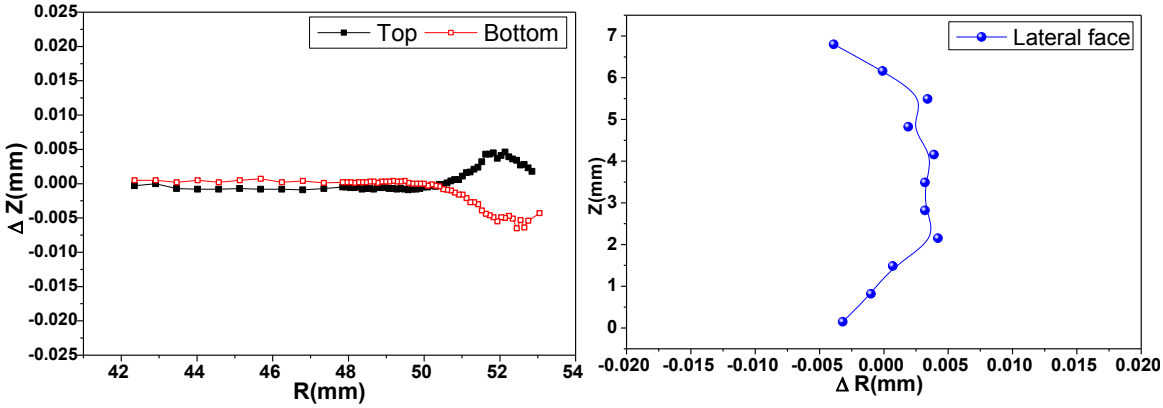

(b)

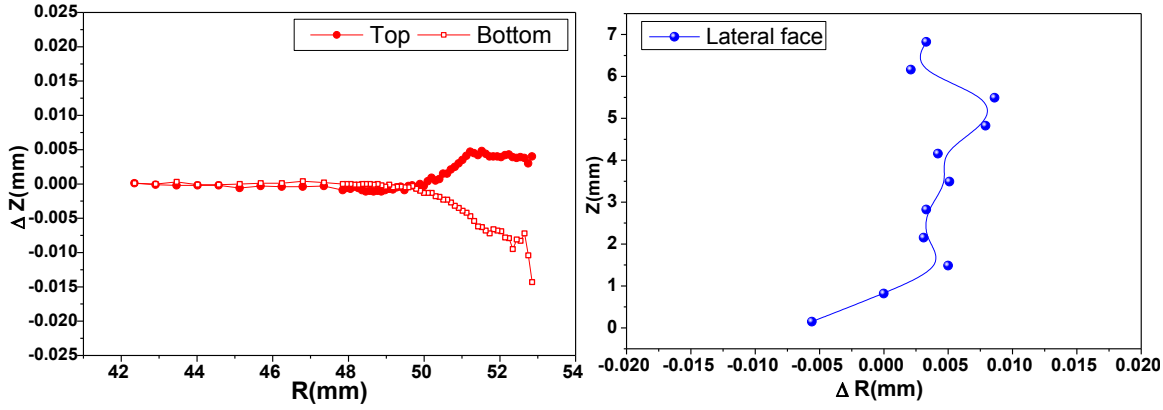

(c)

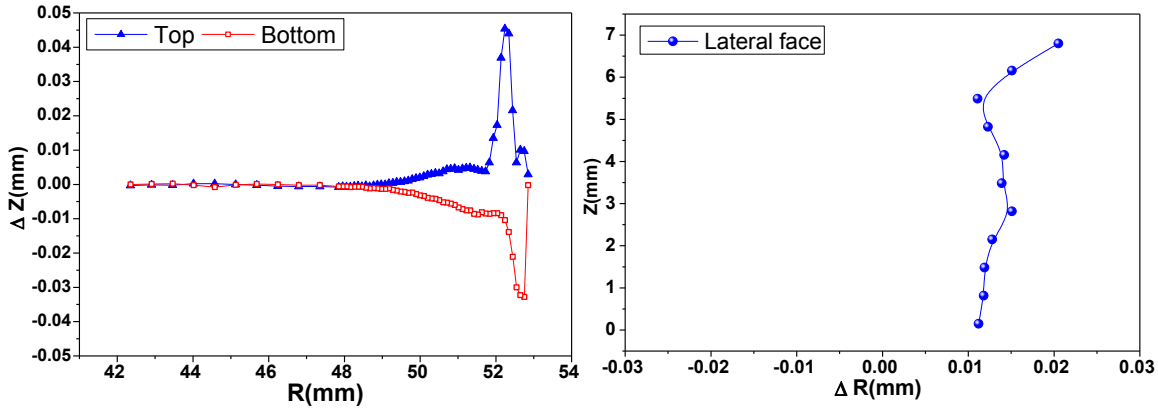

(d)

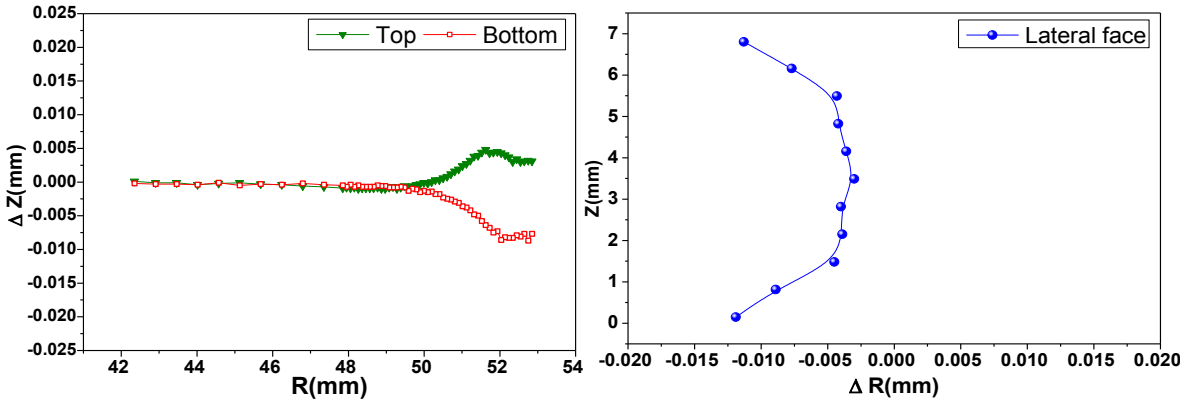

(e)

Fig 6 (a) to (e): axial (left) and radial (right) distortion profiles of disc #11 to #15 at measuring angle of -90˚

- **Group III (disc #16 to #20 with initial hardness of 27HRC)**

1. At measuring angle of 90˚ (-X-axis):

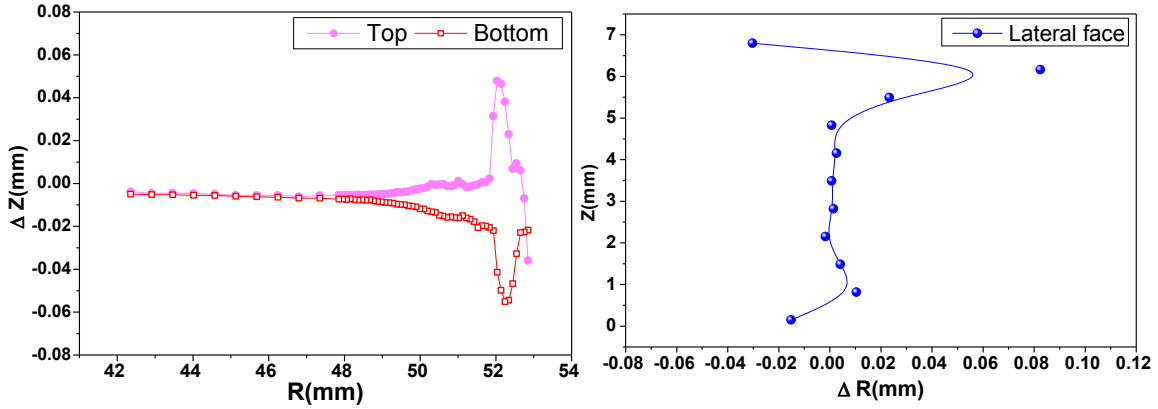

(a)

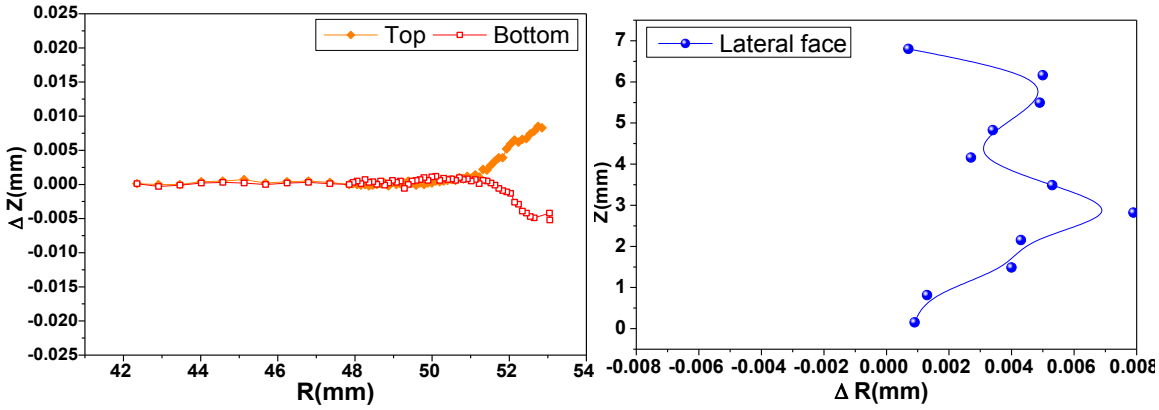
Top
Bottom
Δ Z(mm)
R(mm)
Lateral face
Z(mm)
Δ R(mm)

(b)

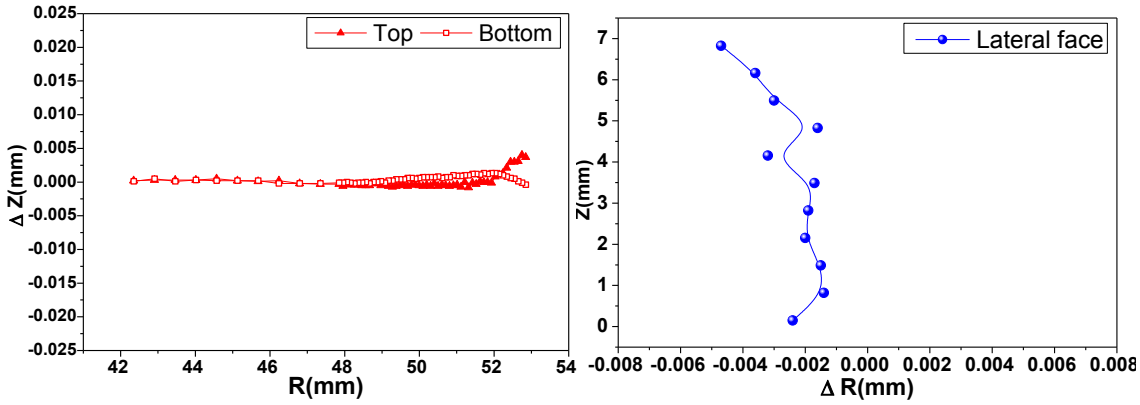
Top
Bottom
Δ Z(mm)
R(mm)
Lateral face
Z(mm)
Δ R(mm)

(c)

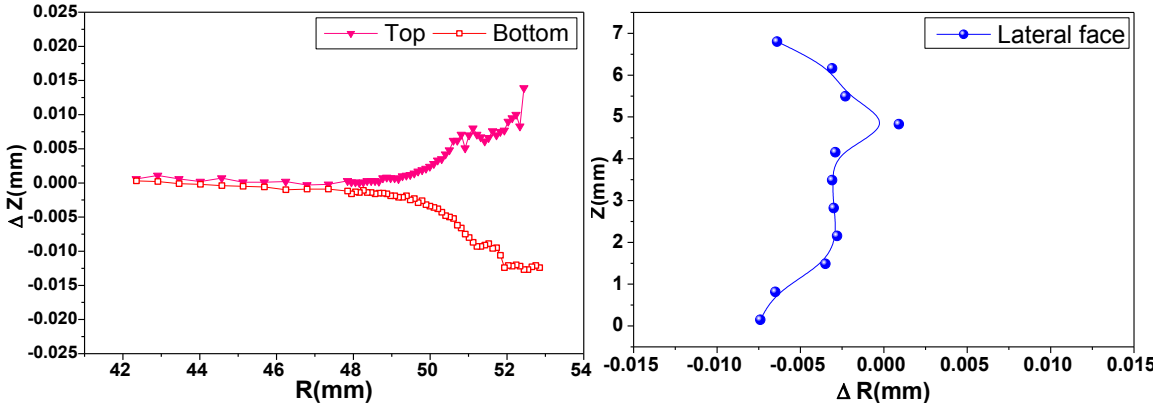
Top
Bottom
Δ Z(mm)
R(mm)
Lateral face
Z(mm)
Δ R(mm)

(d)

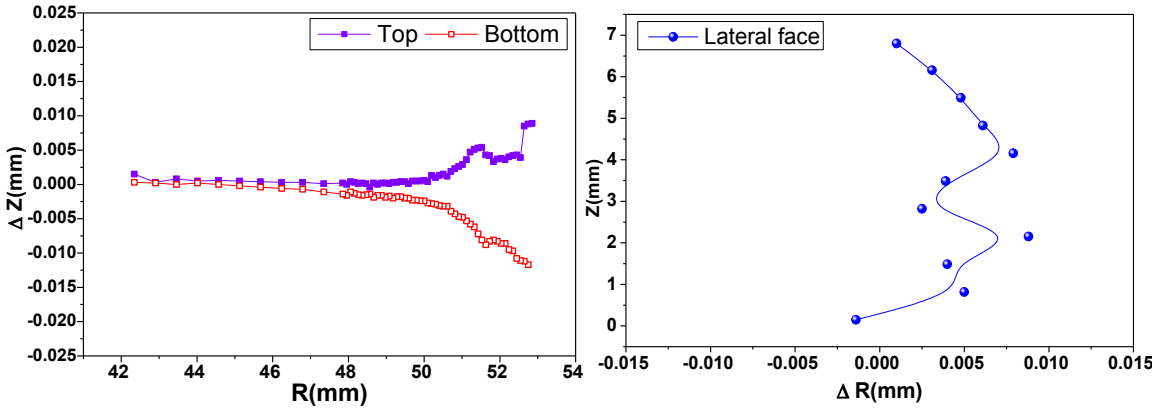

(e)

Fig 7 (a) to (e): axial (left) and radial (right) distortion profiles of disc #16 to #20 at measuring angle of 90˚

2. At measuring angle of 180˚ (+Y-axis)

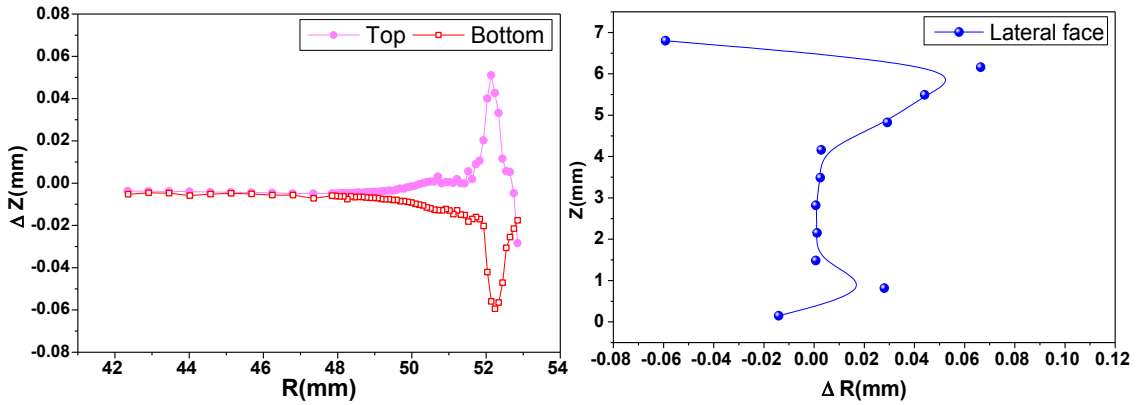

(a)

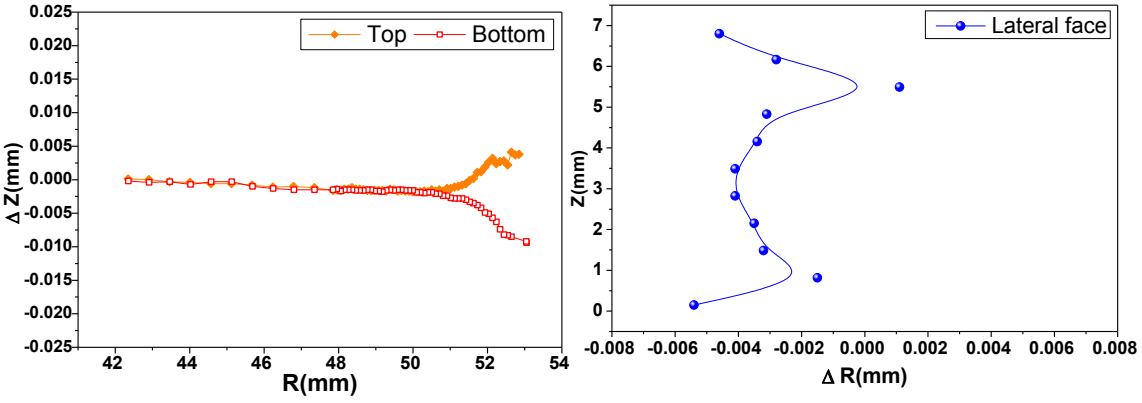

(b)

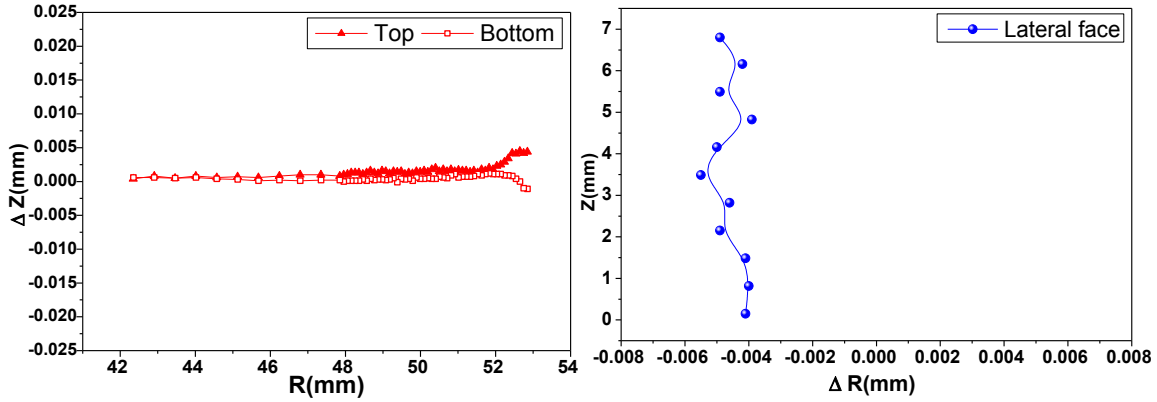

(c)

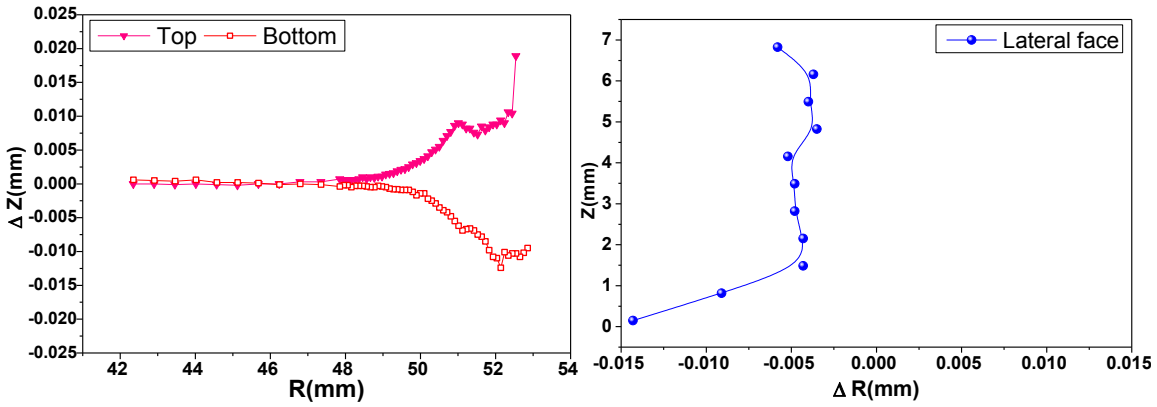

(d)

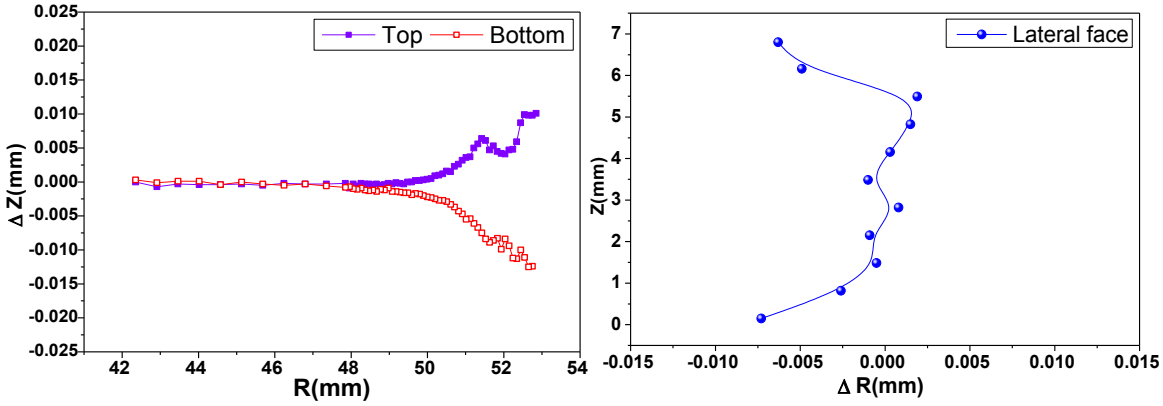

(e)

Fig 8 (a) to (e): axial (left) and radial (right) distortion profiles of disc #16 to #20 at measuring angle of 180˚

3. At measuring angle of -90° (+X-axis)

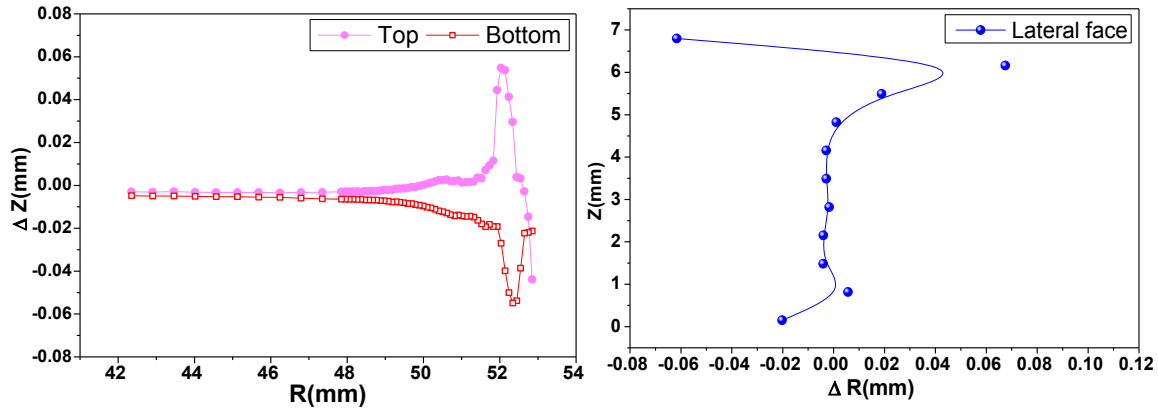

(a)

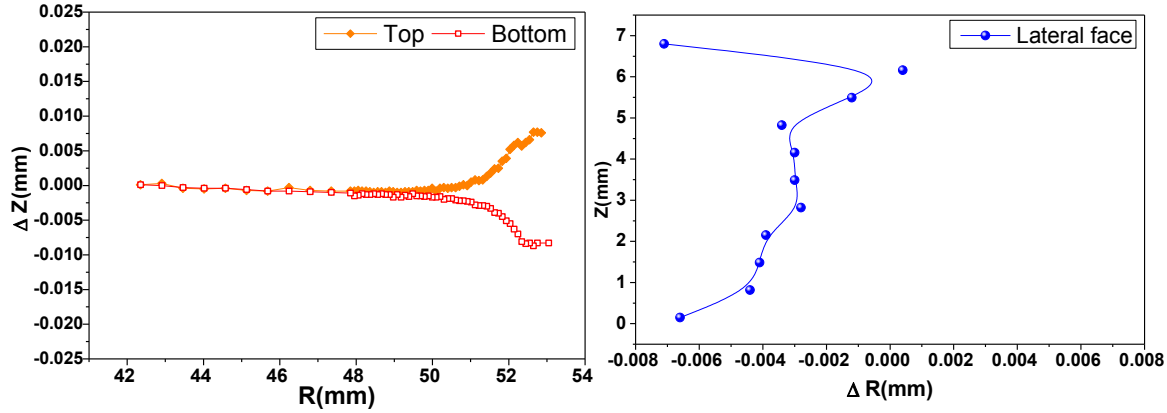

(b)

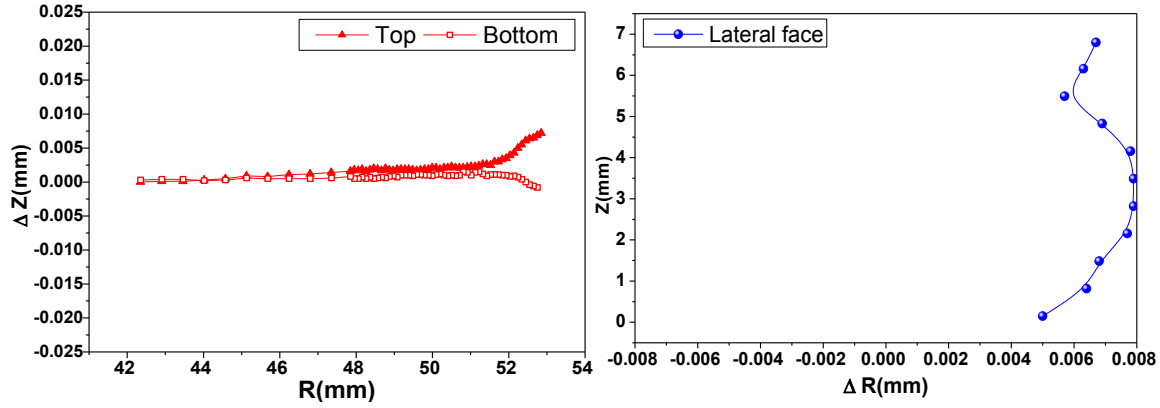

(c)

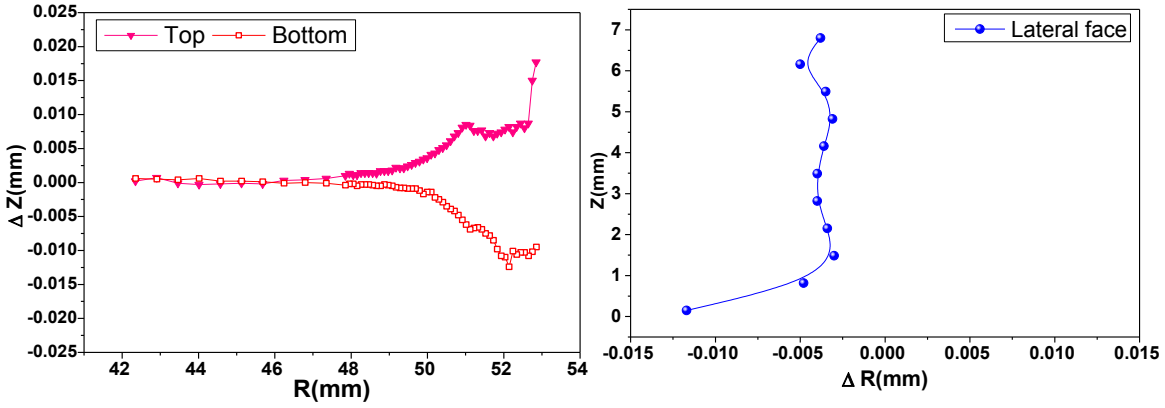

(d)

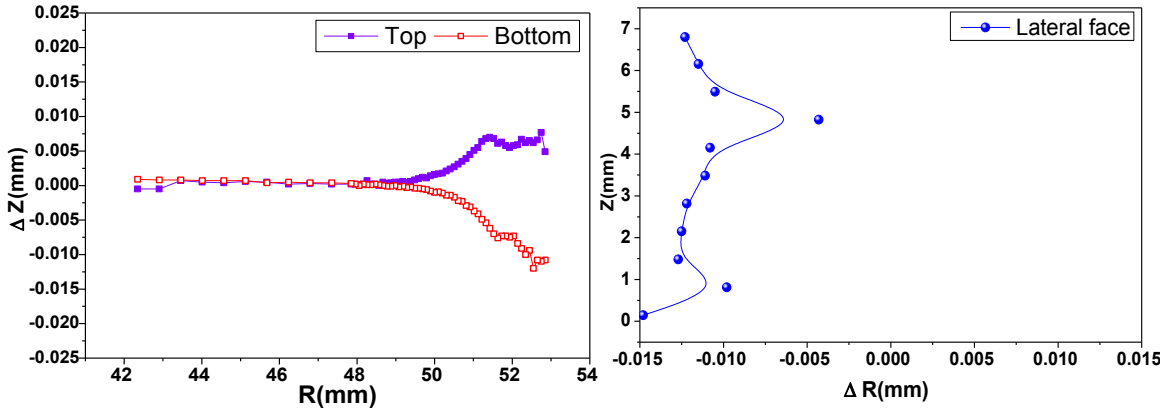

(e)

Fig 9 (a) to (e): axial (left) and radial (right) distortion profiles of disc #16 to #20 at measuring angle of -90˚

Appendix III

Repeatability and Surface Roughness Verifications for Distortion Measurement

- **Repeatability:**

Fig 1 to 3 give an example of coordinate measurement (by CMM) repeatability check on disc #1 top surface. Fig 1 is the top face 2D map of disc #1 measured by CMM at first time. Fig 2 is the top face 2D map of the repeat measurement on the same disc. Fig 3 is the linear comparison of top face Z coordinate between first and repeat measurement at the measuring angle of 0º.

It can be seen from Fig 1 to Fig 3 that disc #1 shows a slightly gradual increase of Z on top face towards the disc's center. Based on the 2D map comparison between Fig 1 and Fig 2, it is found that the top face profile between two individual measurements is quite similar. Fig 3 shows a more clear idea of present CMM measurement repeatability. It can be seen from Fig 3, the difference between two measurements is smaller than 1 E-03mm. Besides, according to the statistic analysis based on all data measured on disc #1 top face, it shows the mean absolute deviation between two measurements is 6.07E-04, no more than 1 E-03mm.

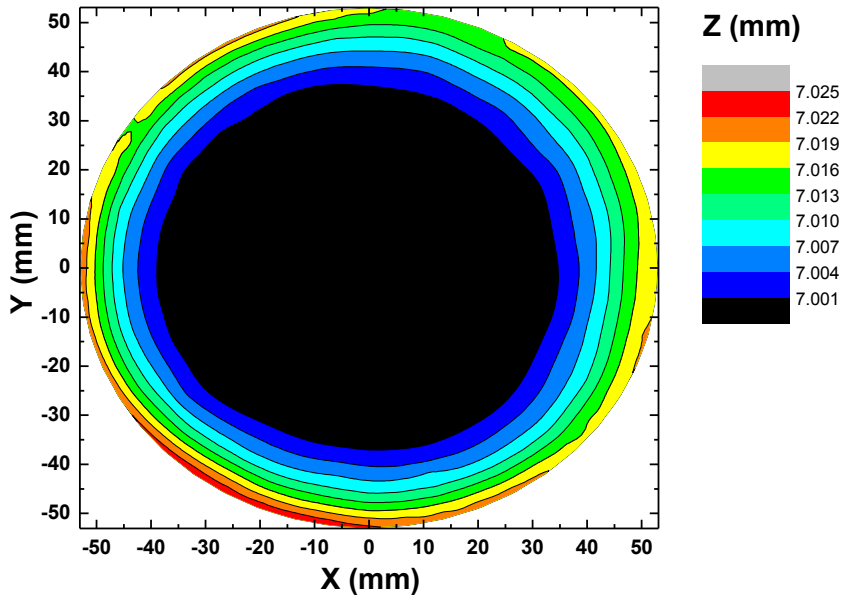

Fig 1: Top face 2D map (first measurement) of disc #1 before IH treatment

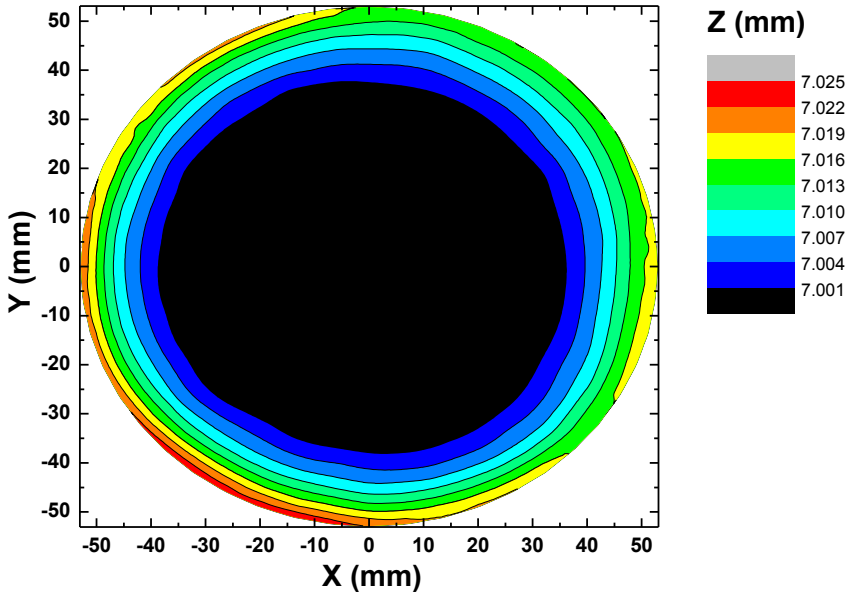

Fig 2: Top face 2D map (repeat measurement) of disc #1 before IH treatment

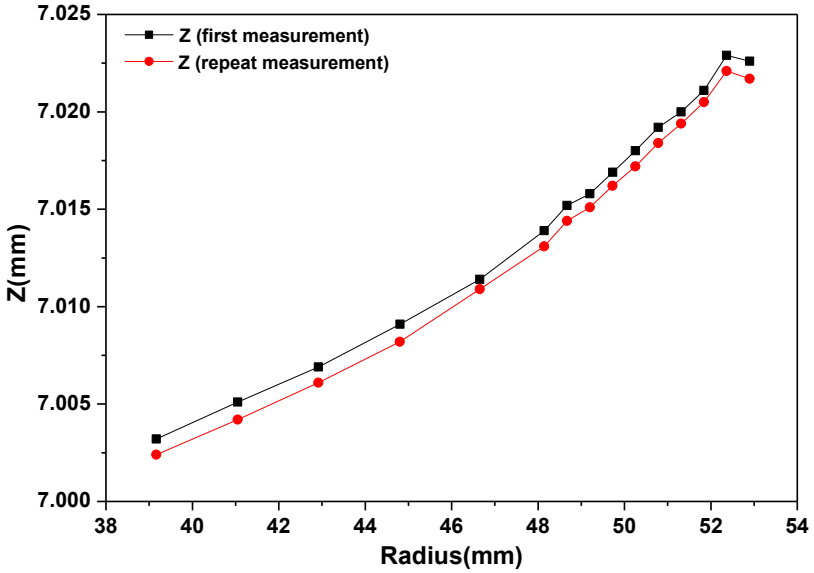

Fig 3: Comparison of Z coordinates on the top face of disc #1 between the first and the repeated measurements, at measuring angle 0º

- **Surface roughness investigation:**

Fig 4 and Fig 5 display the variation of Z coordinate on disc #1 top face by 2D map and by linear analysis. It can be from both figures that there is a slightly gradual increase of Z coordinate on top face. This could be resulted from the sample manufacture process.

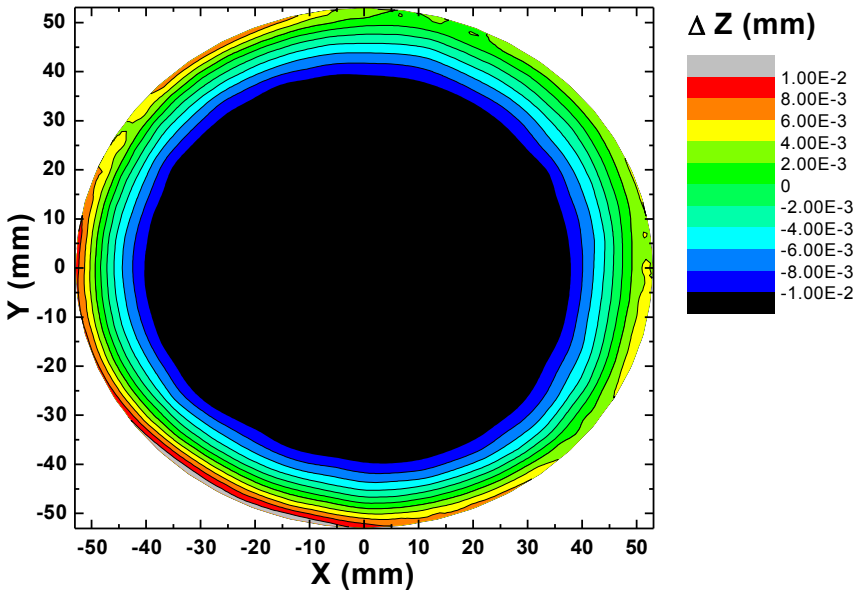

Fig 4: 2D map of Z coordinate variation on disc #1 top face

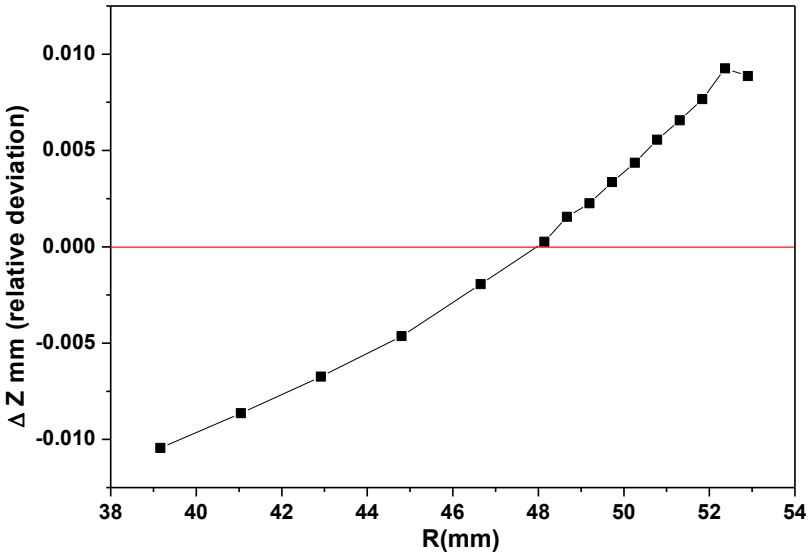

Fig 5: Linear of Z coordinate variation on disc #1 top face, at measuring angle of 0º